UNIVERSITY OF BELGRADE

SCHOOL OF ELECTRICAL ENGINEERING

Milan Žeželj

MODELING AND OPTIMIZATION OF TRANSPORT PROCESSES IN MODERN NANOELECRONIC DEVICES

Doctoral dissertation

Belgrade, 2016

УНИВЕРЗИТЕТ У БЕОГРАДУ

ЕЛЕКТРОТЕХНИЧКИ ФАКУЛТЕТ

Милан Жежељ

МОДЕЛОВАЊЕ И ОПТИМИЗАЦИЈА ТРАНСПОРТНИХ ПРОЦЕСА У САВРЕМЕНИМ НАНОЕЛЕКТРОНСКИМ УРЕЂАЈИМА

Докторска дисертација

Београд, 2016

Thesis advisor, Committee member:
Dr. Jelena Radovanović
Professor
School of Electrical Engineering
University of Belgrade

Committee member:
Dr. Vitomir Milanović
Professor Emeritus
School of Electrical Engineering
University of Belgrade

Committee member:
Dr. Igor Stanković
Associate Research Professor
Institute of Physics Belgrade
University of Belgrade

Committee member:
Dr. Jovan Radunović
Professor – Retired
School of Electrical Engineering
University of Belgrade

Committee member:
Dr. Branko Malešević
Associate Professor
School of Electrical Engineering
University of Belgrade

The doctoral dissertation of Milan Žeželj was defended on _____.

To my family and friends

Acknowledgments

This thesis was written in the Scientific Computing Laboratory (SCL), Center for the Study of Complex Systems of the Institute of Physics Belgrade under the supervision of Dr. Igor Stanković. I would like to thank Igor for his generous help and careful guidance through all aspects of my PhD studies. I gratefully thank him for teaching me about good scientific practice and for introducing me to the exciting world of complex physical systems. I also thank Igor for his encouragement when it was most required. I especially thank Dr. Antun Balaž, head of SCL, for giving me the opportunity to be a member of the laboratory and for his infinite support in all aspects of my life. For precious scientific discussions, advice, and generous help, I thank Dr. Nenad Vukmirović. Dr. Aleksandar Belić and Danica Stojiljković have greatly contributed to my understanding of percolation theory and critical phenomena, some of the main topics of this thesis, and I would like to thank them both. The work presented in Chapter 5 was done in close collaboration with professors Dr. Jelena Radovanović and Dr. Vitomir Milanović from the School of Electrical Engineering, University of Belgrade. I thank both of them for many scientific discussions and for numerous things that I have learned from them during the graduate courses, as well as for giving me the opportunity to work with them on unexplored topics in the field of quantum cascade lasers. I would like to thank my colleagues, but first of all my friends, for great time I have spent at the SCL.

This thesis was supported by the Ministry of Education, Science, and Technological Development of the Republic of Serbia under projects No. ON141035 and No. ON171017, by the SCOPES Grant No. IZ73Z0–128169 of the Swiss National Science Foundation, and by Pančevo Dairy.

Finally, I am indebted to my sons, wife, mother, father, brother, grandmothers, and grandfathers for their love and infinite support that goes far beyond my graduate studies.

Modeling and optimization of transport processes in modern nanoelectronic devices

Abstract

A functionality of modern nanoelectronic devices cannot be precisely described without using appropriate statistical methods and models needed for understanding different transport properties in those devices. Therefore, in this thesis we develop and integrate different numerical approaches for modeling and optimization of transport processes, such as algorithms for percolation detection, conjugate gradient methods, and simulated annealing algorithms. Using these methods and algorithms we propose different models that describe and optimize effects of structural and geometrical parameters on transport properties of modern nanoelectronic devices, such as transparent conducting nanowire networks, thin-film carbon nanotube transistors, and quantum cascade lasers. For transparent networks of randomly distributed conducting nanowires, we propose an electrical conductivity model that explicitly depends on the nanowire density and junction-to-nanowire conductance ratio. Using the proposed model we quantify a relationship between the optical transparency and the electrical conductivity of the transparent nanowire networks. For thin-film transistors based on random networks of as-grown single-walled carbon nanotubes, we determine the carbon nanotube density, length, and channel dimensions under which the transistors simultaneously attain high on-current and high on/off ratio. Finally, we show that the decrease in the output characteristics of GaAs/AlGaAs quantum cascade laser in the presence of an intense external magnetic field is significantly moderated by the presence of interface roughness scattering. We also present an efficient numerical algorithm for optimization of quantum cascade laser active region parameters and calculation of its output characteristics in a magnetic field.

Keywords: transport processes, percolation theory, random nanowire networks, transparent conductors, random carbon nanotube networks, thin-film transistors, interface roughness scattering, quantum cascade lasers

Scientific field: Electrical and Computer Engineering

Research area: Nanoelectronics and Photonics

UDC number: 621.3

Моделовање и оптимизација транспортних процеса у савременим наноелектронским уређајима

Сажетак

Функционалност савремених наноелектронских уређаја се не може прецизно описати без коришћења одговарајућих статистичких метода и модела потребних за описивање разноврсних транспортних процеса у тим уређајима. Због тога смо у овој тези развили и интегрисали различите нумеричке приступе за моделовање и оптимизацију транспортних процеса, као што су алгоритми за детектовање перколације, конјуговани градијентни методи и алгоритми за симулирано одгревање. На основу ових метода и алгоритама предложили смо различите моделе који описују и оптимизују утицај структурних и геометријских параметара на транспортна својства савремених наноелектронских уређаја, као што су прозирни проводници са мрежама наножица, танкослојни транзистори са угљеничним нанотубама и квантни каскадни ласери. За прозирне мреже насумично распоређених проводних наножица, предложили смо модел електричне проводности који експлицитно зависи од густине наножица и односа проводности контакта и наножице. Користећи предложени модел квантификовали смо однос између оптичке транспарентности и електричне проводности прозирне мреже наножица. За танкослојне транзисторе засноване на случајним мрежама неселектованих једнозидних угљеничних нанотуба, одредили смо њихову густину, дужину и димензије канала при којима транзистори истовремено достижу високу струју провођења и висок однос струје провођења и струје цурења. Коначно, показали смо да је слабљење излазних својстава GaAs/AlGaAs квантног каскадног ласера у присуству јаког спољашњег магнетног поља значајно одређено присуством расејања на површинским неравнинама. Такође, представили смо ефикасан нумерички алгоритам за оптимизацију параметара активног региона квантног каскадног ласера и израчунавање његових излазних карактеристика у магнетном пољу.

Кључне речи: транспортни процеси, перколациона теорија, неуређене мреже наножица, прозирни проводници, неуређене мреже угљеничних нанотуба, танкослојни транзистори, расејање на површинским неравнинама, квантни каскадни ласери

Научна област: Електротехника и рачунарство

Област истраживања: Наноелектроника и фотоника

УДК број: 621.3

Contents

Chapter 1 Introduction

Transport processes are very important for understanding and modeling of a wide variety of phenomena, not only in modern nanoelectronic devices, but also in physics, biology, chemistry, and neuroscience [1–3]. Typical examples of transport processes in nanoelectronic devices include hopping transport in semiconductor systems, diffusion in porous materials, electrical or thermal conduction in composite solids, optical processes in heterogeneous materials, etc. [1]. With the advent of powerful computers, efficient computational algorithms have been developed for estimating transport properties at the macroscopic level [1, 2]. These computational algorithms are usually based on numerically solving large systems of (non)linear equations obtained from the physical laws that determine the transport processes at microscopic level [1–3].

Here we develop and integrate different numerical approaches for modeling and optimization of transport processes in materials of complex and disordered morphology, such as algorithms for percolation detection [4], conjugate gradient methods [5, 6], and simulated annealing algorithms [7, 8]. An important tool for describing effects of connectivity in a disordered material on its transport properties is percolation theory [1, 2]. For instance, percolation theory precisely quantifies how the conducting components of a composite material, that consists of conducting and insulating phases, cluster together and form spanning paths for transport of current, heat, or stress across the material [1, 2]. Therefore, algorithms for percolation detection, based on the percolation theory, are used to determine connectedness of a complex and disordered network considering connectivity of its individual elements. The conjugate gradient method is most prominent iterative method for solving a sparse system of linear equations [9], while the simulated annealing algorithm belongs to a class of stochastic global optimization methods based on the Metropolis

function for the acceptance probability [10]. Using these methods and algorithms we propose here different models to describe and optimize effects of structural and geometrical parameters on transport properties of modern nanoelectronic devices, such as transparent conducting nanowire networks, thin-film carbon nanotube transistors, and quantum cascade lasers.

The transparent conducting nanowire networks are thin films of randomly distributed metallic (usually Ag) nanowires. The thin-film carbon nanotube transistors are (quasi-)two-dimensional networks of randomly distributed single-walled carbon nanotubes. Nanowires and single-walled carbon nanotubes are rodlike nanoparticles that can be regarded as widthless sticks, because their length is much larger than their diameter[1]. Therefore, the connectedness of complex and disordered systems, such as random networks of nanowires and random networks of carbon nanotubes, can be characterized by applying the concepts of percolation theory to the systems of randomly distributed sticks. For that reason, we have also developed an efficient numerical algorithm for the stick-percolation detection. Using this algorithm we have investigated finite-size scaling effects in percolating widthless stick systems through an extensive Monte Carlo simulation study. A generalized scaling function for two-dimensional stick systems is introduced to describe the scaling behavior of the first two percolation probability moments. This generalized scaling function, with geometry-dependent prefactors and constant exponents in its expansion, is used to propose an analytic model of the percolation probability function. The analytic model is used to estimate an optimal density of random carbon nanotubes for which their thin-film networks exhibit excellent transistor performance. Also, we have developed an algorithm for calculating the electrical conductivity of two-dimensional systems comprised of randomly distributed sticks. This algorithm is based on the conjugate gradient method for solving large systems of linear equations. Using this algorithm we obtain electrical conductivity dependence of transparent conducting nanowire networks on the nanowire density and junction-to-nanowire conductance

[1]Single-walled carbon nanotubes have the smallest diameter of all carbon nanotubes, distributed within a narrow range ($0.8 - 5$ nm), and a length from tens of nanometers to millimeters [11], whereas nanowires have a larger diameter (~ 10 to > 100 nm) and lengths similar to those of carbon nanotubes [12].

ratio. Also, using this algorithm we have calculated electrical properties of thin-film carbon nanotube transistors in on- and off-state for different channel dimensions and different lengths of carbon nanotubes. We have also defined acceptable ranges of these geometrical parameters for which the transistors simultaneously attain high on-conductance and high on/off conductance ratio.

Finally, we note that many materials have a very rough surface, where the roughness follows a very complex pattern. The quantum cascade lasers are nanoelectronic devices based on parallel semiconductor layers with in-plane terrace-like surface defects at the interfaces between the layers. We have studied here effects of the interface roughness scattering on electron transport and output characteristics of quantum cascade laser in a magnetic field by solving the full set of nonlinear rate equations that describe electron transitions between different energy levels. The system of nonlinear rate equations can be successively solved by solving the corresponding system of linear equations in each of the successive steps. The conjugate gradient method can be separately applied in each step for solving the obtained systems of linear equations. Also, the optimization of the quantum-cascade-laser performance at a selected wavelength can be performed at the entire free-parameters space using simulated annealing algorithm.

The rest of this thesis is organized as follows. A brief overview of the most important transport processes in each of the considered nanoelectronic devices is given in the rest of this Chapter. In Chapter 2 we investigate the finite-size scaling effects in the percolating widthless stick systems with variable aspect ratios through an extensive Monte Carlo simulation study. In Chapter 3 we numerically investigate electrical conductivity of two-dimensional random nanowire networks from the percolation threshold up to ten times the percolation threshold density. We propose a conductivity model explicitly dependent on the nanowire density and nanowire-to-stick conductance ratio. Using the proposed model we quantify a relationship between the optical transmittance and the electrical conductivity of the random nanowire networks. In Chapter 4 we numerically study the effects of geometrical and structural parameters of the thin-film carbon nanotube networks on their electrical properties in order to obtain an optimized and uniform transistor performance

without using any post-growth treatment. Finally, in Chapter 5 we investigate an influence of interface roughness scattering on output characteristics of GaAs/AlGaAs quantum cascade laser in a magnetic field. Also, we describe an efficient numerical algorithm for optimization of GaAs/AlGaAs quantum cascade laser active region parameters and calculation of its output characteristics in a magnetic field.

1.1 Electrical conductivity vs. optical transparency of random nanowire networks

Randomly distributed nanowires (NWs) networks are flexible, electrically active materials with great promise for use as an active medium of transparent-conductor applications [13–15], thin-film solar cells [16], and sensor devices [17]. The implementation of NWs for any of these applications assumes the activation of junctions between wires in the network, which is typically accomplished by using heat [18], pressure [19], or electrical stress [20]. As a result, the random NW networks are established as electrically active materials with high electrical conductivity and well-preserved optical transparency as two most important critical performance criteria for the transparent-conductor applications [21]. Many studies [13, 21–23] have revealed a trade-off between high electrical conductivity and high optical transparency of random NW transparent conductors. Therefore, the electrical conductivity dependence and optical transparency dependence on the NW density and system geometry needs to be taken into account in any random NW design [24]. Nanowires are most typically comprised of metallic NWs, which can be regarded as conductive widthless sticks, because they are straight and rigid rodlike nanoparticles whose length is much larger than their diameter [12, 25]. The percolation models [2, 26] are often used to model an onset of the high electrical conductivity in the composites consisting of the conductive widthless sticks in the insulating matrices [13, 15, 27–29].

The percolation theory predicts that the electrical conductivity of the composite materials with the conductive filler density n above, but close to the percolation threshold n_c, increases with the density by a power scaling law $\sigma \sim (n - n_c)^t$, with the universal conductivity exponent $t \approx 1.29$ for two-dimensional (2D) systems [2].

While the conductivity scaling law is expected to be applicable only near the percolation threshold, in many experiments the scaling law was used over a much larger range of concentrations, but with the nonuniversal values of the conductivity exponent [18, 28–30]. Madaria *et al.* [18] used the conductivity scaling law to extract the conductivity exponent of highly conductive Ag nanowire networks. However, fitting the experimental data in a very broad density range, from the percolation threshold up to more than ten times the percolation threshold density, they obtained the nonuniversal value 1.42 for the conductivity exponent. Hu *et al.* [28] also obtained the nonuniversal value 1.5 for the conductivity exponent using the conductivity scaling law for fitting the experimental data for ultrathin carbon nanotube networks operating from the percolation threshold up to about ten times the percolation threshold density. At the same time, several numerical studies confirmed the observed nonuniversality of the conductivity exponent when the stick density was well above the percolation threshold [31–33]. Keblinski *et al.* [31] demonstrated that the universal power law holds from the percolation threshold n_c, to about twice its value $2n_c$. For higher stick density, $n > 2n_c$, they observed that the conductivity scaling exponent in the following cases becomes: (i) slightly higher than 1 when junctions are superconductive and only the stick conductance is the limiting factor for the current flow through the system; and (ii) close to 1.75 when the sticks are superconductive and the contact conductance is the limiting factor. Li *et al.* [33] showed that the conductivity exponent significantly varies with the junction-to-stick conductance ratio for lower stick densities, up to $2n_c$. The broad range applicability of the conductivity scaling law was explained by the presence of long-range correlations in the distribution of conductive sticks in the system [1].

In Chapter 3, we will demonstrate that the nonuniversality of the conductivity exponents is a consequence of a transition from the percolating to dense NW networks. We will numerically investigate the conductivity of the randomly distributed NWs networks from the percolation threshold up to ten times the percolation threshold density. We will show that it is not appropriate to use a simple scaling law to describe the conductivity dependence on the density, both for finite and dense networks. Based on our Monte Carlo simulation results, we will propose a conductivity

model that describes the electrical conductivity dependence on the NW density and the different junction-to-NW conductance ratios. The model is motivated by the observed structural characteristic (i.e., the density of total NWs and NW-to-NW contacts involved in the current flow through the system). The finite-size effects, especially pronounced in the vicinity of the percolation threshold, are also included in the generic description for the conductivity of random NW networks. Finally, using the proposed model and an analytical approximation for the density-dependent optical transmittance, we will quantify the dependence of the optical transparency on the electrical conductivity for random NW networks. Also, we will show that random NW networks can be used as high-performance transparent conductors only if the length-to-diameter aspect ratio of constituent NWs is higher than 100.

1.2 Electrical transport in random carbon nanotube networks

Recently, random carbon nanotube (CNT) networks have been demonstrated as potentially useful active materials in electronics applications [34], optoelectronics [35], sensors [36], and memory cells [37]. CNT thin-film transistors (TFTs) are expected to enable fabrication of high-performance, flexible, and transparent devices using relatively simple techniques [11, 38–46]. As-grown networks of single-walled (SW) CNTs contain both metallic (m-CNTs) and semiconducting (s-CNTs) nanotubes in an approximate ratio 1:2, which leads to a trade-off between on-conductance and the on/off conductance ratio [47–50]. If the density of CNTs in a TFT is sufficiently high so that m-CNTs exceed the percolation threshold, the CNT network will become predominantly metallic and, hence, the on/off ratio will be very small [50]. In contrast, if the CNT density is so low that a conduction path through m-CNTs does not exist, a high on/off ratio can be attained, but under such circumstances the low on-conductance is disadvantage [50, 51].

Various experimental efforts have been made to improve different transport processes in random CNT TFTs. A simultaneous increase of on-conductance and the on/off ratio is one of the most important requirements for achieving high-performance transistor devices. With roughly 1/3 of as-grown CNTs being metallic,

extra steps, such as electrical burning of m-CNTs via an electrical breakdown method [52], are used in order to cut the metallic paths through the transistors. However, such breakdown also removes some s-CNT pathways, leading to a decrease of the on-conductance. If the breakdown is applied when s-CNTs in the network are gated to the off-state, most of s-CNTs will be well preserved and the on-conductance will not be much affected [37]. However, using additional steps after the CNTs synthesis process, such as electrical breakdown methods, prolongs the production time and thus increases production costs. Other researchers have used semiconducting enriched CNTs in order to enhance the performance of CNT TFTs. For example, methods that separate CNTs by electronic type, such us density-gradient ultracentrifugation [53] or the gas-phase plasma hydrocarbonation reaction techniques [54] are used after or during the CNTs synthesis process in order to obtain pure semiconducting nanotubes. However, these techniques also create defects in the remaining CNT networks and add impurities, which degrade the overall performance of TFTs [55–57]. This approach also increases the difficulties in the fabrication process, and the repeatability and uniformity of devices are uncertain [55].

The effects of m-CNTs in a random network can be reduced by carefully controlling the CNT density, length, and device geometry, such that the metallic fraction of CNTs is below the percolation threshold [34], i.e., each conducting path contains at least one semiconducting CNT. An optimized device, i.e., one with the highest possible on-conductance at a given on/off ratio, has a total density of CNTs above the percolation threshold and a density of m-CNTs below the percolation threshold. Although such high-quality devices have been reported in the literature [50, 51, 58, 59], numerical simulations and experiments to determine the CNT density, channel size, and CNT length for optimum device performance, fabricated at industrial yield rates are still lacking.

In Chapter 4, we will study effects of device parameters (density of CNTs, channel dimensions and CNT length) on their electrical transport processes, i.e., on the on-conductance and on/off ratio, in order to design an optimized and uniform device performance without using any post-growth treatment. Using a realistic numerical approach, we determine the CNT density, length, and channel dimensions for which

CNT thin-film transistors simultaneously attain on-conductance higher than 1 μS and an on/off ratio higher than 10^4. We show that a realization probability of desired characteristics higher than 99% is obtained for the channels with aspect ratio $L_{\mathrm{CH}}/W_{\mathrm{CH}} < 1.2$ and normalized size $L_{\mathrm{CH}}W_{\mathrm{CH}}/l_{\mathrm{CNT}}^2 > 250$ when the CNT length is $l_{\mathrm{CNT}} = 4 - 20$ μm and the normalized density of CNTs is close to the value where the probability of percolation only through s-CNT pathways reaches its maximum.

1.3 Electron transport in quantum cascade laser in a magnetic field

In recent years, quantum cascade lasers (QCLs) have become light sources of choice for a broad variety of applications including high-precision gas sensing, infrared imaging, military countermeasures, security monitoring, non-invasive medical diagnostics, optical communications [60–74]. In the mid- and far-infrared spectral range, these powerful light sources are particularly appreciated for the wide scope of operating wavelengths, which can be achieved by using the same heterostructure material combination. Some of the features that make this kind of devices so unique are: unipolarity, the population inversion achieved through careful quantum engineering of lifetimes of the states (typically in the picoseconds range), and the electron recycling due to the cascading scheme. Their performance under the influence of a high magnetic field has been intensively studied as well, due to the fact that magnetic field may serve as an efficient tool to determine the nature and magnitude of scattering mechanisms in the active region [63–66, 75–79]. Early experiments have demonstrated QCL emission enhancement and a magneto-phonon-resonance effects [63–65], which have led to a deeper insight into the physics of intersubband lasers. Furthermore, in the THz frequency range, where the performance of QCLs deteriorate rapidly with temperature, due to detrimental thermal activation of non-radiative losses, the highest operating temperature of 225 K is reported for the structure assisted by external magnetic field for additional carrier confinement [76]. Recently, a portable QCL-based infrared magnetospectrometer

covering the spectral range from 5 to 120 μm has been constructed, for applications in cyclotron-resonance spectroscopy measurements where high magnetic fields (up to 60 T) are required [67]. Hence, a detailed understanding of various scattering mechanisms under the influence of a strong magnetic field is an important factor for improving QCL performance and applicability.

The typical design of the QCL active region entails a three-level system. The transport of carriers, i.e., electrons, between these levels can be explained as follows. The electrons are injected into the upper laser state, from which they can relax into the lower state by means of photon-assisted transition or by scattering, mainly by interactions with longitudinal optical (LO) phonons. In order to achieve the population inversion, the lifetimes of electrons in the corresponding quantum states must satisfy the following relation $\tau_{32} > \tau_{21}$. This relation is achieved by means of two key points:

(1) the lifetime τ_{32} is increased by employing a transition with a reduced spatial overlap of the wavefunctions; and

(2) the lifetime τ_{21} is reduced by making the energy E_{21} resonant with the optical phonon energy, which is the most efficient scattering mechanism.

Further extension of otherwise short carrier lifetime (of the order of 1 ps) is achieved using an intense magnetic field parallel to the growth direction of semiconductor layers [64–66, 75]. The magnetic field breaks the two-dimensional (2D) in-plane continuous energy subbands into discrete Landau levels. The lifetime of electrons in the excited laser state is strongly modulated by the applied magnetic field. The dependence of the electron lifetime on the magnetic field strength results in oscillations in the laser emission intensity. The inelastic scattering by LO-phonons and elastic scattering by the interface roughness were identified as main mechanisms behind this effect by Leuliet *et al.* [66]. Given that the scattering processes between the two states depend on their energy spacing, certain relaxation mechanisms can be enhanced or inhibited by varying the magnetic field strength, although they may be influenced by the operating temperature as well. LO-phonon scattering is well explained in previous theoretical and experimental works [64–66, 75, 80]. Increasing the magnetic field reduces the number of relevant Landau levels and changes

energy differences between individual levels, thus affecting the lifetime of carriers in higher states. On the other hand, the strength of the interface roughness scattering in a particular sample is determined by the morphology of the interfaces [7, 8]. In contrast to LO-phonon, the interface roughness scattering does not depend on the temperature. As a result, the efficiency of the interface roughness scattering mechanism remains constant with increasing temperature, while the efficiency of the LO-phonon scattering is reduced due to their higher absorption rates [81].

In Chapter 5, we will present a theoretical description of a realistic QCL active region and introduce models for LO-phonon scattering and interface roughness scattering rate with and without a presence of an external magnetic field parallel to the confinement direction. We will study the electron relaxation rates for the upper state of the laser transition, due to electron–LO-phonon interactions and interface roughness scattering. To understand the effects of interface roughness scattering and compare them with the LO-phonon scattering, we will study relaxation times and optical gain for different temperatures and magnetic fields. The electron distribution over the states of the system can be found by solving the full set of rate equations that describe the electron transport between levels, and subsequently used to determine the optical gain. For both the population inversion and the optical gain, the interface roughness scattering will be shown to have a significant influence in terms of reducing the predicted magnitude, especially at low temperatures. Finally, we will describe an efficient numerical algorithm for optimization of GaAs/AlGaAs quantum cascade laser active region parameters and calculation of its output characteristics in a magnetic field.

Chapter 2 Finite-size scaling in asymmetric systems of percolating sticks

As already noted, there has been an increasing interest in the randomly distributed stick particles [27, 32, 51, 82, 83], due to promising developments in the area of the conducting rodlike nanoparticle networks, such as carbon nanotubes and silicon, copper, and silver nanowires, with applications in electronics [51, 84, 85], optoelectronics [28], and sensors [34, 86]. We note that most of the theoretical work in the field of percolation of random systems has been done for lattice percolation [2, 87–93]. The random stick networks are an important representative of the continuum percolation [26, 94–96]. The random stick percolation and lattice percolation fall into the same universality class having the same critical exponents [26], because all random systems fall on the same scaling function if dimensionality of the system, percolation rule, boundary conditions, and aspect ratio are fixed [91]. In real applications, the aspect ratio of the rectangular system is usually variable parameter, e.g., the geometry of the transistor gate channel in the carbon nanotube transistors is not fixed [51, 83]. Therefore, the objective of this Chapter is to describe in a consistent way finite-size scaling of average percolation density and standard deviation for the asymmetric rectangular stick systems with free boundaries and following that, to propose an analytic model of the percolation probability function. From general scaling arguments one would expect that for all finite-size systems their convergence is governed by an exponent $-1/\nu$ [2]. For two-dimensional (2D) systems $\nu = 4/3$ [2]. Following Ziff's initial publication [89], Hovi and Aharony [90, 91] argued that the irrelevant scaling variables in the renormalization-group treatment of percolation imply a slower leading-order convergence of percolation probability to its infinite-system value, characterized by an exponent $-1/\nu - \theta$, whose value was deducted from the Monte Carlo work of Stauffer to be $\theta \approx 0.85$ [87]. Further

it was shown that for lattice percolation on the square system the leading exponent of the average density at which percolation first occurs is $-1/\nu - \theta$, where $\theta \approx 0.9$ [93]. All the previous studies were performed for symmetric systems. We show that only in the symmetric case the exponent of average percolation density is $-1/\nu - \theta$. In asymmetric systems, we observe a leading $-1/\nu$ exponent. Another quantity, the percolation probability at the percolation threshold in symmetric bond percolating systems, is size independent, i.e., scale invariant [97]. Until now, this behavior has not been observed in other types of random percolating systems. We will demonstrate that asymmetric systems can exhibit scale-invariant behavior.

In this Chapter, we investigate finite-size scaling of the asymmetric rectangular stick systems with free boundaries. Both from renormalization group considerations and in the simulations, we find that the aspect ratio strongly influences scaling behavior of the percolation probability distribution function moments, i.e., average density of sticks at which percolation first occurs and variance of the percolation probability distribution function. A generalized scaling function is introduced, with aspect-ratio-dependent prefactors and constant exponents in its expansion. Also, an analytic model of the percolation probability function is proposed. Finally, it is shown that the percolation probability of the asymmetric infinite stick system at the critical threshold density agrees with Cardy's analytic formula [88].

2.1 Numerical method for calculation of stick percolation probability

Monte Carlo simulations, coupled with an efficient cluster analysis algorithm and implemented on a grid platform, are used to investigate the stick percolation [98–101]. A detailed description of the algorithm for stick-percolation detection is given below. We consider two-dimensional (2D) systems with isotropically placed widthless sticks of length l_s. The sticks are randomly positioned and oriented inside the rectangular system of length L_S and width W_S. For simplicity, the finite-size scaling effects will be further analyzed in terms of the system dimensions normalized by the stick length l_s. Therefore, the normalized system length is $L = L_S/l_s$, its width is

$W = W_S/l_s$, and the normalized sticks have unit length, i.e., $l = 1$, see Fig. 2.1(a). Two sticks lie in the same cluster if they intersect. The system percolates if two opposite boundaries perpendicular to the percolating direction (the left and right ones) are connected with the same cluster, see Fig. 2.1(b). The boundaries parallel to the percolating direction (the top and bottom ones) are free. The aspect ratio r is defined as the length of the rectangular system in the percolating direction (the x direction) divided by the length in the perpendicular direction (the y direction), i.e., in this case $r = L/W$. We only consider long-system limits ($L > l$) where an one-stick connection of system boundaries is impossible. We define the normalized system size as a square root of the rectangular area $\mathcal{L} = \sqrt{LW}$ (geometric average). The behavior of stick percolation is studied in terms of the number stick density $n = N/\mathcal{L}^2$. The percolation threshold of the infinite system is defined by the critical density $n_c \approx 5.63726$ [4, 101].

2.1.1 Algorithm for stick-percolation detection

The algorithm starts with a blank rectangular system assuming that the length direction at the same time represents the percolating direction, see Fig. 2.1(b). A similar algorithm was discussed in Ref. [98], where the lattice percolation was studied and in Ref. [101], where symmetric stick systems were analyzed. Two sticks lie in the same cluster if they intersect. A tree structure is used to store these clusters, as already shown in Ref. [98]. In each cluster, one stick is chosen to be the "root stick". All other sticks in the cluster have pointers which point either directly to the root stick or to another stick in the cluster. It implies that any stick in the cluster points directly or indirectly (through a path comprising other sticks) to the root stick and therefore, all sticks in the same cluster have the identical root stick. We note that a cluster percolates if and only if its orthogonal projection along the x-axis completely covers the bottom boundary of the system. For simplicity, this condition can be used for percolation detection in the rectangular stick system. In order to further simplify the percolation detection, the minimum and maximum value of the cluster projection along the x-axis should be stored for each cluster.

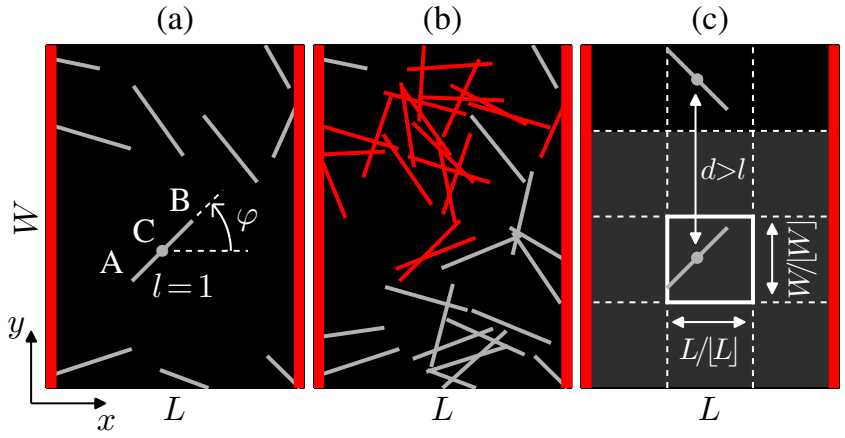

Figure 2.1: Schematic illustration of stick percolation on a rectangular system with normalized length $L = 3$ and width $W = 4$. (a) The rectangular stick system bellow the percolation density. Each stick is of unity length $l = 1$ and described by its center point C and orientation φ. The end points of a stick are denoted as A (closer to the left boundary) and B (closer to the right boundary). The system boundaries (the left and the right) are shown as vertical bold red lines. (b) The rectangular stick system at the percolation density. The sticks that belong to the percolating cluster are denoted with red color. (c) The system is virtually divided into $\lfloor L \rfloor \times \lfloor W \rfloor$ subcells (dashed white lattices) with size $L/\lfloor L \rfloor \times W/\lfloor W \rfloor$. Each stick is registered in the subcell where its center lies. It is explicitly shown that a stick in a subcell (bold white boundaries) is impossible to intersect any stick at other subcells than the sticks at the same subcell or its neighbors (the gray subcells).

The system is virtually divided into $\lfloor L \rfloor \times \lfloor W \rfloor$ subcells[1] (or sub-rectangles) with size $L/\lfloor L \rfloor \times W/\lfloor W \rfloor$, as shown by the dashed lattices in Fig. 2.1(c). Note that when the normalized system length L and width W are integers the system is divided into $L \times W$ sub-squares with unity length $l = 1$. With these preparations, a random normal stick is generated by producing a random point (x_C, y_C) for its center point and a random angle φ with respect to the horizontal direction for its orientation, see Fig. 2.1(a). Note that $0 \leq x_C \leq L$, $0 \leq y_C \leq W$, and $-\pi/2 \leq \varphi \leq \pi/2$. The stick is first treated as an one-stick cluster with itself as the root stick and registered into the subcell in which the point (x_C, y_C) lies. In this work each stick is registered in a subcell indexed as $(\lfloor x_C \lfloor L \rfloor / L \rfloor, \lfloor y_C \lfloor W \rfloor / W \rfloor)$. According to this rule, a stick even centered exactly on a subcell boundary is also registered into a specific subcell. For the one-stick cluster minimum value of its component in the x-direction corresponds

[1] $\lfloor x \rfloor$ denotes the largest integer no greater than x.

to the point A (which is closer to the left boundary) $x_{\mathrm{A}} = x_{\mathrm{C}} - l/2\cos(\varphi)$, while maximum value corresponds to the point B (which is closer to the right boundary) $x_{\mathrm{B}} = x_{\mathrm{C}} + l/2\cos(\varphi)$, since $\cos(\varphi) \geq 0$ for $-\pi/2 \leq \varphi \leq \pi/2$. As already noted, these values should be initially stored for each one-stick cluster.

According to such a registration, a stick in a subcell (e.g., the one with bold white boundaries in Fig. 2.1(c)) is only possible to intersect sticks in the same or the neighboring subcells (the gray subcells in Fig. 2.1(c)) since the distance d between its center and any stick center in other sub-cells is greater than $l = 1$, i.e., the maximum possible center distance of two intersecting sticks. Then, it is only needed to check the connectivity property between the newly generated stick and those sticks belonging to the same or neighboring subcells. For algorithmic purposes, a stick can be presented as a vector $\overrightarrow{AB}$. Two sticks, presented as $\overrightarrow{A_1B_1}$ and $\overrightarrow{A_2B_2}$, intersect if the following conditions are simultaneously satisfied

$$\begin{aligned} \left(\overrightarrow{A_1B_1} \times \overrightarrow{A_1A_2}\right) \circ \left(\overrightarrow{A_1B_1} \times \overrightarrow{A_1B_2}\right) &\leq 0, \\ \left(\overrightarrow{A_2B_2} \times \overrightarrow{A_2A_1}\right) \circ \left(\overrightarrow{A_2B_2} \times \overrightarrow{A_2B_1}\right) &\leq 0. \end{aligned} \tag{2.1}$$

Note that these inequalities presented in a scalar form do not contain trigonometric functions. This significantly reduce a computing time required for checking a stick connectivity. When two sticks intersect, if they have the same root stick, i.e., belonging to the same cluster, nothing needs to be done; if not, the two corresponding clusters should be merged simply by adding a pointer from the root stick of the smaller cluster to that of the larger. It is known as a "weighted union" algorithm explained in Ref. [98]. Also, the x-component of a merged cluster should be obtained by overlapping the x-components of all clusters participating in the merger. In order to expedite the merging a "find with path compression" algorithm is also applied as in Ref. [98]. Following these processes, we repeat adding a random stick, registering it in an appropriate subcell, checking its connectivity with other sticks in the same and neighboring subcells, and merging, if necessary, the clusters until the x-component of a merged cluster completely covers the bottom boundary of the system. In this case, the system percolates for the first time and the total number

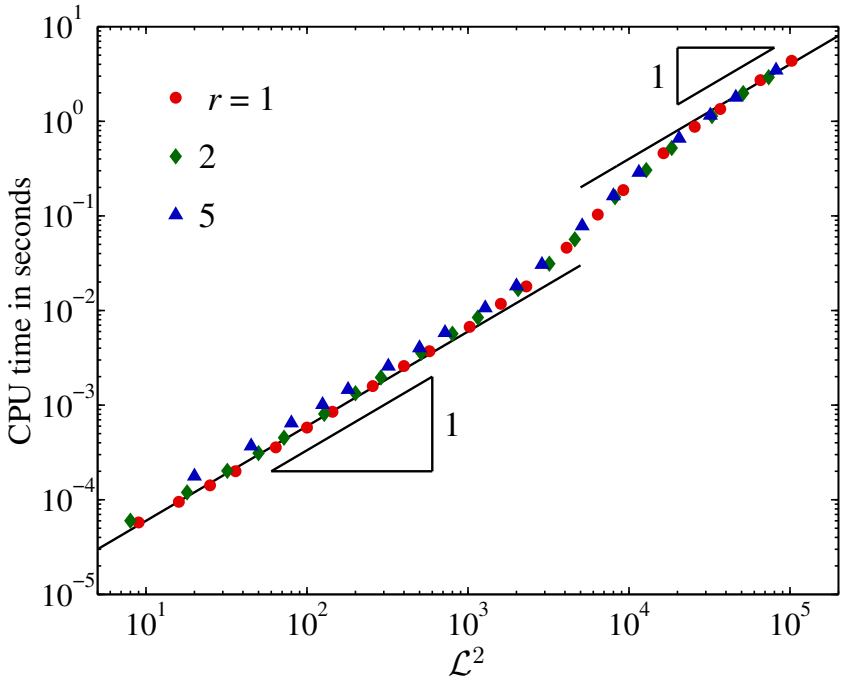

Figure 2.2: The average CPU time T for a single MC realization of a rectangular system with area $\mathcal{L}^2$ up to the percolation transition shown in logarithmic scale for three aspect ratios $r = 1, 2$, and 5. The simulations were run on a computer cluster configured with Intel Xeon CPUs with 2.33 GHz and 8 GB RAM. The solid lines $T \sim \mathcal{L}^2$ are only guides for the eye. As one can see, the running time depends linearly on the system area ($T \sim \mathcal{L}^2 \sim N_\mathrm{p}$) when the area is $\mathcal{L}^2 < 10^3$. The slope increases when the system can no longer fit entirely into the cache memory, forcing the CPU to access to slower RAM memory. With further increase of the system size, cache efficiency effects diminished and therefore, the running time becomes linear again (for $\mathcal{L}^2 > 10^4$).

of sticks is then recorded as N_p. By now, the whole simulation procedure for one realization is accomplished.

After performing the simulation procedure for N_MC realizations the different percolation properties can be obtained using appropriate statistical methods which will be explained bellow. In order to ensure the same precision for small and large systems we collected more than $N_\mathrm{MC} = 10^9$ Monte Carlo realizations for small systems $\mathcal{L} < 10$, down to $N_\mathrm{MC} = 10^7$ for the largest system $\mathcal{L} = 320$. These simulations are performed for a wide range of the aspect ratios, $0.1 \leq r \leq 10$. As one can see in Fig. 2.2, the algorithm running time until the system percolates for the first time is linearly dependent on the number of sticks at the criticality N_p,

i.e., linearly dependent on the system area $\mathcal{L}^2$, because $N_\mathrm{p} \sim \mathcal{L}^2$. The running time slows down when the computer is forced to access to its slower memory parts, causing higher slope with increase of the system size $\mathcal{L}$. With further increase of the system size, cache efficiency effects diminished and therefore, the running time becomes linear again (for $\mathcal{L}^2 > 10^4$). The running time behavior is almost identical for rectangular systems with different aspect ratios r, as shown in Fig. 2.2.

2.1.2 Calculation of average stick percolation density and standard deviation

Percolation probability function $R_{N,\mathcal{L},r}$ is the probability that the system with N sticks, normalized size $\mathcal{L}$, and aspect ratio r percolates. The percolating probability function $R_{N,\mathcal{L},r}$ for N sticks can be simply obtained by dividing the number of realizations that satisfy the following condition $N_\mathrm{p} \leq N$ by the total number of realizations N_MC. It is convenient to pass from the discrete percolation probability function $R_{N,\mathcal{L},r}$ for N sticks to a probability function $R_{n,\mathcal{L},r}$ for arbitrary stick density n, see Ref. [101]. This discrete-to-continuum transition cannot be obtained with arbitrary precision simply using the relation $n = N/\mathcal{L}^2$. In continuum-percolation processes this can be resolved by convolving all the measured observables with the Poisson distribution in order to generate a common "canonical ensemble" for any value of the stick density n, as shown in Ref. [101], so

$$R_{n,\mathcal{L},r} = \sum_{N=0}^{\infty} \frac{(n\mathcal{L}^2)^N e^{-n\mathcal{L}^2}}{N!} R_{N,\mathcal{L},r}. \tag{2.2}$$

Using the percolation probability distribution function defined as $P_{n,\mathcal{L},r} = \partial R_{n,\mathcal{L},r}/\partial n$, the average stick percolation density at which, for the first time, a percolating cluster connects boundaries of the system is

$$\langle n \rangle_{\mathcal{L},r} = \int_0^\infty n P_{n,\mathcal{L},r} dn = \frac{1}{\mathcal{L}^2} \sum_{N=0}^{\infty} (1 - R_{N,\mathcal{L},r}), \tag{2.3}$$

where the last equality follows from integrating by parts. Another important parameter of the probability distribution function, $P_{n,\mathcal{L},r}$, is variance $\Delta^2_{\mathcal{L},r} = \langle n^2 \rangle_{\mathcal{L},r} - \langle n \rangle^2_{\mathcal{L},r}$,

where $\langle n^2\rangle_{\mathcal{L},r}$ is calculated as

$$\langle n^2\rangle_{\mathcal{L},r}=\int_0^\infty n^2 P_{n,\mathcal{L},r}dn=\frac{2}{\mathcal{L}^4}\sum_{N=0}^{\infty}(N+1)(1-R_{N,\mathcal{L},r}). \tag{2.4}$$

Equations (2.3) and (2.4) allow calculations of the first two moments directly from discrete percolation probability function $R_{N,\mathcal{L},r}$. This is computationally more efficient since it avoids calculation of function $R_{n,\mathcal{L},r}$ with a high resolution. Detailed derivations of Eqs. (2.3) and (2.4) are given in Appendix A. Also, the standard errors propagations of the analyzed variables are given in Appendix B.

2.2 Generalized scaling function for percolation moments

The percolation probability function is related to the universal scaling function [91]

$$R_{n,\mathcal{L},r} = F(\hat{x},\{\hat{y}_i\},\hat{z}). \tag{2.5}$$

The arguments of the universal scaling function F are $\hat{x} = A(n-n_c)\mathcal{L}^{1/\nu}$, $\hat{y}_i = B_i\omega_i\mathcal{L}^{-\theta_i}$, and $\hat{z} = C\ln(r)$, where A, $\{B_i\}$, and C are the nonuniversal metric factors, $\{\omega_i\}$ are the irrelevant variables, and $\{\theta_i\}$ are the corrections to scaling exponents, $(i = 1, 2, ...)$. Using free boundary conditions and considering two complementary systems – the sticks and empty space around the sticks – we can conclude that either the sticks percolate in one direction or the empty space percolates in the opposite direction:

$$F(\hat{x},\{\hat{y}_i\},\hat{z}) + F^*(\hat{x}^*,\{\hat{y}_i^*\},\hat{z}^*) = 1, \tag{2.6}$$

where quantities denoted by star refer to the empty space. The sticks and empty space around the sticks are dual systems. Hence, the empty space occupancy n^* can be presented as $n^* = n_\infty - n$, and the critical occupancy of the empty space is then $n_c^* = n_\infty - n_c$, where $n_\infty \to \infty$ is the total space occupancy. Using the universality of the percolation probability function, which predicts that for dual systems universal scaling functions F and F^* are equal, and noting that $\hat{x}^* = A^*(n^*-n_c^*)\mathcal{L}^{1/\nu} = A^*(n_\infty - n - (n_\infty - n_c))\mathcal{L}^{1/\nu} = -(A^*/A)\hat{x}$, $\hat{y}_i^* = (B_i^*/B_i)\hat{y}_i$, and $\hat{z}^* = C^*\ln(1/r) =$

$-(C^*/C)\hat{z}$, we may rewrite the previous equation in the form

$$F(\hat{x},\{\hat{y}_i\},\hat{z}) + F(-(A^*/A)\hat{x},\{(B_i^*/B_i)\hat{y}_i\},-(C^*/C)\hat{z}) = 1. \tag{2.7}$$

Taking the derivative with respect to $\hat{x}$, $\hat{y}_i$, or $\hat{z}$ and evaluating the derivatives at $\hat{x} = \hat{y}_i = \hat{z} = 0$, we find that nonuniversal metric factors for dual systems satisfy

$$\begin{aligned} A^* &= A, \\ B_i^* &= -B_i, \\ C^* &= C. \end{aligned} \tag{2.8}$$

Finally, we obtain that the universal scaling function behaves as

$$F(\hat{x},\{\hat{y}_i\},\hat{z}) + F(-\hat{x},\{-\hat{y}_i\},-\hat{z}) = 1. \tag{2.9}$$

Evaluating the previous expression at $\hat{x} = \hat{y}_i = \hat{z} = 0$, i.e., at $n = n_c, \mathcal{L} \to \infty, r = 1$, we obtain

$$F(0,\{0\},0) = \frac{1}{2}. \tag{2.10}$$

This is in agreement with Cardy's analytical model [88], which predicts that the percolation probability at the percolation threshold n_c for infinitely large $\mathcal{L} \to \infty$ and symmetric system $r = 1$ is equal to $1/2$. This property will be discussed in more detail in section 2.5.

Taking the derivative of Eq. (2.9) with respect to $\hat{x}$, $\hat{y}_i$, and $\hat{z}$ and evaluating the derivatives at $\hat{x} = \hat{y}_i = \hat{z} = 0$, we conclude that $\partial^m F/\partial\hat{x}^j\partial\hat{y}_1^{k_1}...\,\partial\hat{z}^l\big|_0 = 0$, for m even, where $m = j + \sum_i k_i + l > 0$. Expanding the percolation probability function near the critical point we find that

$$F(\hat{x},\{\hat{y}_i\},\hat{z}) = F(0,\{0\},0) + f_0(\hat{x},\hat{z}) + \sum_{i=1}^{\infty} f_i(\hat{x},\hat{z})\hat{y}_i + ... \tag{2.11}$$

where the functions $f_0(\hat{x},\hat{z})$ and $f_i(\hat{x},\hat{z})$ are defined by

$$f_0(\hat{x},\hat{z}) = \sum_{j,l=0}^{\infty} \frac{1}{j!l!} \left.\frac{\partial^{j+l} F}{\partial \hat{x}^j \partial \hat{z}^l}\right|_0 \hat{x}^j \hat{z}^l, \text{ for } j+l \text{ odd}, \tag{2.12}$$

and

$$f_i(\hat{x},\hat{z}) = \sum_{j,l=0}^{\infty} \frac{1}{j!l!} \left.\frac{\partial^{j+l+1} F}{\partial \hat{x}^j \partial \hat{y}_i \partial \hat{z}^l}\right|_0 \hat{x}^j \hat{z}^l, \text{ for } j+l \text{ even}. \tag{2.13}$$

Since the percolation probability distribution function $P_{n,\mathcal{L},r} = \partial R_{n,\mathcal{L},r}/\partial n$ gives the probability distribution for a system of size $\mathcal{L}$ and aspect ratio r to percolate for the first time at stick density n, we can define the moments of this distribution

$$\mu_k = \int_0^{\infty} (n - n_c)^k \frac{\partial R_{n,\mathcal{L},r}}{\partial n} dn. \tag{2.14}$$

The percolation probability distribution function for the infinite $\mathcal{L} \to \infty$ and almost symmetric system $r \to 1$ can be approximated with zero when the stick density n is outside $\delta n \to 0$ region around n_c, i.e., $P_{|n-n_c|>\delta n, \mathcal{L}\to\infty, r\to 1} \approx 0$, see Fig. 2.3(e). Therefore, the kth percolation moment near the critical point can be determined as

$$\mu_k = \int_{n_c-\delta n}^{n_c+\delta n} (n - n_c)^k \frac{\partial R_{n,\mathcal{L},r}}{\partial n} dn. \tag{2.15}$$

Finally, using the universal scaling function F with appropriate arguments $\hat{x}$, $\{\hat{y}_i\}$, and $\hat{z}$, the above expression becomes

$$\mu_k = A^{-k} \mathcal{L}^{-k/\nu} \int_{-A\delta n \mathcal{L}^{1/\nu}}^{A\delta n \mathcal{L}^{1/\nu}} \hat{x}^k \frac{\partial F}{\partial \hat{x}} d\hat{x}. \tag{2.16}$$

Substituting Eqs. (2.11)-(2.13) into Eq. (2.16) we obtain the generalized scaling function for the kth percolation distribution moment:

$$\mu_k(\{\hat{y}_i\},\hat{z}) = \mathcal{L}^{-k/\nu} \left(g_0(\hat{z}) + \sum_{i=1}^{\infty} g_i(\hat{z}) \hat{y}_i + \ldots \right), \tag{2.17}$$

where we introduce general function $g_0(\hat{z})$

$$g_0(\hat{z}) = A^{-k} \sum_{j,l=0}^{\infty} \frac{1}{j!l!} \frac{\partial^{j+l} F}{\partial \hat{x}^j \partial \hat{z}^l}\bigg|_0 \frac{j}{j+k} \hat{x}^{j+k} \bigg|_{-A\delta n \mathcal{L}^{1/\nu}}^{A\delta n \mathcal{L}^{1/\nu}} \hat{z}^l, \text{ for } j+l \text{ odd} \tag{2.18}$$

and general functions $g_i(\hat{z})$

$$g_i(\hat{z}) = A^{-k} \sum_{j,l=0}^{\infty} \frac{1}{j!l!} \frac{\partial^{j+l+1} F}{\partial \hat{x}^j \partial \hat{y}_i \partial \hat{z}^l}\bigg|_0 \frac{j}{j+k} \hat{x}^{j+k} \bigg|_{-A\delta n \mathcal{L}^{1/\nu}}^{A\delta n \mathcal{L}^{1/\nu}} \hat{z}^l, \text{ for } j+l \text{ even}. \tag{2.19}$$

Nonzero values of the general functions given by Eqs. (2.18) are obtained only for $j+k$ odd. Therefore, for odd k, j is even, and then $g_0(\hat{z})$ is an odd function and $g_i(\hat{z})$ are even functions of $\hat{z}$. On the other hand, for even k, j is odd, and then $g_0(\hat{z})$ is even and $g_i(\hat{z})$ are odd functions. Therefore, the observed parity of prefactors in respect to $\hat{z}$ should be independent of the type of the system.

From Eq. (2.17) the scaling behavior of the $\langle n \rangle_{\mathcal{L},r}$ can be described by the generalized scaling function with aspect-ratio-dependent coefficients

$$\langle n \rangle_{\mathcal{L},r} = n_c + \mathcal{L}^{-1/\nu} \sum_{i=0}^{\infty} a_i(r) \mathcal{L}^{-\theta_i}. \tag{2.20}$$

where $\{\theta_i\}$ are the corrections to scaling exponents. The zeroth-order correction to exponent θ_0 should be zero [2]. In analogy to $\langle n \rangle_{\mathcal{L},r}$, for variance $\Delta^2_{\mathcal{L},r}$ we introduce the following expansion

$$\Delta^2_{\mathcal{L},r} = \mathcal{L}^{-2/\nu} \sum_{i=0}^{\infty} b_i(r) \mathcal{L}^{-\theta_i}. \tag{2.21}$$

From Eq. (2.17) and the parity of $g_0(\hat{z})$ and $g_i(\hat{z})$, we can estimate the zeroth-order and the first-order prefactors for $\langle n \rangle_{\mathcal{L},r}$ and $\Delta^2_{\mathcal{L},r}$ near $\ln(r) = 0$, i.e., $\hat{z} = 0$, as follows

$$\begin{aligned} a_0(r) &\approx a_{0,0} \ln(r) + a_{0,1} \ln^3(r), \\ a_1(r) &\approx a_{1,0} + a_{1,1} \ln^2(r), \end{aligned} \tag{2.22}$$

and

$$\begin{aligned} b_0(r) &\approx b_{0,0} + b_{0,1} \ln^2(r), \\ b_1(r) &\approx b_{1,0} \ln(r) + b_{1,1} \ln^3(r), \end{aligned} \tag{2.23}$$

where $a_{i,j}$ and $b_{i,j}$ are nonuniversal coefficients.

2.3 Finite-size scaling of average stick percolation density and standard deviation

The results for percolation probability $R_{n,\mathcal{L},r}$ and distribution $P_{n,\mathcal{L},r}$ function are shown in Fig. 2.3. One observes that the slope of percolation probability function $R_{n,\mathcal{L},r}$ increases with the increase of the system size. The percolation probability function curves intersect approximately at n_c. The fine behavior of percolation probability function at n_c (see insets of Fig. 2.3) will be discussed in section 2.5. With the increasing system size, the standard deviation of probability distribution function decreases to zero. Also, average stick percolation density $\langle n \rangle_{\mathcal{L},r}$, which corresponds roughly to maximum of probability distribution function $P_{n,\mathcal{L},r}$, approaches to the percolation threshold n_c. For $r < 1$, $\langle n \rangle_{\mathcal{L},r}$ converges to n_c from below with increase of the system size $\mathcal{L}$. The reason for this is that narrow finite systems will be spanned already at lower densities than n_c. For $r > 1$, $\langle n \rangle_{\mathcal{L},r}$ converges from above, while for symmetric systems ($r = 1$) is roughly centered at n_c, see Fig. 2.3.

From Fig. 2.4, one can see that average stick percolation density $\langle n \rangle_{\mathcal{L},r}$ for aspect ratio higher than 1 is a monotonically decreasing function of the system size $\mathcal{L}$. Somewhat surprising, for aspect ratios lower than 1, $\langle n \rangle_{\mathcal{L},r}$ is not a monotonic function and has a local minimum; i.e., for small systems $\langle n \rangle_{\mathcal{L},r}$ is a decreasing function, which passes through n_c, reaches a minimum, and after that converges to n_c from below. In the inset of Fig. 2.4, one can see that for large system sizes all the curves show power-law convergence to the percolation threshold n_c with exponent $-1/\nu$, except in the symmetric case, i.e., $r = 1$, where the exponent is $-1/\nu - \theta_1$. Absolute values of the leading-order prefactors are the same for aspect ratios r and $1/r$, which

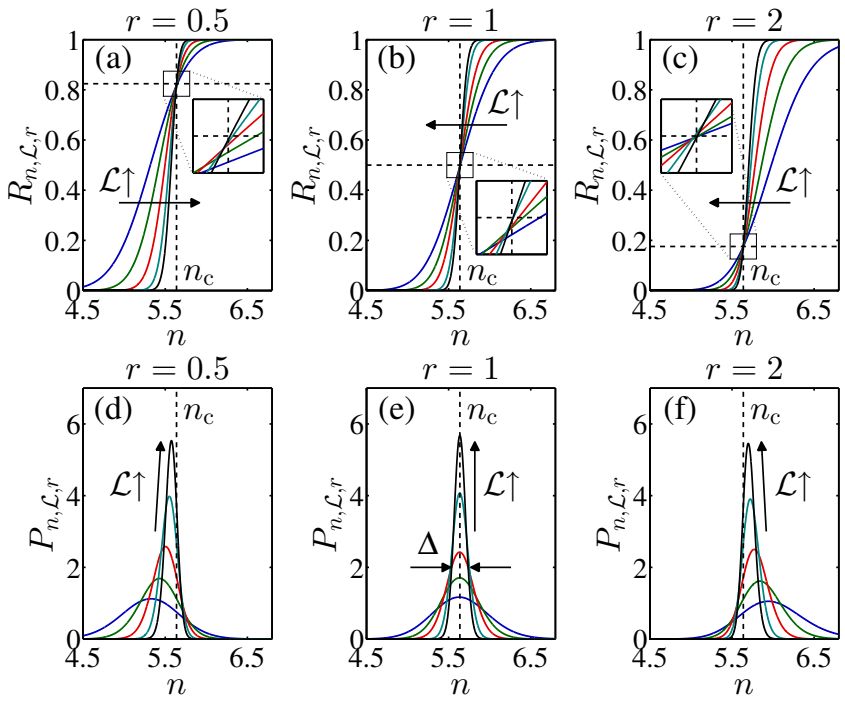

Figure 2.3: Percolation probability function $R_{n,\mathcal{L},r}$ (a), (b), and (c) and probability distribution function $P_{n,\mathcal{L},r}$ (d), (e), and (f) for stick percolation on rectangular systems with free boundary conditions and increasing system size from $\mathcal{L} = 20$ to 200 for three aspect ratios $r = 0.5, 1$, and 2. The direction of the increase of $\mathcal{L}$ is indicated on graphs. The vertical dashed lines denote the value for the percolation threshold n_c, while the horizontal dashed lines denote the percolation probability of the infinite systems at the percolation threshold $R_{n_c,\mathcal{L}\to\infty,r}$. Insets: The fine behavior of percolation probability function at the critical point n_c.

is in accordance with the prefactors parity explained in the previous section.

The higher exponent of symmetric systems comes from the basic physics of percolation, that is, connectedness. We can illustrate this using a simplified image of site percolation by introducing the quantity $R(p)$ as the probability that the sites with occupancy p form a spanning path. The percolation probability $R(p)$ and occupancy p are equivalent to the percolation probability function $R_{n,\mathcal{L},r}$ and stick density n, respectively. In this image, a cell coming out of the renormalization transformation (coarse graining) is occupied only if it contains a set of sites that span this cell. The universal scaling function introduced in the previous section reflects the fact that the probability of the spanning system at the percolation threshold $R(p_c)$ remains unaltered under this transformation [2]. Therefore, the fixed point of this

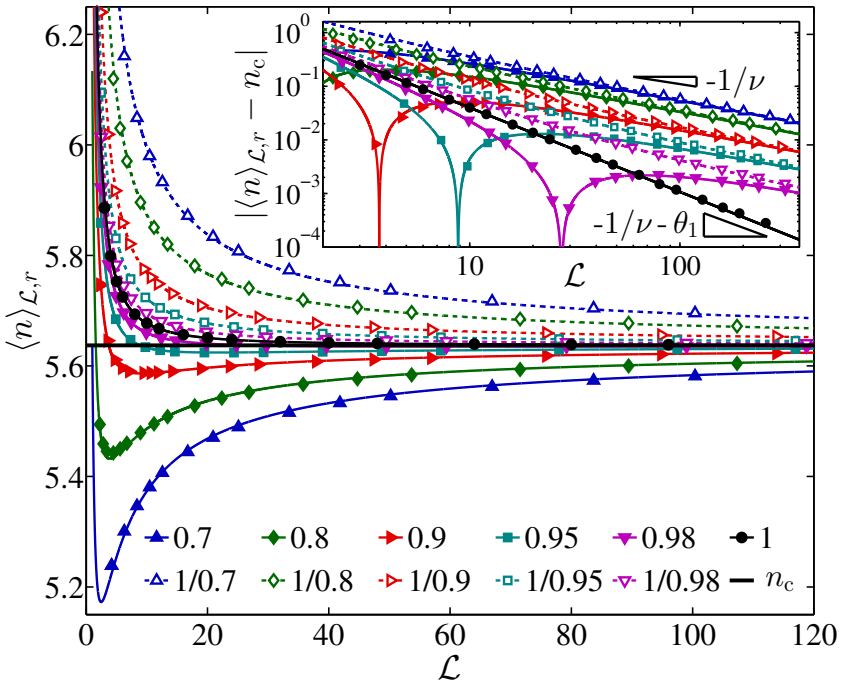

Figure 2.4: The dependence of the average stick percolation density $\langle n \rangle_{\mathcal{L},r}$ on the system size $\mathcal{L}$ and aspect ratio r. The points are obtained from Monte Carlo simulations and calculated using Eq. (2.3). The values are given for aspect ratios $r = 0.7, 0.8, 0.9, 0.95, 0.98, 1$ (filled) and their inverse values $r = 1/0.7, 1/0.8, 1/0.9, 1/0.95, 1/0.98$ (transparent). The horizontal bold line denotes the expected value for the percolation threshold n_c. The lines represent the average stick percolation density $\langle n \rangle_{\mathcal{L},r}$ modeled using Eqs. (2.20) and (2.22), coefficients $a_{i,j}$ given in Table 2.1, and the corrections to scaling exponents $\theta_0 = 0$ and $\theta_1 = 0.82$. Inset: The same data are shown in logarithmic scale to demonstrate the same power law convergence of the r and $1/r$ pairs.

system, i.e., the critical percolation threshold, p_c should satisfy relation $p_c = R(p_c)$. We can expand the percolation probability around the percolation threshold p_c, $|R(p) - R(p_c)| \approx dR/dp|_{p_c}|p - p_c|$. Also, if we renormalize the lattice close to p_c by a length factor b, the characteristic length changes as ξ/b. Since $\xi \sim |p - p_c|^{-\gamma}$, we can write another relation, $|R(p) - R(p_c)|^{-\gamma} \approx |p - p_c|^{-\gamma}/b$, connecting characteristic lengths before and after renormalization. From these two relations one can conclude that the critical exponent should be

$$-1/\gamma \approx \frac{\ln dR/dp|_{p_c}}{\ln 1/b}. \tag{2.24}$$

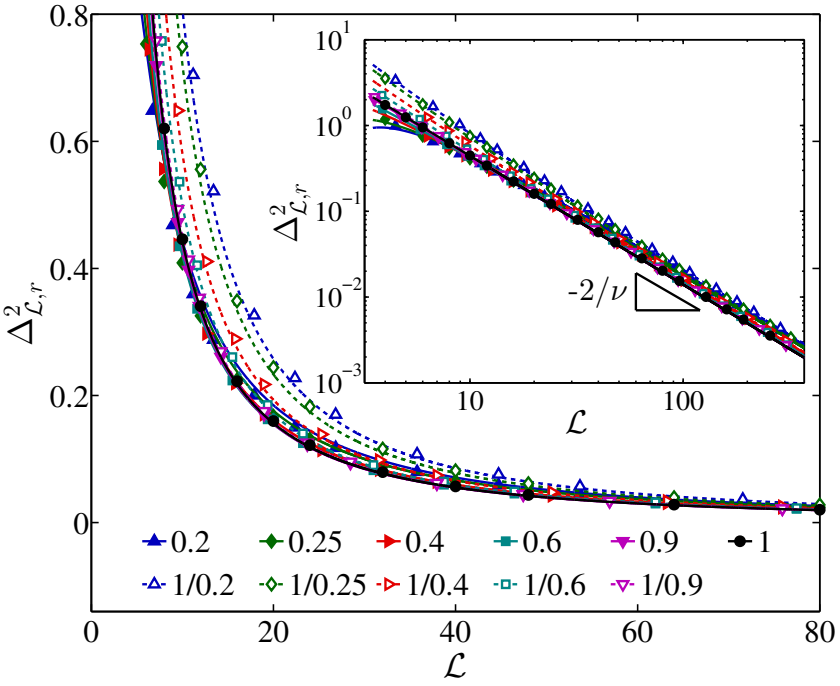

Figure 2.5: The dependence of the the percolation probability distribution function variance $\Delta^2_{\mathcal{L},r}$ on the system size $\mathcal{L}$ and aspect ratio r. The points are obtained from Monte Carlo simulations and calculated using Eqs. (2.3) and (2.4). The values are given for aspect ratios $r = 0.2, 0.25, 0.4, 0.6, 0.9, 1$ (filled) and their inverse values $r = 1/0.2, 1/0.25, 1/0.4, 1/0.6, 1/0.9$ (transparent). The lines represent the variance $\Delta^2_{\mathcal{L},r}$ modeled using Eqs. (2.21) and (2.23), coefficients $b_{i,j}$ given in Table 2.1, and the corrections to scaling exponents $\theta_0 = 0$ and $\theta_1 = 0.82$. Inset: The same data are shown in logarithmic scale to demonstrate the same power law convergence for all aspect ratios r.

From Fig. 2.3, one can see that probability density $P_{n_c,\mathcal{L},r}$ which is derivative of $R_{n,\mathcal{L},r}$ at n_c is always larger for symmetric systems than for asymmetric systems of the same size. Therefore, from Eq. (2.24), one expects higher absolute value of the exponent in symmetric compared to asymmetric systems. Another conclusion one can draw from this analysis is that the observed exponents are a result of the interplay of the characteristic length and the system shape. Usually, such behavior is attributed to a competition between two-dimensional and three-dimensional (or one-dimensional and two-dimensional), e.g., in the Ising model for slab geometries; see Ref [3]. In this system we observe that there is sharp transition in the nature of scaling when we pass from the symmetric to asymmetric system, and a competition between exponents characteristic for symmetric and asymmetric systems.

As illustrated in Fig. 2.5, the variance of percolation probability distribution function $\Delta^2_{\mathcal{L},r}$ for all aspect ratios r is a monotonically decreasing function of the system size $\mathcal{L}$. We note that the variance of narrow systems $\Delta^2_{\mathcal{L},r<1}$ is approximately equal to the variance of symmetric systems $\Delta^2_{\mathcal{L},r=1}$ with the same size $\mathcal{L}$. In the inset of Fig. 2.5, one can see that all presented curves show power-law convergence to zero with exponent $-2/\nu$, which is in accordance with Eqs. (2.21) and (2.23).

2.4 Prefactors and exponents of average stick percolation density and standard deviation

From Monte Carlo simulation data we have obtained the two leading-order terms of $\langle n \rangle_{\mathcal{L},r}$ in Eq. (2.20) by fitting. A detailed description of the fitting analysis is given in Appendix C. The results of the analysis are shown in Fig. 2.6. The zeroth-order prefactor $a_0(r)$ is zero for symmetric system $r = 1$, and it is an odd function on a logarithmic scale, i.e., $a_0(r) = -a_0(1/r)$, as shown in detail in Appendix C. The first-order prefactor $a_1(r)$ is an even function, i.e., $a_1(r) = a_1(1/r)$, as also shown in Appendix C. The fitting coefficients $a_{i,j}$ for prefactors a_0 and a_1, given in Table 2.1, are calculated using the least-squares fitting methods. The influence of higher order terms of $\langle n \rangle_{\mathcal{L},r}$ was comparable to or smaller than the simulation data error and we could not extract them with sufficient precision. As shown in Fig. 2.6(b), the zeroth-order correction $\theta_0 = 0$ is equal to zero, while for the first-order correction we obtain $\theta_1 = 0.82(2)$ for $r = 1$, which is consistent with Refs. [87, 89]. The residual aspect ratio dependence of θ_1 cannot be further analyzed without provision of retaining the first two terms in Eq. (2.20). However, for all studied values of aspect ratio $0.1 < r < 10$, the average stick percolation density $\langle n \rangle_{\mathcal{L},r}$, modeled using the two leading-order terms in Eqs. (2.20) and (2.22), coefficients $a_{i,j}$ given in Table 2.1, and the corrections to scaling exponents $\theta_0 = 0$ and $\theta_1 = 0.82$, shows an excellent agreement with the MC results over the whole range of the system size $\mathcal{L}$, see Fig. 2.4.

From Eq. (2.20) one can see that the system size where the average stick percolation density reaches its minimum is $\mathcal{L}_{\min} \approx (-a_1(r)/a_0(r)(1+\nu\theta_1))^{1/\theta_1}$, see

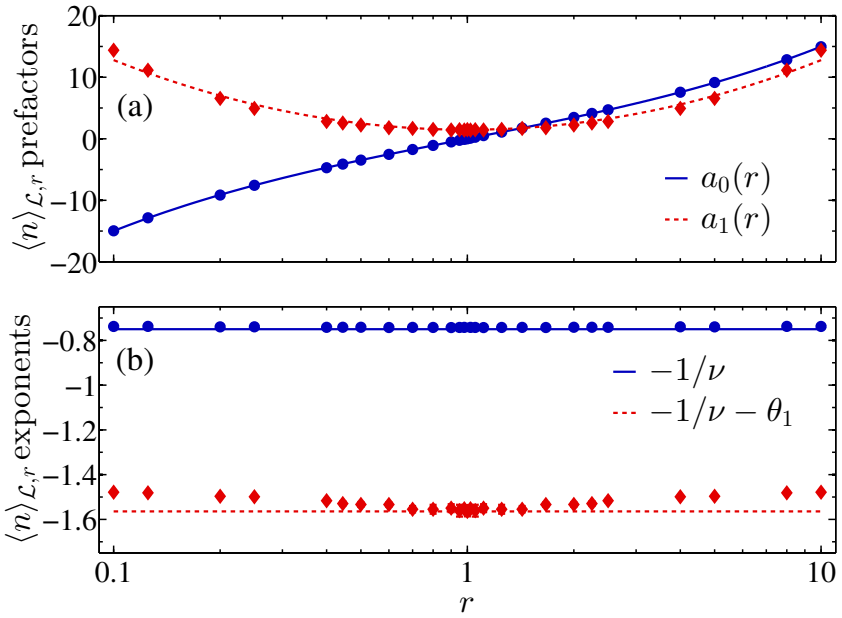

Figure 2.6: Prefactors (a) and exponents (b) are shown for the two leading-order terms of generalized scaling function for average stick percolation density $\langle n\rangle_{\mathcal{L},r}$ given by Eq. (2.20). The zeroth-order prefactor is an odd function on a logarithmic scale, i.e., $a_0(r) = -a_0(1/r)$, and the zeroth-order exponent is $-1/\nu$ (solid lines). The first-order prefactor is an even function, i.e., $a_1(r) = a_1(1/r)$, and the first-order correction to the scaling exponent is $\theta_1 = 0.82(2)$ for $r = 1$ (dashed lines).

Fig. 2.4. The size $\mathcal{L}_{\min}$ is a real number only for narrow systems, i.e., $r < 1$, because the prefactors $a_0(r)$ and $a_1(r)$ have different signs only in that case, see Fig. 2.6(a). When r approaches one from bellow, i.e., $r \to 1^-$, the two leading-order prefactors converge to $a_0(r) \to a_{0,0}\ln(r)$ and $a_1(r) \to a_{1,0}$ (see Eq. (2.22)) and consequently, $\mathcal{L}_{\min}$ diverges as $1/\ln(r)$, i.e., $\mathcal{L}_{\min} \sim 1/\ln(r) \to \infty$. In that case, for small system sizes $\mathcal{L} < \mathcal{L}_{\min}$, the first-order term of the average stick percolation density $\langle n\rangle_{\mathcal{L},r}$ is dominant compared to the zeroth-order term, see Fig. 2.4.

Table 2.1: The improved values of the coefficients $a_{i,j}$ and $b_{i,j}$, where $i, j \in \{0, 1\}$, compared to those given in our previously published paper [4]. The improved values are obtained using the least-squares fitting method as explained in Appendix C.

	0, 0	0, 1	1, 0	1, 1
$a_{i,j}$	4.861(6)	0.310(4)	1.48(5)	2.1(2)
$b_{i,j}$	13.98(7)	2.24(4)	15.4(3)	3.2(2)

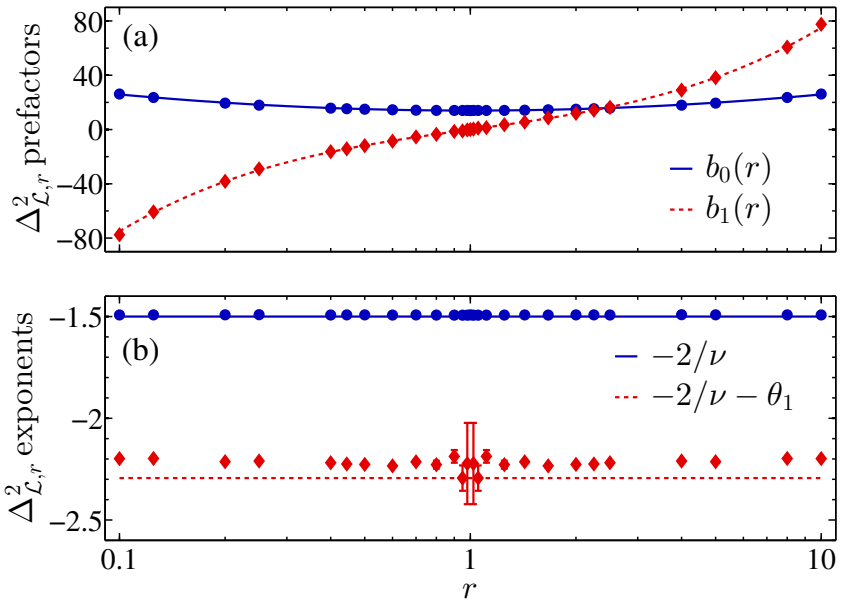

Figure 2.7: Prefactors (a) and exponents (b) are shown for the two leading-order terms of generalized scaling function for stick percolation density variance $\Delta^2_{\mathcal{L},r}$ given by Eq. (2.21). The zeroth-order prefactor is an even function on a logarithmic scale, i.e., $b_0(r) = b_0(1/r)$, and the zeroth-order exponent is $-2/\nu$ (solid lines). The first-order prefactor is an odd function, i.e., $b_1(r) = -b_1(1/r)$, and the first-order correction to the scaling exponent is $\theta_1 = 0.80(5)$ for $r = 0.95$ (dashed lines).

The prefactors and exponents of stick percolation density variance $\Delta^2_{\mathcal{L},r}$ for the two leading-order terms in Eq. (2.21) are shown in Fig. 2.7. The prefactors and exponents are obtained by fitting, as explained in Appendix C. The fitting coefficients $b_{i,j}$ for prefactors b_0 and b_1 are given in Table 2.1 and the obtained prefactor dependences on the system aspect ratio r are shown in Fig. 2.7(a). The zeroth-order prefactor of $\Delta^2_{\mathcal{L},r}$ is an even function on a logarithmic scale, i.e., $b_0(r) = b_0(1/r)$, as one can also see from a coarse observation of the percolation probability distribution function in Fig. 2.3. Asymmetry of the variance, i.e., $\Delta^2_{\mathcal{L},r} \neq \Delta^2_{\mathcal{L},1/r}$, is the first-order effect, because the first-order prefactor is an odd function on a logarithmic scale, i.e., $b_1(r) = -b_1(1/r)$, as shown in Appendix C. Also, for all studied values of the aspect ratio $0.1 < r < 10$, the stick percolation density variance $\Delta^2_{\mathcal{L},r}$, modeled using the first two terms in Eqs. (2.21) and (2.23), coefficients $b_{i,j}$ given in Table 2.1, and corrections to scaling exponents $\theta_0 = 0$ and $\theta_1 = 0.82$, shows an excellent agreement with the MC results over the whole range of the system size $\mathcal{L}$, see Fig. 2.5.

2.5 Percolation probability function at percolation threshold

We also investigate the scaling behavior of the percolation probability at the percolation threshold $R_{n_c,\mathcal{L},r}$ expanding the universal scaling function $F(0,\{\hat{y}_i\},\hat{z})$ near the infinite-size system, i.e., $\mathcal{L}\to\infty$, as follows

$$F(0,\{\hat{y}_i\},\hat{z}) = F(0,\{0\},\hat{z}) + \sum_{i=1}^{\infty}\frac{\partial F}{\partial \hat{y}_i}\hat{y}_i + \dots \,. \tag{2.25}$$

This relation is equivalent to the following scaling function

$$R_{n_c,\mathcal{L},r} = R_{n_c,\mathcal{L}\to\infty,r} + \sum_{i=1}^{\infty} c_i(r)\mathcal{L}^{-\theta_i} + \dots, \tag{2.26}$$

where $c_i(r)$ are aspect-ratio-dependent scaling prefactors. Instead of the previous expansion, in Ref. [93] was found that the best fit for the percolation probability function at the percolation threshold n_c is given by

$$R_{n_c,\mathcal{L},r} = R_{n_c,\mathcal{L}\to\infty,r} + \frac{c_1(r)}{\mathcal{L}} + \frac{c_2(r)}{\mathcal{L}^2}. \tag{2.27}$$

We suppose that the higher order terms in the generalized scaling function given by Eq. (2.26) cannot be neglected and their comprehensive influence is probably superposed resulting in only two terms, as shown in Eq. (2.27). In order to confirm that, we find that the previous equation represents an excellent fit to the percolation probability values at the percolation threshold $R_{n_c,\mathcal{L},r}$ for all analyzed system sizes $\mathcal{L}$ and aspect ratios r. Therefore, the results for prefactors $c_1(r)$ and $c_2(r)$ obtained using Eq. (2.27) for fitting data are shown in Fig. 2.8. For the two limiting cases ($r < 0.1$ and $r > 10$), the prefactors are close to zero, which is consistent with the behavior observed in Fig. 2.3. Between these two limiting cases, one can observe that both prefactors are close to zero for $r = 2.25(5)$. This means that the percolation probability at the percolation threshold is independent of the system size $\mathcal{L}$ when the system aspect ratio r is approximately equal to 2.25, i.e., $R_{n_c,\mathcal{L},r\approx 2.25} \approx 0.135$. The scale invariance, i.e., $R_{n_c,\mathcal{L},r} = R_{n_c,\infty,r}$, has been already seen and intuitively understood for bond percolation in symmetric systems, where $R_{p_c=0.5,r=1} = 1/2$ is

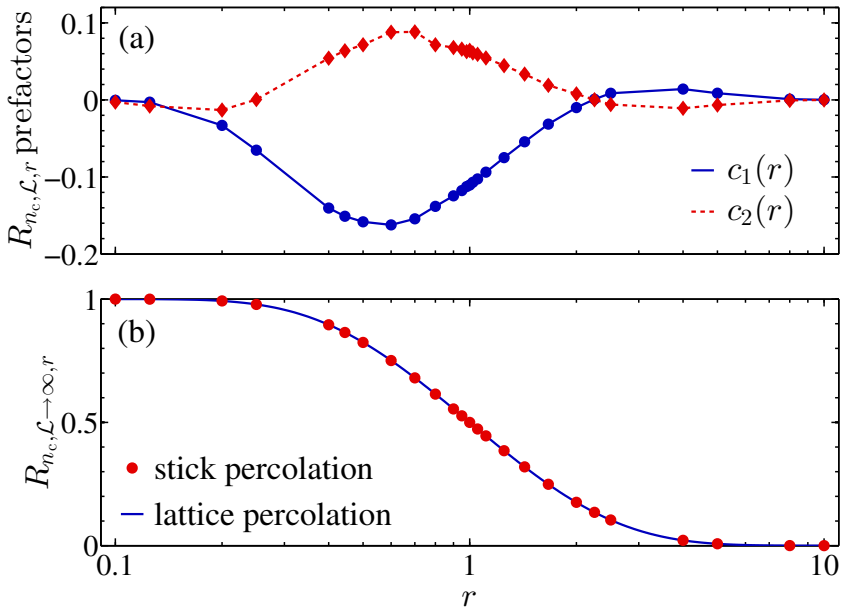

Figure 2.8: (a) Prefactors for finite-size scaling of the percolation probability at the percolation threshold $R_{n_c,\mathcal{L},r}$ are shown for the two leading-order terms. (b) The percolation probability at the percolation threshold for infinitely large systems $R_{n_c,\mathcal{L}\to\infty,r}$. The points represent Monte Carlo data for stick percolation, while the line represents results of Cardy's model for the lattice percolation. The error bars are much smaller than the size of the points for all r.

also independent of the system size $\mathcal{L}$; see Ref. [97]. The reason for the observed system size invariance of percolation probability at the threshold in the asymmetric stick system is the existence of multiple zeros of at least second order at this point in the universal scaling function. We note that this invariance can also be observed in insets of Fig. 2.3 where the fine behavior of percolation probability function at the critical point n_c is shown for different system sizes from $\mathcal{L} = 20$ to 200. For narrow systems ($r = 0.5$) shown in Fig. 2.3(a), as well as symmetric ones ($r = 1$) shown in Fig. 2.3(b), the percolation probability at the percolation threshold n_c approaches to its infinite-size value $R_{n_c,\mathcal{L}\to\infty,r}$ with increasing system size $\mathcal{L}$. On the other hand, for the systems shown in Fig. 2.3(c), which have the aspect ratio $r = 2$ close to its critical value 2.25(5), all percolation probability function curves intersect approximately at the same point, see inset of Fig. 2.3(c).

Finally, regarding the value of the percolation probability at the percolation threshold of the infinite system, we find that Cardy's analytical model derived for

the lattice percolation also describes our simulation data; see Fig. 2.8(b). The deviation between the analytical values for lattice and the Monte Carlo values for stick percolation is less than the statistical error of the simulation data, i.e., less than 10^{-5}. The percolation probability for the 2D stick system therefore satisfies $R_{n_c,\mathcal{L}\to\infty,r} + R_{n_c,\mathcal{L}\to\infty,1/r} = 1$. This relation can also be obtained from Eq. (2.9) considering duality of infinite-size systems at the percolation threshold, i.e., $F(0,\{0\},\hat{z}) + F(0,\{0\},-\hat{z}) = 1$.

2.6 Analytic model for the percolation probability function

Finally, we propose an analytic model for calculating the percolation probability function $R_{n,\mathcal{L},r}$ using a cumulative distribution function [50, 102]

$$R_{n,\mathcal{L},r} = \frac{1}{2}\left[1 + \mathrm{erf}\left(\frac{n - \langle n\rangle_{\mathcal{L},r}}{\sqrt{2}\Delta_{\mathcal{L},r}}\right)\right], \tag{2.28}$$

where $\langle n\rangle_{\mathcal{L},r}$ is the average stick percolation density modeled using Eqs. (2.20) and (2.22) and coefficients $a_{i,j}$ given in Table 2.1, $\Delta_{\mathcal{L},r}$ is the the percolation density standard deviation modeled using Eqs. (2.21) and (2.23) and coefficients $b_{i,j}$ given in Table 2.1, whereas $\mathrm{erf}(x) = 2\int_0^x e^{-t^2}dt/\sqrt{\pi}$ is the Gaussian error function.

The percolation probability functions $R_{n,\mathcal{L},r}$ for different aspect ratios and normalized system sizes are shown in Fig. 2.9. As already noted, the percolation probability function moves toward higher densities with increasing system aspect ratio r and becomes steeper with increasing normalized system size $\mathcal{L}$. As demonstrated in Fig. 2.9, the values obtained using the proposed model given by Eq. (2.28) represent an excellent fit to the data calculated using MC simulations, even for the systems with a relatively small normalized size $\mathcal{L} > 5$. Therefore, we conclude that the proposed analytic model can be used as an excellent approximation of the percolation probability function for all studied systems sizes with $\mathcal{L} > 5$ and all studied aspect ratios $0.1 < r < 10$.

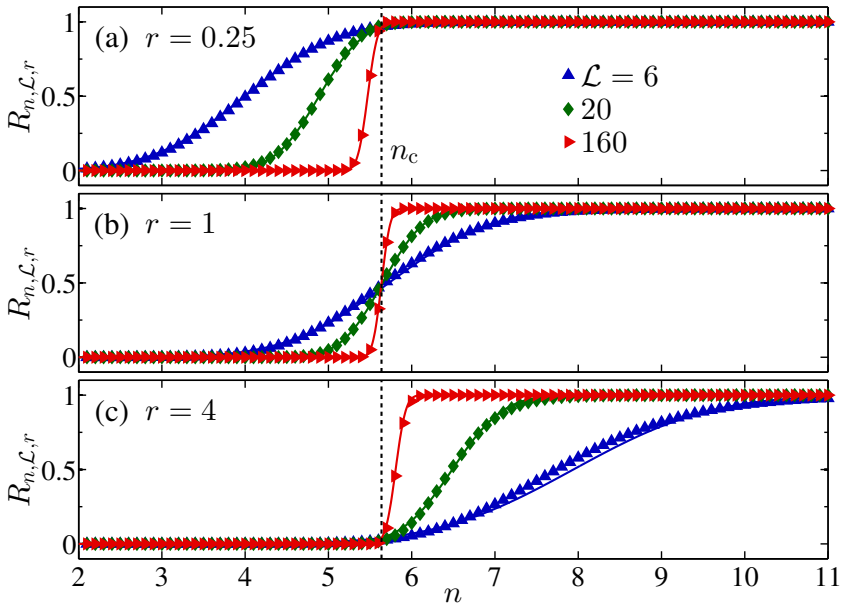

Figure 2.9: The percolation probability functions for different aspect ratios (a) $r = 0.25$, (b) 1, and (c) 4 and for three normalized system size values $\mathcal{L} = 6$, 20, and 160. The points are obtained from the MC simulations and calculated using Eq. 2.2. The solid lines denote values obtained from our analytic model for the percolation probability functions given by Eq. (2.28). The vertical dashed lines denote the percolation threshold value n_c.

2.7 Conclusions

In summary, based on the analysis of finite-size scaling in continuum two-dimensional systems, the generalized scaling law is introduced for average percolation density, standard deviation, and percolation probability at the percolation threshold. The presented methodology could be used to model accurately these properties for any percolating system. According to the generalized scaling function, an analytic model of the percolation probability function for two-dimensional systems is also proposed. We find that the zeroth-order prefactor of average percolation density is an odd function with respect to $\ln(r)$. This explains the faster convergence of average percolation density for symmetric systems than expected from general scaling arguments. We also observe that there is a characteristic aspect ratio for which percolation probability at the percolation threshold is system-size independent. In addition, for the infinite system, we find that the percolation probability at the critical threshold den-

sity shows excellent agreement with Cardy's prediction for lattice percolation. The presented results confirm that continuum percolation belongs to the same universality class as lattice percolation in the sense that the value of percolation probability at the threshold for infinitely large systems is the same for lattice and continuum percolation. One should note that a number of other features observed in this Chapter should be a common characteristic within the class, e.g., the existence of the aspect ratio where the percolation probability at the threshold is scale invariant and parity of the moments of the percolation probability distribution function. This opens up the question of the particle shape influence on prefactors, whether it is possible to find systems where the observed behaviors are more pronounced, and finally the question of the general form of the prefactors for describing different systems.

Chapter 3 From percolating to dense random nanowire networks: electrical conductivity and optical transparency investigation

Across different application areas, such as thin-film solar cells, organic light emitting diodes, and many touch screen applications, two critical performance criteria for the transparent conductors are their electrical conductivity and optical transparency. Therefore, the electrical conductivity and optical transparency dependencies on the NW density and system geometry needs to be taken into account in any device design based on random NW networks [24]. The percolation theory predicts that the electrical conductivity of the composite materials with the conductive filler density n above, but close to the percolation threshold n_c, increases with the density by a power scaling law $\sigma \sim (n - n_c)^t$, with the universal conductivity exponent $t \approx 1.29$ for two-dimensional (2D) systems [2]. While the conductivity scaling law is expected to be applicable only near the percolation threshold, in many experiments the scaling law was used over a much larger range of concentrations, but with the nonuniversal values of the conductivity exponent [18, 28–30].

In this Chapter, the conductivity of two-dimensional random NW networks is investigated from the percolation threshold up to ten times the percolation threshold density using an extensive Monte Carlo simulation study. We show that it is not appropriate to use a simple scaling law to describe the conductivity dependence on the density, both for finite and dense networks. Based on our Monte Carlo simulation results, we propose a model that explicitly depends on the NW density and junction-to-NW conductance ratio. The model describes the transition from the conductivity determined by the structure of a percolating cluster to the conductivity of the dense random NW networks. The proposed model is motivated by the

observed structural characteristic of the random NW networks (i.e., the density of total NWs and contacts involved in the current flow through the system). The model is also valid for the different stick-like nanoparticles. The finite-size scaling effects are also included in the description. Finally, using the proposed model and an analytical approximation for the density-dependent optical transmittance, we quantify a dependence of the optical transmittance on the electrical conductivity for random NW networks. We also propose a procedure for estimating values of all relevant geometrical and electrical parameters of random NW networks required for using these networks as high performance transparent conductors.

3.1 Numerical method for conductivity calculation

Monte Carlo (MC) simulations are coupled with an efficient iterative algorithm implemented on the grid platform and used to investigate the conductivity of randomly distributed NWs networks [33, 99, 103]. We have considered the two-dimensional systems with isotropically placed NWs modeled as widthless sticks with a fixed length l_s. The centers of the NWs are randomly positioned and oriented inside the square system with size L_S. Two electrodes (i.e., conducting bars) are placed at the left and right sides. The top and bottom boundaries of the system are free and nonconducting, because free boundary conditions are more consistent with NW networks in practice. Two sticks (NWs) belong to the same cluster if they intersect. The system percolates (conduct) if the electrodes are connected with the same cluster. The behavior of the NW percolation is studied in terms of the normalized NW density $n = N/\mathcal{L}^2$, where N is the total number of NWs and $\mathcal{L} = L_S/l_s$ is the normalized system size. As determined in Chapter 2, the percolation threshold of the infinite-size stick system is defined by the critical density $n_c \approx 5.63726$. To evaluate the conductivity of the NW networks we introduce two different conductances:

(1) the conductance of the entire NW G_s; and

(2) the conductance due to the NW-to-NW junction G_j.

We assume diffusive electrical transport through the NW, which is typical for the rodlike nanostructures whose length is larger than the mean free path of the elec-

trons [104, 105]. According to the diffusive electrical transport the electrical conductance of a NW segment G_{seg} is inversely proportional to its length l_{seg} and can be calculated as follows

$$G_{\mathrm{seg}} = G_{\mathrm{s}} \frac{l_{\mathrm{s}}}{l_{\mathrm{seg}}}. \tag{3.1}$$

In our simulations, each NW-NW junction is modeled by an effective contact conductance regardless of the type of the junction, following the simplified approach of the authors of Refs. [15, 21, 33]. Therefore, if two NWs intersect a junction with the fixed conductance G_{j} is created at the intersection point. The created NW-NW junction conductance G_{j} connects two virtually created nodes positioned at the intersection point, as shown in Fig. 3.1. Each of these two nodes belongs to one of the two intersecting sticks, see Fig. 3.1. Therefore, the entire network of randomly distributed NWs is modeled by the electrical conductances of NW segments and NW-NW junctions created between the nodes positioned at the interaction points, see Fig. 3.1. As shown in Fig. 3.1, a node indexed by k can have maximum 2 neighboring nodes indexed by l_1 and l_2 belonging to the same NW as the node k (ith NW), as well as one neighboring node indexed by l_3 belonging to different NW (jth NW). The segment conductances G_{kl_1} and G_{kl_2} are determined from Eq. (3.1) where appropriate segment lengths are distances between the pairs of neighboring nodes (k, l_1) and (k, l_2), respectively.

Nodes that are positioned between the left and right electrodes of the system represent internal nodes of the electrical network. Each internal node k is associated with a electrical potential V_k, where $k = 1, 2, \ldots, N_{\mathrm{n}}$ and N_{n} is the total number of internal nodes. The electrical potentials of internal nodes are initially unknown and they should be calculated in order to determine the electrical conductivity of the network. However, when a NW intersects the left or right system electrode, an external node is created at the intersection point. If the NW intersects the left (right) electrode, the electrical potential of the created external node is set to 0 (V), according to a realistic assumption that the system electrodes are highly conductive and that the contact resistance between a NW and an electrode can be neglected [33]. Hence, the external nodes are the only nodes in the network that have known and fixed potentials (0 or V).

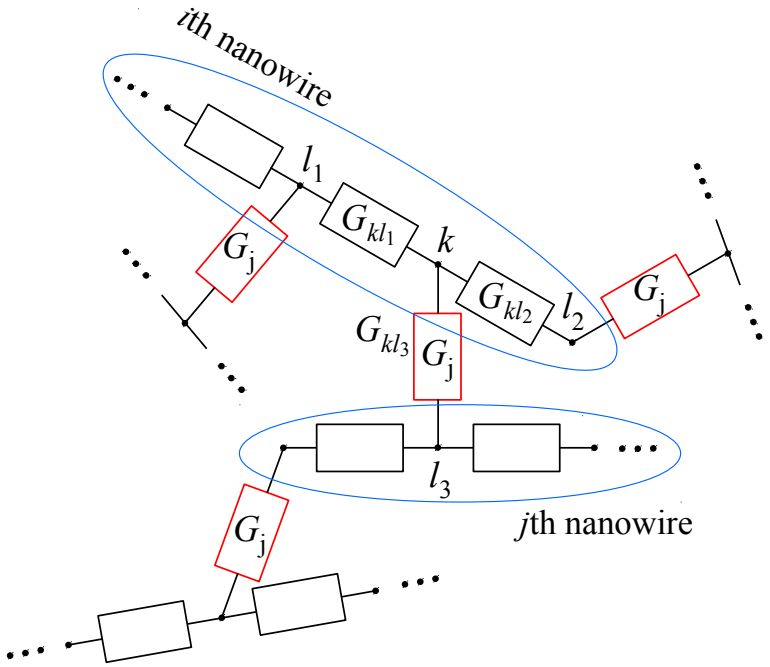

Figure 3.1: Schematic illustration of an electrical network of randomly distributed NWs where conductances of NW segments (black) and NW-NW junctions (red) are presented. A junction with the fixed conductance G_j is created at the intersection point between two virtually created nodes. Each of these two nodes belongs to one of two intersecting NWs. One node (k) can have maximum 3 neighboring nodes (l_1, l_2, and l_3), i.e., maximum 2 nodes belonging to the opposite sides of the same NW (l_1 and l_2 at ith NW) and 1 node belonging to different NW (l_3 at jth NW).

As shown in Fig. 3.1, an arbitrary internal node k can have maximum 3 internal neighboring nodes l_1, l_2, and l_3. Kirchhoff's current law is used to balance the current flow through the internal node k as follows

$$\sum_{l=l_1}^{l_3} G_{kl}\,(V_k - V_l) = I_k, \tag{3.2}$$

where G_{kl} is the conductance between the internal nodes k and l and I_k is the current flowing into the internal node k. If the internal node k has only internal nodes as its neighbors (maximum 3 of them), the current I_k is equal to 0. If the internal node k has an external node as one of its neighbors, the current I_k is different from 0. In that case, the current I_k flowing into the internal node k is $I_k = G_k(V_e - V_k)$, where G_k is conductance between the internal node k and its neighboring external node, if

such exists, given by Eq. (3.1), whereby the voltage V_e is equal to 0 or V depending on whether the external node is created at the left- or right-electrode intersection.

Kirchhoff's current law given by Eq. (3.2) and applied to all N_n internal nodes of the electrical network can be presented in the matrix form:

$$Gv = i, \tag{3.3}$$

where the square $N_n \times N_n$ matrix G represents a conductance matrix:

$$G = \begin{bmatrix} G_{11} & -G_{12} & \dots & -G_{1k} & \dots & -G_{1l} & \dots & -G_{1N_n} \\ -G_{21} & G_{22} & \dots & -G_{2k} & \dots & -G_{2l} & \dots & -G_{2N_n} \\ & & \vdots & & \vdots & & \vdots & \\ -G_{k1} & -G_{k2} & \dots & G_{kk} & \dots & -G_{kl} & \dots & -G_{kN_n} \\ & & \vdots & & \vdots & & \vdots & \\ -G_{l1} & -G_{l2} & \dots & -G_{lk} & \dots & G_{ll} & \dots & -G_{lN_n} \\ & & \vdots & & \vdots & & \vdots & \\ -G_{N_n1} & -G_{N_n2} & \dots & -G_{N_nk} & \dots & -G_{N_nl} & \dots & G_{N_nN_n} \end{bmatrix},$$

with the diagonal elements equal to

$$G_{kk} = \sum_{l=1,\, l\neq k}^{N_n} G_{kl} + G_k, \tag{3.4}$$

where G_k is the conductance between the internal node k and its neighboring external node, if such exists, otherwise $G_k = 0$. We note that a diagonal element G_{kk} of conductance matrix G presents sum of all conductances that have an internal node k as a common node, regardless of the type (internal or external) of their non-common nodes. Also, we note that a conductance between two non-neighboring nodes k and l is by default equal to 0 in the conductance matrix G. The column vector v presents an unknown vector of the electrical potentials of all internal nodes:

$$v = \begin{bmatrix} V_1 \\ V_2 \\ \vdots \\ V_k \\ \vdots \\ V_l \\ \vdots \\ V_{N_\mathrm{n}} \end{bmatrix},$$

whereas the column vector i presents a known vector which is determined by the electrical potential V applied to the right electrode, i.e., to the appropriate right-electrode external nodes:

$$i = V \begin{bmatrix} G_1 \\ G_2 \\ \vdots \\ G_k \\ \vdots \\ G_l \\ \vdots \\ G_{N_\mathrm{n}} \end{bmatrix},$$

where G_k is the conductance between the internal node k and its neighboring right-electrode external node, if such exists, otherwise $G_k = 0$.

The conductance matrix G is a square matrix with the total number of elements equal to the squared number of total internal nodes N_n^2. The total number of internal nodes is higher than 10^6 in the real systems. Therefore, the crucial significance for solving so large systems of linear equations given by Eq. (3.3) is the sparseness of their matrices G, which have maximum 4 non-zero elements in each raw (maximum 3 non-zero neighboring conductances + one diagonal element). Also, we note that the system matrix G is symmetric $G = G^\mathrm{T}$, because $G_{kl} = G_{lk}$, as well as positive-definite, because $G_{kk} > 0$ and $G_{kk} \geq \sum_{l \neq k} |G_{lk}|$ for all k and its total sum is positive $\sum_{k,l} G_{k,l} > 0$, see Ref. [106].

Since the system matrix G is sparse, square, symmetric, and positive-definite an iterative equation solver (i.e., conjugate gradient method (CGM) with Jacobi preconditioner) has been employed to solve the large system of linear equations as explained in detail in Appendix D. In order to improve the simulation efficiency, the following optimizations have been performed before the iterative equation solver is employed to solve the system:

i) During the determination of the NW connectivities, each NW is first registered into a subcell in which its center lies, as described in section 2.1. As it was explained there, it is only necessary to check the connectivity between a chosen NW and any of those NWs belonging to the same subcell or the neighboring subcells.

ii) Before applying Kirchhoff's current law to the internal nodes, it should be checked does the analyzed NW network percolate. If the NW network does not percolate its conductivity is equal to 0 and, therefore, there is no need for solving Kirchhoff's current law equations.

iii) If the NW network percolates, all dangling NWs, with the corresponding junctions, that do not carry any current should be deleted before the iterative solver is applied, see Ref. [33].

iv) In order to reduce the total number of iterations, starting values for the electrical potentials V_k^0 should be proportional to their distances x_k from the left electrode, i.e., $V_k^0 = \frac{x_k}{\mathcal{L}} V$, because this starting values present a good estimate of the final potentials V_k, see Ref. [107].

After solving this large system of linear equations and obtaining the potentials of all internal nodes, the total current I is easily determined as the sum of the currents flowing into (out of) all external nodes connecting the left (right) electrode. After obtaining the total current I under an applied voltage between the electrodes V the macroscopic electrical conductivity[1] of the system is evaluated as $\sigma = I/V$. Monte Carlo simulations have been performed for a wide range (i.e., $G_j/G_s = 0.001$ to

[1]For a rectangular system of size $L \times W$, where L is the distance between the electrodes and W is their length, the relation between the system conductance G and conductivity σ is according to Ohm's law given by $G = \sigma W/L$. In this Chapter the system is the square-shaped $L = W$, which implies $G = \sigma$. Although in the square system conductance is equal to the system conductivity, in this Chapter for clarity we have assumed terminology in which the *conductance* is used for denoting a single conductive element (NW or junction) while the *conductivity* is related to the entire system.

1000) of junction-to-NW conductance ratios[1]. Finally, for each set of the system parameters, the electrical conductivity is averaged over the N_{MC} independent MC realizations. To obtain the same precision for the finite-size systems $N_{\mathrm{MC}} = 64000$ realizations are used for the systems with normalized size $\mathcal{L} = 10$ down to $N_{\mathrm{MC}} = 4000$ for the largest system $\mathcal{L} = 40$ studied. Using the appropriate functions for the fitting data and the least-squares fitting methodology [4], good fits with high correlation factors ($R^2 > 0.998$) were obtained for all analyzed systems.

As one can see in Fig. 3.2, the algorithm running time needed for conductivity calculation using CGM with Jacobi preconditioner for a single MC realization of a random NW network depends on the square of normalized NW density, i.e., on the total number of internal nodes, by a power law with the exponent equal to a value of 3/2, i.e., ($T \sim (n^2)^{3/2} \sim N_{\mathrm{n}}^{3/2}$), when the NW density is $n > 10$. The power-law dependency of the running time with the exponent 3/2 for CGM is explained in detail in Appendix D. We note that for higher NW densities n almost all junctions and NWs will be involved in the current flow through the system, as shown in Fig. 3.4. Therefore, for the normalized NW density higher than 10, i.e., $n > 10$, the number of internal nodes involved in the current flow increases with the NW density by a square power law $N_{\mathrm{n}} \sim n^2$ and for this reason, we obtain the power-law dependency $T \sim (n^2)^{3/2}$ shown in Fig. 3.2. For lower NW densities the number of internal nodes N_{n} involved in the current flow increases rapidly with increasing NW density n, see Fig. 3.4, and, hence, the running time also increases rapidly with increasing n^2, see Fig. 3.2 for $n < 10$.

[1] The choice of an extended range of conductance ratios is based on the experimental measurements on crossed NWs [108], as well as other rodlike nanoparticles, such as CNTs [109, 110]. For crossed single-walled CNTs the junction conductance is of the order of magnitude $0.1e^2/h$ [109] (where e is the electron charge, h is Planck's constant, and $e^2/h \approx 39$ μS) and two orders of magnitude higher for NW-NW junctions [21, 22, 111]. In the diffusive case, typical for NWs and CNTs whose length l_{s} is larger than the mean free path of electrons λ, the conductance can be approximated by $G_{\mathrm{s}} \approx (4e^2/h)(\lambda/l_{\mathrm{s}})$ [104, 105, 112]. For single-walled CNTs the mean free path of the electrons is of the order $\lambda \approx 1$ μm [105, 112], while for NWs, the mean free path is considerably shorter ≈ 40 nm [113], implying that the diffusive conduction model is applicable even for very short NWs. Therefore, the junction-to-stick conductance ratio $G_{\mathrm{j}}/G_{\mathrm{s}}$ depends on the total stick length l_{s}. When the stick length is of the order of the mean free path of the electrons the conductance ratio, especially for CNTs, is $G_{\mathrm{j}}/G_{\mathrm{s}} = 0.001 - 0.1$. On the other hand, for very long sticks (i.e., $l_{\mathrm{s}} > 100\lambda$), the conductance ratio, especially for NWs, becomes higher than 1, $G_{\mathrm{j}}/G_{\mathrm{s}} > 1$.

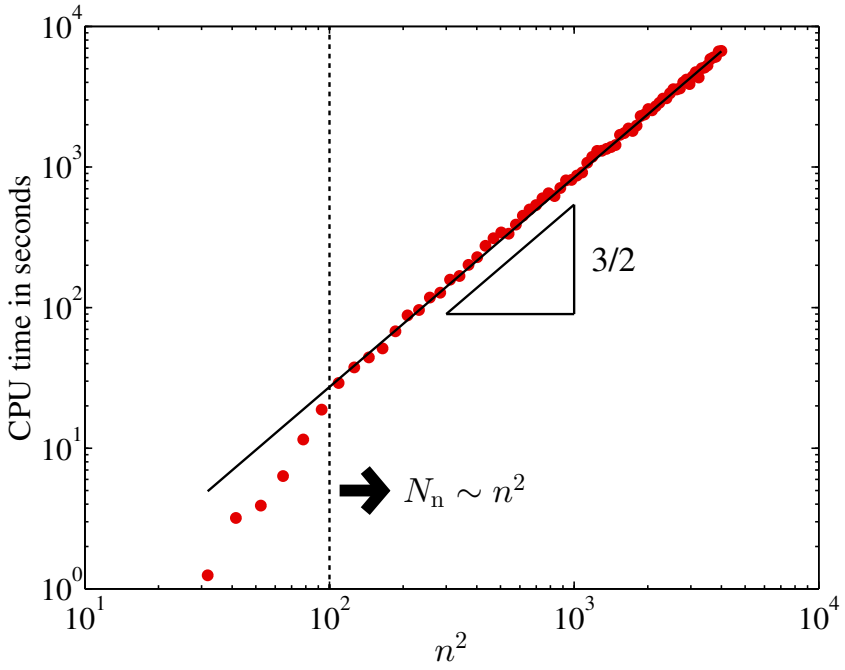

Figure 3.2: The dependence of the average CPU time T needed for conductivity calculation using CGM with Jacobi preconditioner on the square of normalized density n^2 for a single MC realization of a random NW network with the normalized size $\mathcal{L} = 20$ and junction-to-NW conductance ratio $G_j/G_s = 1000$. The results are shown on a logarithmic scale to demonstrate power-low dependence of the running time. The simulations were run on a computer cluster configured with Intel Xeon CPUs with 2.33 GHz and 8 GB RAM. The solid line $T \sim (n^2)^{3/2}$ is only a guide for the eye. As one can see, the running time depends on the total number of internal nodes by a power law with the exponent equal to a value of 3/2, i.e., $(T \sim (n^2)^{3/2} \sim N_n^{3/2})$, when the normalized NW density is $n > 10$.

3.2 Local conductivity exponent

As already mentioned, the numerical estimates of the conductivity exponent t are based on the linear fit of the MC results for the logarithms of the conductivity σ and density $n - n_c$ [27, 31–33]. The estimates therefore rely on the assumption that σ obeys the simple power-law dependence over a quite extended density range. As there exists no justification of such an assumption, we have investigated in detail the behavior of the conductivity σ as we move away from the critical point. A local

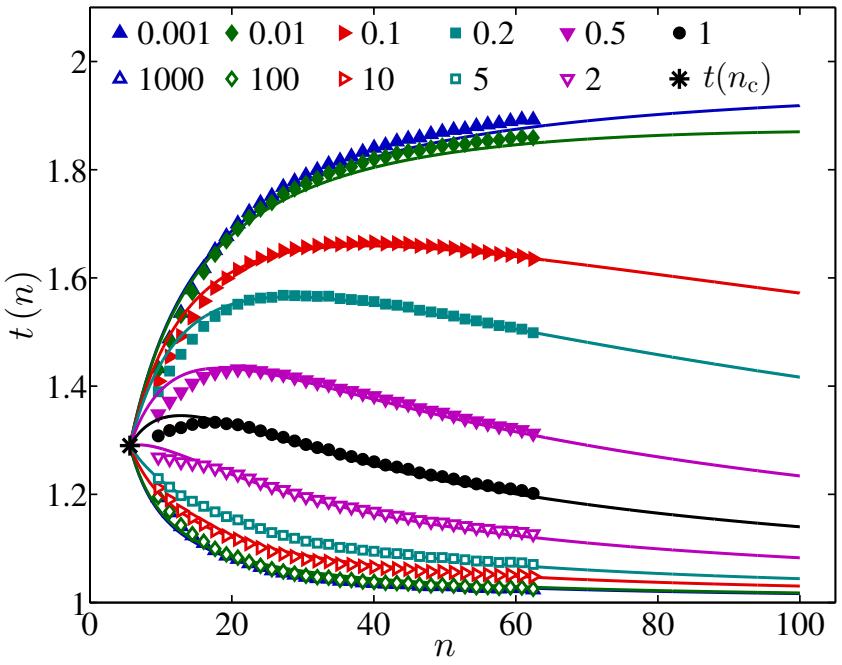

Figure 3.3: The dependence of the local conductivity exponent $t(n)$ on the normalized NW density n and junction-to-NW conductance ratio G_j/G_s. The points are MC simulation results obtained using Eq. (3.5) for the normalized system size $\mathcal{L} = 20$. The values are given for the conductance ratios $G_j/G_s = 0.001, 0.01, 0.1, 0.2, 0.5, 1$ (filled), and their inverse values $1000, 100, 10, 5, 2$ (transparent). The error bars are smaller than the size of the points. The star marker denotes the expected universal value for the conductivity exponent at the percolation threshold $t(n_c)$. The lines represent the local conductivity exponents $t(n)$ obtained from the conductivity model for an infinite-size system, Eq. (3.7).

(density dependent) conductivity exponent is defined as $t(n)$ by [97, 114]

$$t(n) = \frac{n - n_c}{\sigma} \frac{d\sigma}{dn}. \tag{3.5}$$

The dependence of the local conductivity exponent $t(n)$ on the NW density n and the ratio of the NW-NW junction conductance (G_j) to NW conductance (G_s) (i.e., G_j/G_s) is shown in Fig. 3.3. As one can see from a coarse observation, when the NW density approaches the percolation threshold n_c from above the local conductivity exponent converges to the universal value for 2D systems $t(n_c) \approx 1.29$ for all G_j/G_s values. The fine behavior of the local conductivity exponent for finite-size systems in the vicinity of the percolation threshold will be discussed later in this Chapter.

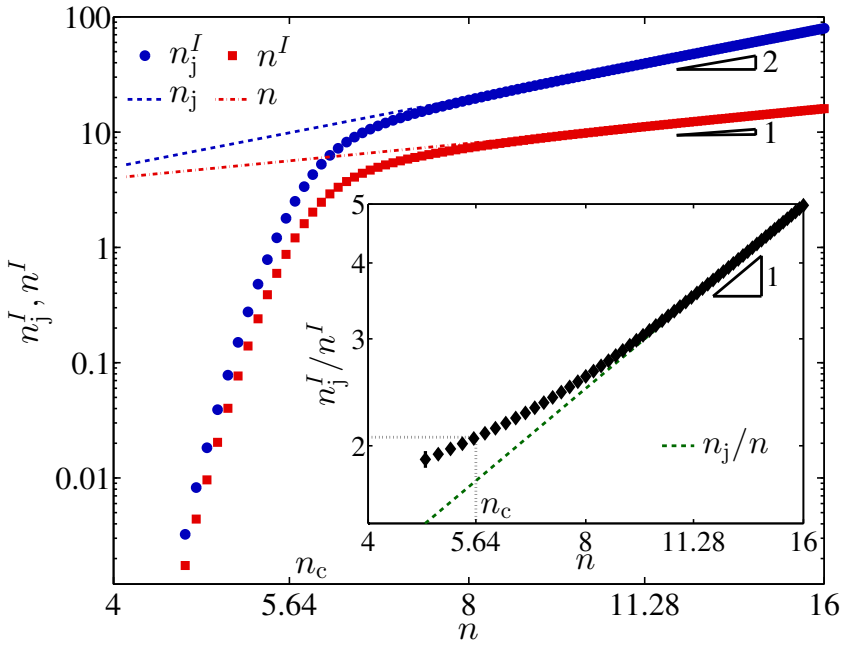

Figure 3.4: The normalized density of junctions n_j^I and NWs n^I involved in the current flow through the system is compared with the density of all junctions n_j and NWs n in the system of normalized size $\mathcal{L} = 20$. For higher NW densities n almost all junctions and NWs will carry some current. The error bars are smaller than the size of the points. Inset: The density ratio of the current-carrying junctions to current-carrying NWs n_j^I/n^I is higher than the density ratio of all junctions to all NWs n_j/n in the system. At the percolation threshold this ratio is about 2, i.e., $n_j^I/n^I = 2.0(1)$.

With the increasing concentration n, the local conductivity exponents $t(n)$ change quickly from the universal value $t(n_c)$, taking the values in a wide range $1 \leq t(n) \leq 2$. From Fig. 3.3, one can see that the local conductivity exponents $t(n)$ for the conductance ratio higher than 2 ($G_j/G_s > 2$) is a monotonically decreasing function of the NW density n which converges to 1 from above. Somewhat surprisingly, for the conductance ratios lower than 1 (i.e., $G_j/G_s < 1$), the local exponent $t(n)$ is not a monotonic function and has a local maximum. The observed density where the local conductivity exponent reaches a maximum decreases with increasing the conductance ratio G_j/G_s.

To explain the observed behavior of the exponent $t(n)$ at the higher densities $n > 2n_c$, one needs to look into the structure of the dense conducting NW networks. Figure 3.4 shows the normalized densities of the NWs n^I and junctions n_j^I that

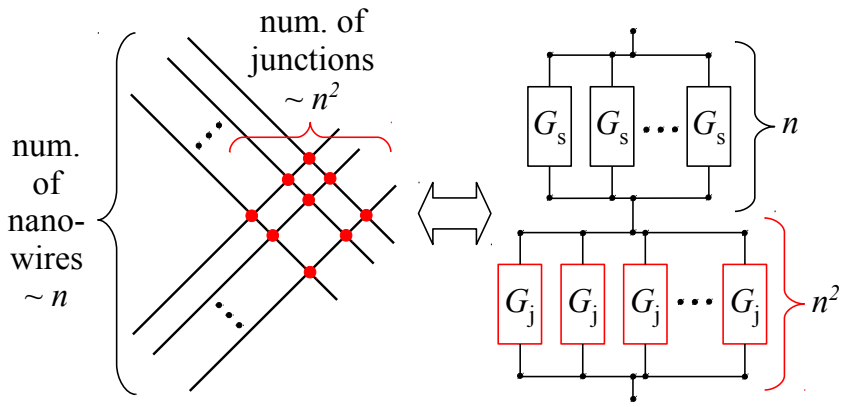

Figure 3.5: Schematic illustration of simplified model of random NW network where the total number of junction is proportional to the square of normalized NW density n^2 (left panel). The equivalent conductance of the simplified network presented as serial conductance n NWs in parallel and n^2 junctions in parallel (right panel).

carry the current through the system. For sufficiently high NW densities ($n > 2n_c$), one can see that almost all the NWs and junctions in the system contribute to the conductivity and that the density of the current-carrying junctions increases with the NW density n by a square power law $n_j^I \sim n^2$. The reason for this is that the mean number of contacts per NW is proportional to the NW density, see Ref. [115]. Also, for a sufficiently high NW density n the current-carrying NW density n^I is proportional to n.

As illustrated in Fig. 3.5, when the NW density n is well above the percolation threshold n_c, the conductivity of the system can be modeled as an equivalent serial conductance n NWs in parallel and n^2 junctions in parallel

$$\sigma \sim \frac{1}{bn^{-1}/G_s + n^{-2}/G_j}, \tag{3.6}$$

where b is a constant parameter. One can see that the square term n^{-2}/G_j, originating from the junctions, converges faster to zero than the linear term bn^{-1}/G_s. This explains the conductivity exponent $t(n)$ approaching to 1 when the NW density is sufficiently high (i.e., $n \gg G_s/G_j$) and the existence of the local exponent maximum in Fig. 3.3. If the NWs are much more conductive than the junctions (e.g., $G_j/G_s = 0.01$) the density where the local conductivity exponent starts to converge to 1 is high and computationally unreachable in the MC simulations shown

in Fig. 3.3. Only in the limiting case when the NWs are superconductive and the conductance ratio approaches zero (i.e., $G_j/G_s \to 0$) should the conductivity exponent $t(n)$ converge to 2 with the increasing density n, which is consistent with Keblinski *et al.* [31]. In the other limit, when the junctions are superconductive (i.e., $G_j/G_s \to \infty$) the local conductivity exponent $t(n)$ should have the fastest convergence to 1.

At the densities close to the percolation threshold n_c, only a fraction but not all the NWs and junctions in the system contribute to the conductivity, by carrying some current. From Fig. 3.4 (inset), one can see that at the percolation threshold n_c, the density of the current-carrying junctions is about two times higher than the density of the current-carrying NWs, i.e., $n_j^I/n^I = 2.0(1)$. From the framework of the percolation theory we cannot determine a density-dependent factor of proportionality in the conductivity power law $\sigma \sim (n - n_c)^t$. Instead, we fit the factor of proportionality with an expression for the dense systems, i.e., with Eq. (3.6), and obtain $1/\left[bn^{t-1}/G_s + (n + n_c)^{t-2}/G_j\right]$. This relation explicitly includes the previous observation that there is almost exactly two times more current-carrying junctions than current-carrying NWs at the percolation threshold. For a general conductivity description of the infinite-size systems we obtain

$$\sigma = a\frac{(n - n_c)^t}{bn^{t-1}/G_s + (n + n_c)^{t-2}/G_j}, \tag{3.7}$$

where $a = 0.027(1)$ and $b = 0.061(3)$ are fitting parameters calculated using the least-squares fitting methods. The solid lines in Fig. 3.3 denote the local conductivity exponents $t(n)$ calculated from Eq. (3.5), using the model for an infinite system given by Eq. (3.7), for a wide range of conductance ratios $G_j/G_s = 0.001$ to 1000. Deviations between the modeled and MC values for local conductivity exponent $t(n)$ are comparable to the statistical errors.

3.3 Finite-size model for conductivity

Figure 3.6 illustrates the structure of the percolating cluster [Figs. 3.6(a) and 3.6(b)] and the redistribution of the current in the dense NW networks due to the junction-

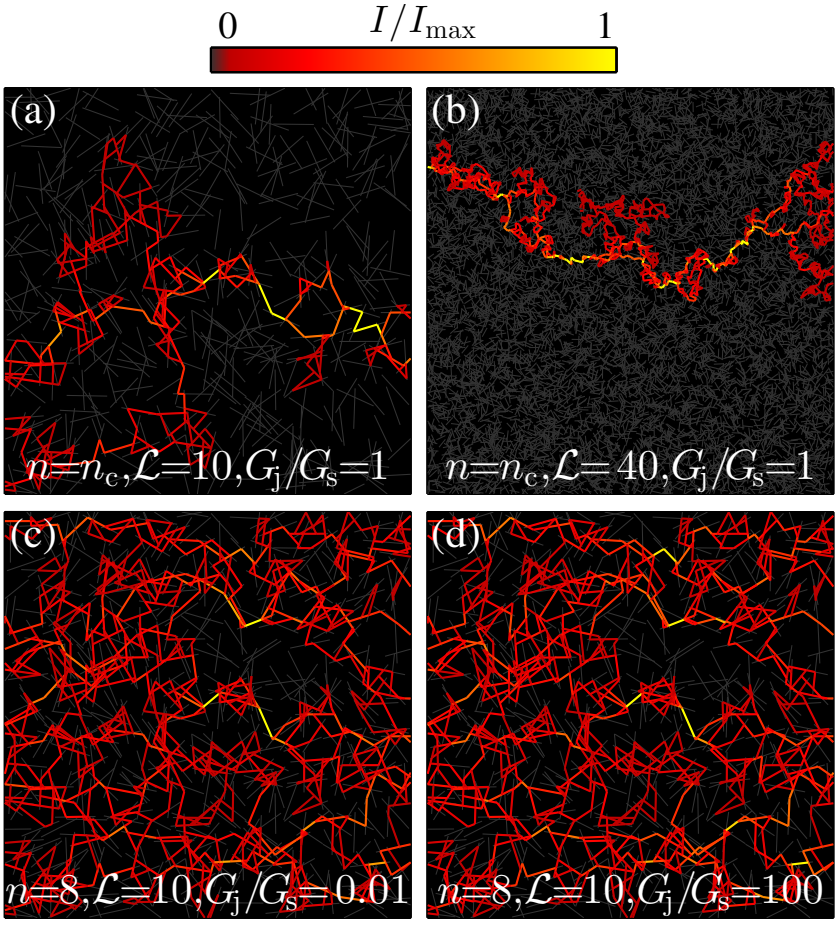

Figure 3.6: Simulated current (a) and (b) at different system sizes and (c) and (d) junction-to-NW conductance ratios. The current through a NW I is given relative to the maximal current in the system $I_{\max}$. There is a large difference in the fraction of the system involved in the current flow between the two nominally identical films in term of density ($n = n_c$) and junction-to-NW conductance ratio ($G_j/G_s = 1$) for two different system sizes $\mathcal{L} = 10$ and 40. The current redistribution with the increasing junction-to-NW conductance ratio G_j/G_s is visible from (c) and (d). (c) If junctions are weakly conductive (i.e., $G_j/G_s = 0.01$) the maximal current flows along the shortest path with the least junctions. (d) For high junction conductance values (i.e. $G_j/G_s = 100$), the total current is evenly carried by the larger number of shortest paths connecting electrodes. This effect is only visible at higher densities (e.g., $n = 8$) where several paths connecting electrodes exist.

to-NW conductance ratio increase [Figs. 3.6(c) and 3.6(d)]. The current through a NW I is given relative to the maximal current in the system $I_{\max}$. As one can see from Figs. 3.6(a) and 3.6(b), the percolating cluster consists of a few sub-clusters connected by high current links. This explains why on average more junctions than

NWs are needed to shortcut the electrodes. For a large, but finite-size systems at the percolation threshold, the density of the current-carrying junctions decreases with normalized system size $\mathcal{L}$ as $n_{\mathrm{j}}^{I} \sim \mathcal{L}^{-\beta/\nu}$, where $\beta = 5/36$ for 2D systems [2]. Also, the density of the current-carrying NWs at the percolation threshold is $n^{I} \sim \mathcal{L}^{-\beta/\nu}$. As a result the densities of the current-carrying NWs and junctions decrease with normalized system size, see Figs. 3.6(a) ($\mathcal{L} = 10$) and 3.6(b) ($\mathcal{L} = 40$). Furthermore, the density ratio n_{j}^{I}/n^{I} at the percolation threshold converges to a constant value with the increase of the normalized system size, see Fig. 3.4. At higher NW densities (i.e., $n = 8$) one can see that current flows along many parallel paths connecting electrodes. An increase of the junction-to-NW conductance ratio $G_{\mathrm{j}}/G_{\mathrm{s}}$ results in the more uniform redistribution of the current, see Figs. 3.6(c) ($G_{\mathrm{j}}/G_{\mathrm{s}} = 0.01$) and 3.6(d) ($G_{\mathrm{j}}/G_{\mathrm{s}} = 100$). For weakly conductive junctions (i.e., low conductance ratio $G_{\mathrm{j}}/G_{\mathrm{s}} = 0.01$), most of the current flows through a shortest path with the least junctions along. With the increase of the junction conductance several parallel paths become visible. As a result, the total current through the system is more evenly distributed, resulting in the higher conductivity. This is also expected from Eq. (3.7).

If we compare the infinite system model prediction and MC simulation results in Fig. 3.3 close to the percolation threshold, we observe a deviation between the predicted and simulated values. This deviation is a result of the finite-size effects, since the MC results in Fig. 3.3 are calculated for the large but finite-size system (i.e., $\mathcal{L} = 20$). The convergence of the local conductivity exponents with increasing system size is shown in Fig. 3.7. The points are MC simulation results for the systems with sizes $\mathcal{L} = 10, 20$, and 40 and the solid line denotes the model for an infinite system given by Eq. (3.7). For the finite-size systems close to the percolation threshold we observe a large deviation of the local conductivity exponent $t(n)$ from the model. The local conductivity exponent decreases with the decreasing system size and can be even lower then 1, i.e., $t(n) < 1$. This is result of a nonzero conductivity value for the finite-size systems at the percolation threshold [2]. Therefore, the model should be adapted for the finite-size systems. The finite-size scaling arguments [2, 4, 116]

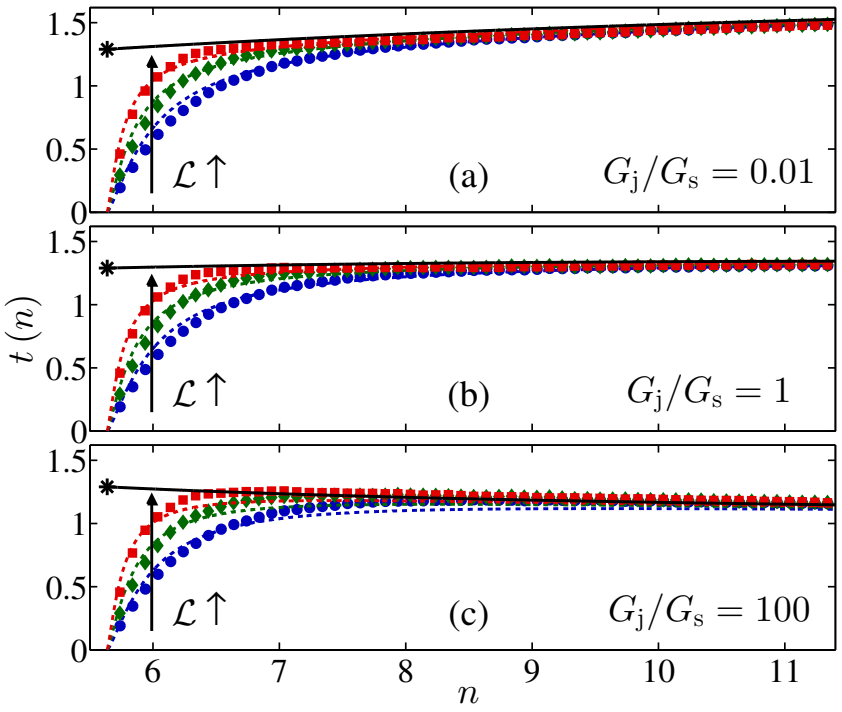

Figure 3.7: The local conductivity exponents $t(n)$ for the NW networks with increasing normalized system size $\mathcal{L} = 10, 20$, and 40 and for three conductance ratio values (a) $G_j/G_s = 0.01$, (b) 1, and (c) 100. The direction of the increase of $\mathcal{L}$ is indicated on the graphs. The points are obtained from the MC simulations and calculated using Eq. (3.5). The error bars are smaller than the size of the points. The solid line represents the local conductivity exponent $t(n)$ for the infinite system obtained from Eq. (3.7), while the dashed lines denote the local conductivity exponents $t(n)$ obtained from the model that includes finite-size effects, Eq. (3.11). The star marker denotes the expected value for the conductivity exponent of the infinite system at the percolation threshold n_c.

suggest that the conductivity σ depends on the system size $\mathcal{L}$ as

$$\sigma \sim (n - n_c)^t f\left[\frac{\xi(n)}{\mathcal{L}}\right], \tag{3.8}$$

where $\xi(n) \sim |n - n_c|^{-\nu}$ is the correlation length that measures the linear extent of the largest cluster and $f\,[\xi(n)/\mathcal{L}]$ is the conductivity finite-size scaling function. For 2D systems the correlation-length exponent is $\nu = 4/3$, see Ref. [2].

In order to demonstrate the generality of the conductivity finite-size scaling function $f\,[\xi(n)/\mathcal{L}]$, the dependence of the normalized conductivity $\sigma/(n - n_c)^t$, which is proportional to $f\,[\xi(n)/\mathcal{L}]$, on the normalized correlation length $(n - n_c)^{-\nu}/\mathcal{L}$ is

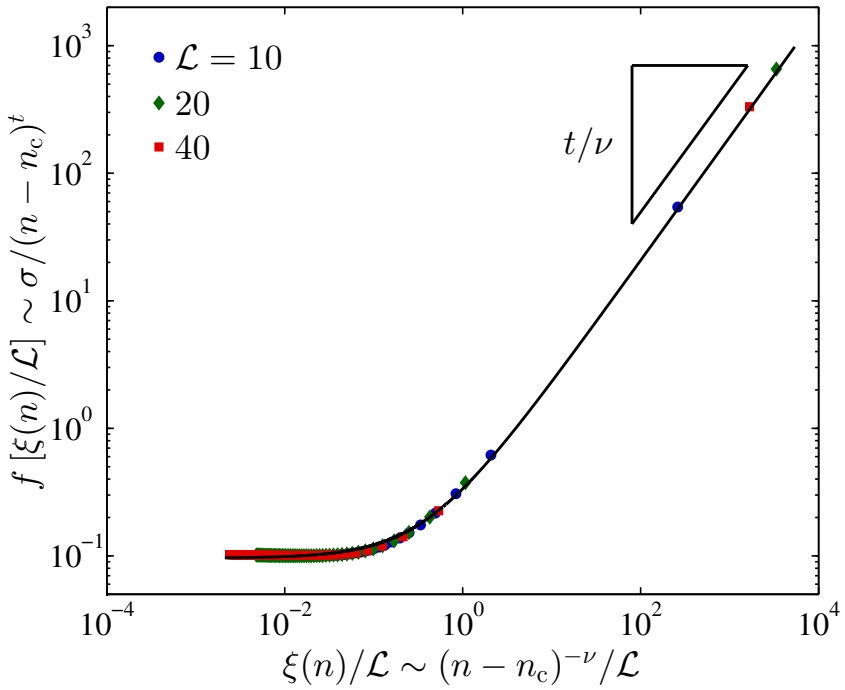

Figure 3.8: The dependence of the conductivity finite-size scaling function $f\,[\xi(n)/\mathcal{L}]$, which is according to Eq. (3.8) estimated as $\sigma/(n-n_c)^t$, on the normalized correlation length $\xi(n)/\mathcal{L} \sim (n-n_c)^{-\nu}/\mathcal{L}$. The dependence is shown for three NW systems with increasing size $\mathcal{L} = 10, 20$, and 40. The points are obtained from the MC simulations. The solid line represents the finite-size scaling function $f\,[\xi(n)/\mathcal{L}]$ calculated from Eq. (3.9).

shown in Fig. 3.8 for different system sizes. As shown in Fig. 3.8, all the points obtained using MC simulations for different system sizes collapse to a common curve. The collapse of all the calculated data to the same curve, independently of the system size, shows the generalized behavior of the conductivity finite-size scaling function $f\,[\xi(n)/\mathcal{L}]$ for random stick networks.

In order to include the finite-size scaling effects into the comprehensive conductivity model, two limiting behaviors are observed:

(1) the infinite system above the percolation threshold; and

(2) the finite-size systems at the percolation threshold.

For the infinite system above the percolation threshold, i.e., $\xi(n)/\mathcal{L} \to 0$, the conductivity follows the simple scaling law and finite-size scaling function $f\,[\xi(n)/\mathcal{L}]$ converges to a constant value, see Fig 3.8. In the other limit, for the finite-size systems at the percolation threshold, i.e. $\xi(n)/\mathcal{L} \to \infty$, conductivity has a nonzero

value $\sigma \sim \mathcal{L}^{-t/\nu}$, see Ref. [2]. Therefore, in that case the finite-size scaling function should have a form $f\left[\xi(n)/\mathcal{L}\right] \sim \left[\xi(n)/\mathcal{L}\right]^{t/\nu}$ to cancel the conductivity dependence on density in Eq. (3.8). This limiting behavior of the conductivity scaling function $f\left[\xi(n)/\mathcal{L}\right]$ is demonstrated in Fig 3.8 as its linear increase with slope t/ν in logarithmic scale when $\xi(n)/\mathcal{L} \to \infty$. Since the finite-size scaling function $f\left[\xi(n)/\mathcal{L}\right]$ above the percolation threshold is a continuous and smooth function (see Fig. 3.8), we approximate it by a combination of its two limiting behaviors

$$f\left[\frac{\xi(n)}{\mathcal{L}}\right] \sim 1 + c\left[\frac{(n-n_c)^{-\nu}}{\mathcal{L}}\right]^{t/\nu}, \tag{3.9}$$

where c is the finite-size parameter. As shown in Fig. 3.8, this approximation represents an excellent fit to the data obtained using numerical simulations when the parameter c is equal to 2.5. Inserting Eq. (3.9) into Eq. (3.8) the first-order approximation of the finite-size scaling law for conductivity becomes

$$\sigma \sim (n-n_c)^t + c\mathcal{L}^{-t/\nu}. \tag{3.10}$$

Finally, incorporating the finite-size effects given by Eq. (3.10) into the conductivity model for an infinite-size system, Eq. (3.7), we obtain the finite-size model for conductivity

$$\sigma = a\frac{(n-n_c)^t + c\mathcal{L}^{-t/\nu}}{bn^{t-1}/G_s + (n+n_c)^{t-2}/G_j}. \tag{3.11}$$

The finite-size parameter for 2D NW networks $c = 2.5(1)$ is calculated using the least-squares fitting methods. A comparison between the MC results and the values obtained from the model given by Eq. (3.11) is shown in Fig. 3.7. The dashed lines in Fig. 3.7 denote the local conductivity exponents $t(n)$ calculated from the model including finite-size effects, Eq. (3.11), for systems with increasing normalized size $\mathcal{L} = 10$, 20, and 40 and for three conductance ratio values $G_j/G_s = 0.01$, 1, and 100. We see that the introduction of finite-size effects in the model significantly improves the quantitative description of the system close to the percolation threshold.

Finally, the MC conductivity values normalized with the NW conductance G_s and fitted by Eq. (3.11) for the systems of normalized size $\mathcal{L} = 20$ and conductance

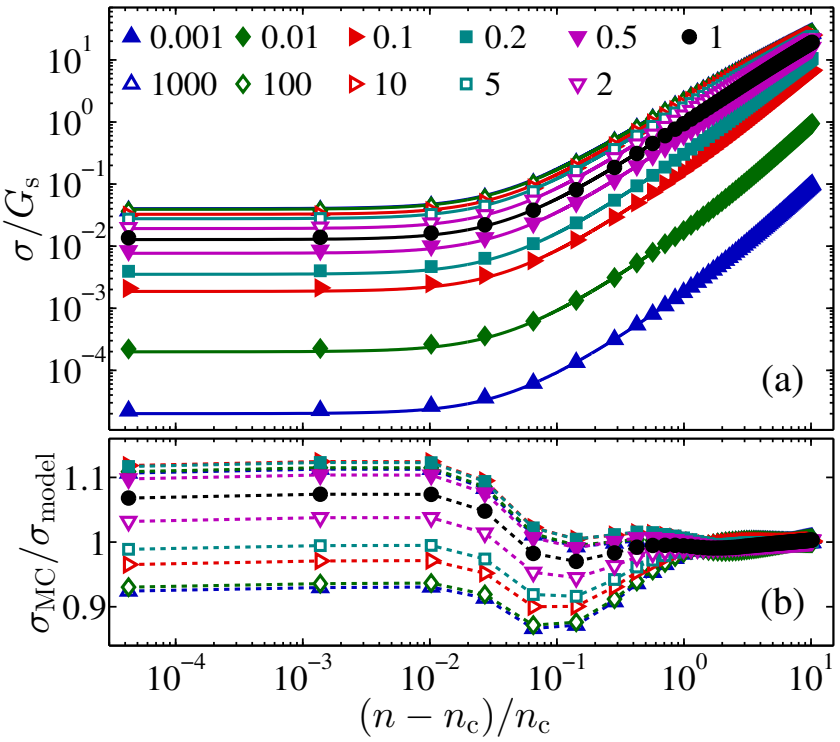

Figure 3.9: (a) Conductivity as a function of $(n - n_c)/n_c$ is obtained from the MC simulations (points) for the NW network of normalized size $\mathcal{L} = 20$ and the junction-to-NW conductance ratio from $G_j/G_s = 0.001$ to 1000 (from bottom to top). The lines denote values obtained from the conductivity model for the finite-size systems given by Eq. (3.11). (b) The conductivity ratio between the MC simulation results σ_{MC} and the values obtained from the model σ_{model} for corresponding finite-size systems, Eq. (3.11). The error bars are smaller than the size of the points.

ratios from $G_j/G_s = 0.001$ to 1000 are shown in Fig. 3.9(a). For all studied values of the conductance ratio G_j/G_s the conductivity obtained from the model agrees with the MC results over the whole range of the NW density n, see Fig. 3.9(a). The agreement between the MC results and the model is good for higher NW densities ($n > 2n_c$) (i.e., further away from the percolation threshold), but not so good in the vicinity of the percolation threshold, see Fig. 3.9(b). Hence, in the vicinity of the percolation threshold the conductivity ratio between the MC simulation results and the values obtained from the model is shown in Fig. 3.10 for different system sizes $\mathcal{L} = 10$, 20, and 40. For all three system sizes in Fig. 3.10 the curves look qualitatively similar. Only the density where the dense-system behavior becomes dominant decreases with the normalized system size $\mathcal{L}$. To improve the agreement

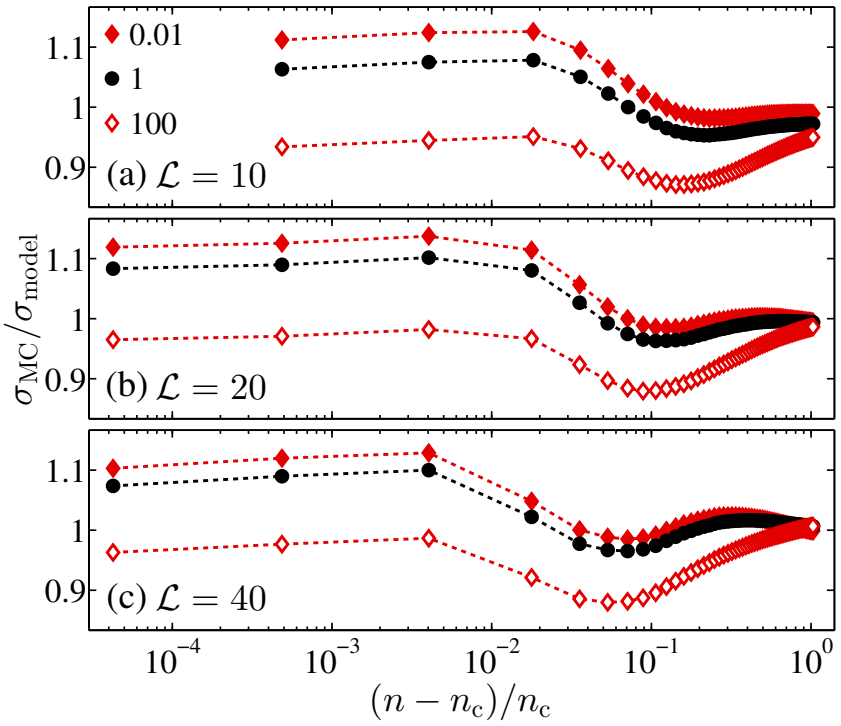

Figure 3.10: The conductivity ratio between the MC simulation results σ_{MC} and the values obtained from the model σ_{model} given by Eq. (3.11) for different system sizes (a) $\mathcal{L} = 10$, (b) 20, and (c) 40 and for three conductance ratio values $G_{\mathrm{j}}/G_{\mathrm{s}} = 0.01$, 1, and 100. The error bars are smaller than the size of the points.

between the MC results and the model close to the percolation threshold one could consider a further refinement of the model to include higher order correction for the finite-size effect. Finally, the proposed model for conductivity gives a good estimate of the local conductivity exponents, as one can see in Figs. 3.3 and 3.7.

3.4 Random nanowire networks as transparent conductors

The networks of randomly distributed metallic NWs are promising candidates to replace expensive indium tin oxide as the transparent conducting electrode material in the next generation devices [14, 21–23, 111]. Two critical performance criteria for the transparent conductors are their optical transmittance T and electrical conductivity σ [21]. Many studies [13, 21–23] have confirmed a trade-off between high optical transmittance T and high electrical conductivity σ. These quantities are both well measurable and depend on a variety of independent structural parameters

including the density of NWs, their length, and diameter.

The relationship between the optical transmittance T and the normalized density n appears to be linear for the NWs with high length-to-diameter aspect ratio and can be described by a simple model based on the fractional area coverage of the NWs, see Refs. [13, 21, 23]. As proposed in Refs. [13, 21, 23], the fractional area coverage of the NWs in a thin-film network can be simply approximated by

$$A_{\mathrm{c}} = \frac{N l_{\mathrm{s}} d_{\mathrm{s}}}{L_{\mathrm{S}}^2}, \tag{3.12}$$

where d_{s} is the diameter of the NWs [13, 21, 23]. The optical transmittance of the random NW network, using its fractional area coverage quantified by Eq. (3.12), can be approximated by

$$T = 1 - A_{\mathrm{c}} = 1 - \frac{N l_{\mathrm{s}} d_{\mathrm{s}}}{L_{\mathrm{S}}^2} \tag{3.13}$$

and according to our definition of the normalized NW density $n = N l_{\mathrm{s}}^2 / L_{\mathrm{s}}^2$, the previous expression can be simplified as

$$T = 1 - \frac{n}{r_{\mathrm{s}}}, \tag{3.14}$$

where $r_{\mathrm{s}} = l_{\mathrm{s}}/d_{\mathrm{s}}$ is the length-to-diameter aspect ratio of NWs.

We remind that the general conductivity model for random NW networks given by Eq. (3.11) is developed modeling NWs as widthless-sticks with infinite aspect ratio ($r_{\mathrm{s}} \to \infty$). Without losing of generality, that conductivity model can also be used for networks of randomly distributed NWs with finite but still high aspect ratio ($r_{\mathrm{s}} \gg 1$). Therefore, incorporating the conductivity model given by Eq. (3.11) into the analytical approximation for the density-dependent optical transmittance given by Eq. (3.14), we obtain a dependence of the optical transmittance T on the network conductivity σ shown in Fig. 3.11. The expected trade-off between the optical transmittance T and the electrical conductivity σ is clearly demonstrated in Fig. 3.11, because high values of σ correspond to a high normalized density n with low T, while lower values of σ correspond to a lower normalized density n with high T. Therefore, an intermediate normalized density n is needed to produce

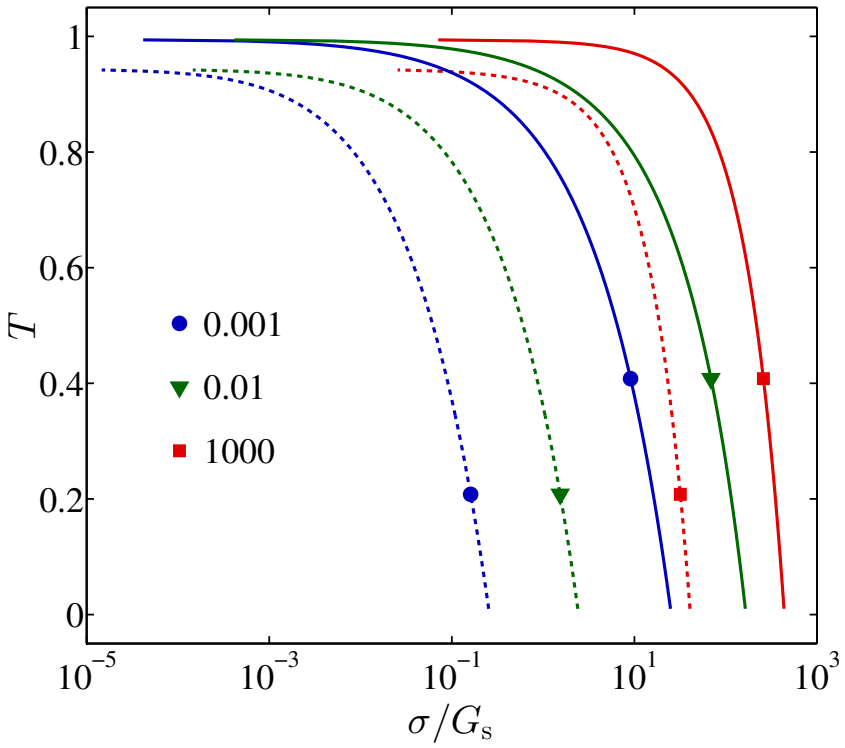

Figure 3.11: Optical transmittance T of a random NW network as a function of the network conductivity σ is obtained by incorporating the conductivity model given by Eq. (3.11) into the density-dependent optical transmittance given by Eq. (3.14) for the system with normalized size $\mathcal{L} = 20$ and three conductance ratio values $G_j/G_s = 0.001$, 0.01, and 1000. The dashed lines represent the optical transmittance T for randomly distributed NWs with length-to-diameter aspect ratio $r_s = 100$, while solid lines denote the optical transmittance for NWs with aspect ratio $r_s = 1000$.

random NW transparent conductors that achieve both acceptable values of T and σ. Also, we note that increase of length-to-diameter aspect ratio r_s and junction-to-NW conductance ratio G_j/G_s is generally advantageous for increasing T at a fixed σ/G_s, see Fig. 3.11.

Acceptable values of the optical transmittance T and the electrical conductivity σ for the most of practical applications are $T > 0.9$ and $\sigma > 0.1$ S, because transmittance lower than 0.9 and conductivity lower than 0.1 S result in significant power losses, see Refs. [12, 13, 21, 23]. From the transmittance constraint $T > 0.9$ and the requirement for achieving a percolation through the network, we obtain that the normalized density of NWs should belong to the range determined by $n_c < n < r_s/10$, see Eq. (3.14). This condition is satisfied only when $n_c < r_s/10$, i.e., when the

length-to-diameter aspect ratio of NWs is $r_s > 10n_c$, which is roughly $r_s > 100$. Finally, practically acceptable values of junction-to-NW conductance ratio G_j/G_s can be determined applying the conductivity constraint to the expression obtained from Eq. (3.11) at the high-bound density $r_s/10$, i.e., $\sigma(r_s/10) > 0.1$ S.

3.5 Conclusions

In this Chapter, we present the results of the numerical Monte Carlo study of the conductivity of random NW networks for the wide range of densities and junction-to-NW conductance ratios. We observe the transition from the conductivity of the percolating cluster to the conductivity of the dense random NW networks with increasing density. Three limiting cases are identified for the conductivity of whole system: one in the vicinity of the percolation threshold, and two for high densities when either the junctions or NWs are superconductive. Each of these cases has a different exponent governing the power-law dependence of the conductivity on density (i.e., 1.29, 1, and 2, respectively). As a result, the exponent can take values anywhere in the range $(1, 2)$ depending on the junction-to-NW conductance ratio. For finite-size systems the density-dependent exponent can even take values lower than 1. Therefore, it is not appropriate to use a simple scaling law to describe the conductivity dependence on the density both for finite and dense systems. We instead propose a comprehensive conductivity model, derived from the behavior of the limiting cases. We find that the proposed description gives a satisfactory estimation of the conductivity and the local conductivity exponent (which is related to the first derivative of the conductivity) over the whole range of the NW density values. Finite-size effects, important for many practical realizations of the random conducting networks, are also included in the conductivity model. Finally, using the proposed model and an analytical approximation for the density-dependent optical transmittance, we quantify a dependence of the optical transmittance on the electrical conductivity for the random NW networks. The presented methodology could be used to describe the properties of other conducting systems (i.e., disks, spheres, and fibers).

Chapter 4 Random networks of carbon nanotubes optimized for transistor mass-production

As already noted, as-grown networks of single-walled (SW) CNTs contain both metallic (m-CNTs) and semiconducting (s-CNTs) nanotubes in an approximate ratio 1:2, which leads to a trade-off between on-conductance and the on/off conductance ratio [6, 47–50]. If the density of CNTs in a TFT is sufficiently high so that m-CNTs exceed the percolation threshold, the CNT network will become predominantly metallic and, hence, the on/off ratio will be very small [50]. In contrast, if the CNT density is so low that a conduction path through m-CNTs does not exist, a high on/off ratio can be attained, but under such circumstances the low on-conductance is disadvantage [50, 51]. In order to suppress a possibility of conduction through the m-CNTs, other researchers have used additional steps after or during the CNT synthesis process. However, all these steps prolongs the production time and increase the production costs or create defects and add impurities in the remaining CNT networks.

In this Chapter, we study effects of device parameters (density of CNTs, channel dimensions and CNT length) on their electrical transport processes, i.e., on the on-conductance and on/of conductance ratio, in order to design an optimized and uniform device performance without using any post-growth treatment. We identify the probabilities of different conduction regimes of random CNT networks using the scaling laws for asymmetric systems of percolating sticks developed in Chapter 2. Finally, we demonstrate how geometrical aspects contribute to the feasibility of the random CNT networks as switches with good transistor performance (i.e., high on-current and on/off ratio) and the uniform performance of realized devices.

4.1 Numerical method

Monte Carlo (MC) simulations are coupled with an efficient iterative algorithm implemented on the grid platform and are used to investigate the electrical properties of CNT networks [4–6, 99, 103]. We consider two-dimensional systems with isotropically placed CNTs modeled as widthless sticks with a fixed length l_{CNT}, as illustrated in Fig. 4.1(a). The centers of the CNTs are randomly positioned and oriented inside a channel with length L_{CH} and width W_{CH}, see Fig. 4.1(a). Source and drain electrodes are placed at the left and right sides of the channel. The top and bottom boundaries of the system are free and nonconducting, because free boundary conditions are more consistent with CNT networks in practice. The behavior of the CNT network is studied in terms of the normalized CNT density $n = N/\mathcal{L}^2$, where N is the total number of CNTs and $\mathcal{L} = \sqrt{LW}$ is the normalized channel size, where $L = L_{\mathrm{CH}}/l_{\mathrm{CNT}}$ is the normalized channel length and $W = W_{\mathrm{CH}}/l_{\mathrm{CNT}}$ is the normalized channel width, see Chapter 2. The aspect ratio of the system r is defined as the ratio of the channel length and width $r = L/W$. Without elaborated post-growth treatments, the CNTs synthesized using any available method are heterogeneous in the sense that they are always a mixture of metallic and semiconducting nanotubes with an approximate ratio of 1:2, i.e., the fraction of m-CNTs is $f_{\mathrm{M}} = 1/3$ and the rest are s-CNTs with the fraction $f_{\mathrm{S}} = 2/3$, see Refs. [56, 109].

An illustration of transfer characteristics (source-drain current I vs. gate voltage V_{G}) for the random CNT TFT with indicated on- I_{ON} and off-current I_{OFF} is shown in Fig. 4.1(b). Also, output characteristics (source-drain current I vs. source-drain voltage V) for the random CNT TFT are illustrated in Fig. 4.1(c). The illustrated transfer and output characteristics have the same form as the corresponding characteristics of standard p-type metal-oxide-semiconductor field-effect transistors. In this thesis, we only consider long-channel limits ($L_{\mathrm{CH}} > l_{\mathrm{CNT}}$) consistent with macroelectronics [47] and low-bias conditions under which nonlinear effects are negligible [109], i.e., the source-drain current I is proportional to the source-drain voltage V, as it can be observed in Fig. 4.1(c) when $V \approx 0$. For long-channel limits, conduction in the CNT network is described by percolation theory

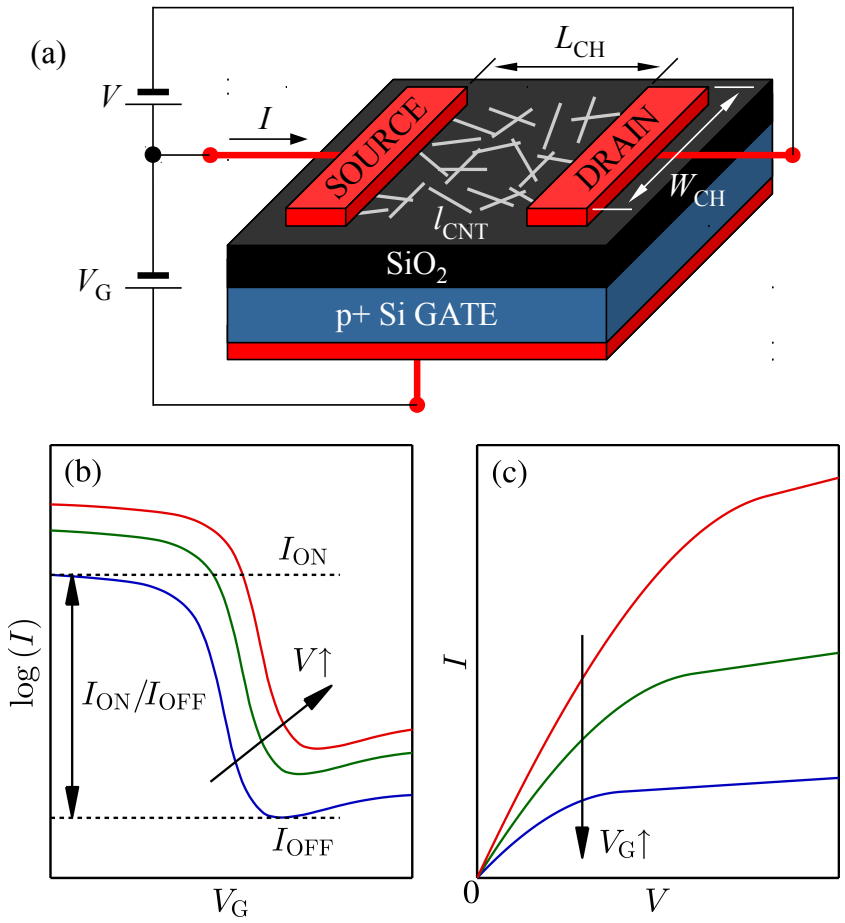

Figure 4.1: (a) Schematic illustration of a random CNT TFT consisting of highly doped p-type (p+) Si as its back-gate electrode, SiO_2 as its gate dielectric, and randomly distributed as-grown CNTs as its active medium. The reference directions of gate voltage V_G, source-drain voltage V, and source-drain current I are also indicated. (b) Transfer characteristics of the random CNT TFT (source-drain current I on a logarithmic scale vs. gate voltage V_G) with appropriate on- I_{ON} and off-current I_{OFF} are illustrated. The direction of the increase of source-drain voltage V is indicated on the graph. (c) Output characteristics (source-drain current I vs. source-drain voltage V) of the random CNT TFT are illustrated. The direction of the increase of gate voltage V_G is indicated on the graph.

as being that of a non-classical two-dimensional conductor, see Chapter 2. Two sticks (CNTs) belong to the same cluster if they intersect. The system percolates (conducts) if the electrodes (source and drain) are connected with the same cluster. The percolation threshold of the infinite-size stick system is defined by the critical density $n_c \approx 5.64$. Similarly, the percolation threshold of only s-CNTs (m-CNTs) is defined by the critical density $n_c/f_S \approx 8.46$ ($n_c/f_M \approx 16.9$).

The conductance along a CNT segment in the on-state, G_{seg}, is assumed to be uniform and can be calculated using Refs. [50, 59, 117]

$$G_{\text{seg}} = \frac{4e^2}{h}\frac{\lambda}{\lambda + l_{\text{seg}}}, \tag{4.1}$$

where e is the electron charge, h is Planck's constant, l_{seg} is the length of the CNT segment, and λ is the mean free path of the electrons, which is taken as 1.0 μm for m-CNTs and 0.3 μm for s-CNTs [118–120]. We consider that the conductance of an m-CNT is independent of the gate voltage [109] and in the off-state is also given by Eq. (4.1). At the same time, we assume that the conductance of an s-CNT in the off-state is 10^6 times lower than in the on-state, since the on/off ratio is usually about 10^6 for well-performing transistors based on individual s-CNTs [121, 122]. We note here that in real systems, the gate dielectric and gate leakage also contribute to the off-current, and thus the on/off ratio. Equation (4.1) assumes diffusive electrical transport through the CNTs typical for rodlike nanostructures whose length is larger than the mean free path of the electrons ($l_{\text{CNT}} \gg \lambda$). For the diffusive electrical transport the electrical conductance of a stick segment is inversely proportional to the length of the CNT segment $(4e^2/h)(\lambda/l_{\text{seg}})$, see Ref. [105, 112]. The conductance of a CNT whose length is lower than the mean free path of the electrons ($l_{\text{CNT}} \ll \lambda$) is near the ballistic transport limit $4e^2/h$ and also can be assumed by Eq. (4.1), see Ref. [118, 122].

Internal nodes for contacts between pairs of CNTs are distinguished from boundary nodes for contacts between CNTs and the source/drain electrodes. The contact conductances for the internal nodes are assigned the following values: (i) $0.1e^2/h$ for the junction between two m-CNTs or between two s-CNTs and (ii) 100 times lower conductance for the junction between one m-CNT and one s-CNT, since we neglect the rectifying behavior under low-bias conditions [109, 110]. The contact resistance at the boundary nodes is neglected since electrodes fabricated using, for example, Ti [58], Au [34], Pd [122], or aligned arrays of m-CNTs [123] yield good Ohmic contact to CNTs. Therefore, if a CNT intersects an electrode the potential of the electrode is applied to the intersection point. Kirchhoff's current law was used

to balance the current flow through each node of the created network. An iterative equation solver (i.e., CGM with Jacobi preconditioner explained in Appendix D) has been employed to solve a large system of linear equations following from Kirchhoff's laws, as it was explained in detail in section 3.1. After obtaining the total source-drain current I under an applied voltage V the macroscopic electrical conductance of the system is evaluated as $G = I/V$.[1] Finally, for each set of system parameters, electrical conductances for the on- and off-state are calculated for more than 10^5 independent MC realizations for systems with normalized size $L = W = 2$, down to 10^4 realizations for the largest system $L = W = 50$ studied. The results obtained using our conductance model show excellent agreement with recently published experimental results, see section 4.4. We note here that our conductance model can also be applied to random networks of multi-walled (MW) CNTs with a small diameter[2].

4.2 Symmetric-channel results

The randomly generated CNT network, if conducting, belongs to one of three complementary CNT network regimes according to its percolation characteristics: (i) neither m-CNT nor s-CNT paths exist but the whole network percolates through a mixed path comprising m- and s-CNTs ($\overline{\mathrm{S}}\overline{\mathrm{M}}$), (ii) only s-CNT paths exist ($\mathrm{S}\overline{\mathrm{M}}$),

[1] The on/off ratio is defined as the ratio of the on- and off-state currents determined at the same source-drain voltage V, i.e., $I_{\mathrm{ON}}/I_{\mathrm{OFF}}$. We only consider low-bias conditions, i.e., $V \approx 0$, under which nonlinear effects are negligible and the currents are given by $I_{\mathrm{ON}} = G_{\mathrm{ON}}V$ and $I_{\mathrm{OFF}} = G_{\mathrm{OFF}}V$, respectively. Hence, the on/off current ratio $I_{\mathrm{ON}}/I_{\mathrm{OFF}}$ is equal to the on/off conductance ratio, i.e., $G_{\mathrm{ON}}/G_{\mathrm{OFF}}$.

[2] SW CNTs have the smallest diameter of all CNTs, distributed within a narrow range ($d_{\mathrm{CNT}} = 0.8 - 5$ nm), and a length l_{CNT} from tens of nanometers to millimeters, whereas MW CNTs have a larger diameter ($\sim$ 3 to $>$ 100 nm) and lengths similar to those of SW CNTs, as noted in [11]. Our scaling model for systems of percolating sticks, which describes the operation regimes of random CNT TFTs, is valid for both SW and MW CNT networks as long as the CNTs can be modeled as widthless sticks, i.e., $l_{\mathrm{CNT}}/d_{\mathrm{CNT}} \gg 1$. On the other hand, the electrical characteristics of individual CNTs are primarily determined by their band gap [11]. It is well known that the band gap of an s-CNT depends inversely on its diameter. However, this dependence is not highly pronounced in the case of SW CNTs, since they have small diameters, distributed within a narrow range [11]. Therefore, our conductance model, which does not include the diameter of CNTs as a parameter, is applicable to SW CNT networks, as shown in the supplementary material, section 1. For the same reason, our conductance model is applicable to the random networks of MW CNTs with small diameters ($d_{\mathrm{CNT}} < 5$ nm), because each individual nanotube in a small-diameter MW CNT behaves similar to a SW CNT [11].

and (iii) at least one m-CNT path exists (M).

Figure 4.2 illustrates the structure of the CNT networks and the redistribution of the currents in on- and off-state with increasing CNT density n. When the CNT density n increases the randomly generated CNT network moves from one operation regime to another. The first regime ($\overline{\mathrm{S}}\overline{\mathrm{M}}$) corresponds to a situation when the density of CNTs ($n = 8$) is higher than the percolation threshold of the entire network n_c but lower than the percolation threshold of only s-CNTs ($n_\mathrm{c} < n < n_\mathrm{c}/f_\mathrm{S}$). In this situation the percolating network consists mixed m- and s-CNTs. As a result, the on-conductance G_ON and resulting on-current I_ON are reduced by the presence of the low-conducting s-CNT/m-CNT junctions, see Fig. 4.2(a). At the same time, since an m-CNT path does not exist, off-conductance is low and therefore, the on/off ratio is high, see Figs. 4.2(a) and (b). The second operation regime ($\mathrm{S}\overline{\mathrm{M}}$) occurs for the medium CNT density ($n_\mathrm{c}/f_\mathrm{S} < n < n_\mathrm{c}/f_\mathrm{M}$) when only s-CNT paths exist, and the current flows through high-conducting s-CNT/s-CNT junctions resulting in a high on-current I_ON, see Fig. 4.2(c). However, the CNT density ($n = 12$) is still lower than the percolation threshold of only m-CNTs and the CNT TFT in the off-state is not short-circuited through an m-CNT path. Therefore, the CNT network can simultaneously achieve high on-conductance G_ON and a high on/off ratio $G_\mathrm{ON}/G_\mathrm{OFF}$, see Figs. 4.2(c) and 4.2(d). Finally, the third regime (M) of the CNT network according to the percolation characteristics occurs at densities close to and above the percolation threshold of only m-CNTs, i.e., $n_\mathrm{c}/f_\mathrm{M}$. For a high CNT density ($n = 16$) at least one m-CNT path exists and a high on-conductance is obtained, see Fig 4.2(e). On the other hand, in the off-state the CNT network is shorted through the m-CNTs and, hence, the on/off ratio is very low, see Figs. 4.2(e) and 4.2(f). Therefore, the CNT network in the M operation regime cannot be used as an active media for transistors with a high switching performance.

According to the determined parameters for moments of the percolation probability distribution function given in section 2.4, we will determine a region of the CNT density n where s-CNT paths are dominant ($\mathrm{S}\overline{\mathrm{M}}$) and, therefore, the on-current and on/off ratio are expected to be high. Details of our analytic model for the percolation probability functions for symmetric channels are given in the next subsection.

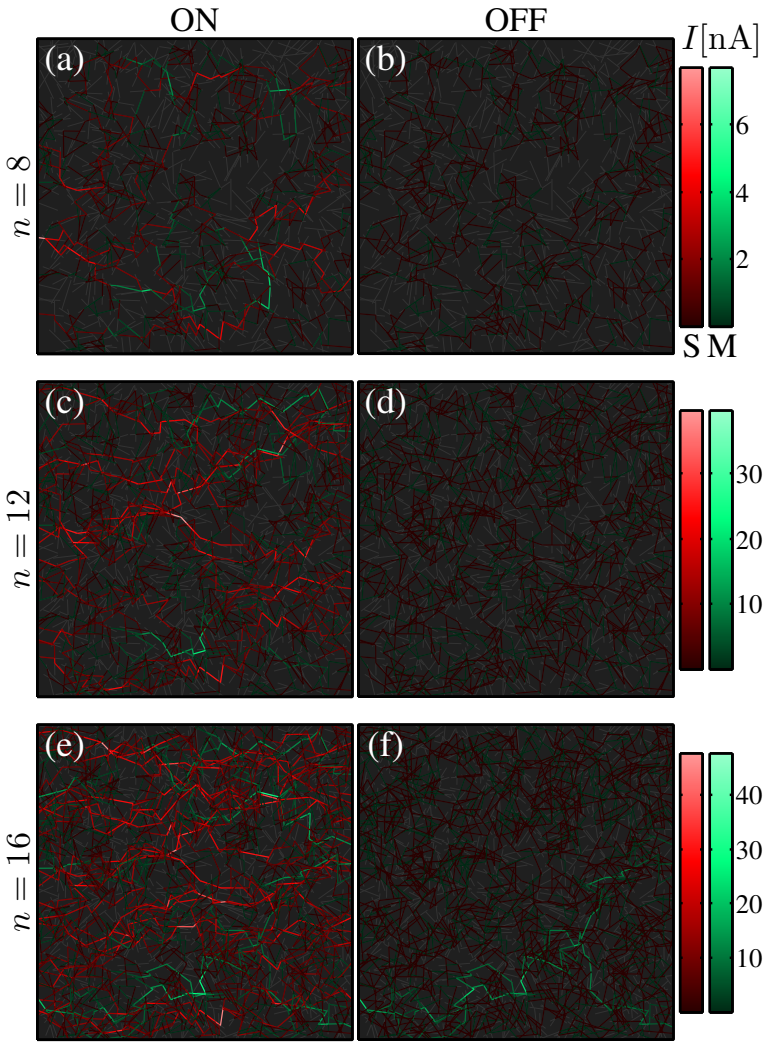

Figure 4.2: Simulated on- ((a), (c), and (e)) and off-current ((b), (d), and (f)) distributions for different CNT densities. The source-drain voltage is $V = 0.1$ V, the CNT length is $l_{\mathrm{CNT}} = 5$ μm, and the channel dimensions are $L_{\mathrm{CH}} = W_{\mathrm{CH}} = 50$ μm, i.e., the normalized system size is $L = 10$. (a) When the density of CNTs ($n = 8$) is significantly lower than the percolation threshold of only s-CNTs ($n < n_{\mathrm{c}}/f_{\mathrm{S}}$), the dominant percolation domain is through mixed paths comprising m- and s-CNTs ($\overline{\mathrm{SM}}$). (b) Since there is no percolating path through only m-CNTs the off-current is low, i.e., the on/off ratio is high. (c) For a higher CNT density ($n = 12$) only s-CNT paths exist ($\mathrm{S}\overline{\mathrm{M}}$), resulting in a high on-current I_{ON}. (d) This CNT density ($n = 12$) is still lower than the percolation threshold of only m-CNTs and, therefore, the CNT TFT is not short-circuited in the off-state and the on/off ratio is still high. (e) For high CNT density ($n = 16$) the m-CNT network percolates. (f) The CNT network in the off-state is shorted through the m-CNTs.

4.2.1 Symmetric-channel percolation probability

Here we calculate the percolation probability dependence on the system size and density for three types of CNT networks: $\overline{\mathrm{S}}\overline{\mathrm{M}}$, $\mathrm{S}\overline{\mathrm{M}}$, and M. For a symmetric-channel configuration the normalized length, width, and system size are equal, i.e., $L = W = \mathcal{L}$. The percolation probability function $R_{n,L}$ gives the probability that the network with the total CNT density n and the normalized system size L percolates in the source-to-drain direction. Similarly, the corresponding probability of the CNT network with the density n and the normalized system size L to achieve the percolation of $\overline{\mathrm{S}}\overline{\mathrm{M}}$, $\mathrm{S}\overline{\mathrm{M}}$, or M operation regime are $R_{n,L}^{\overline{\mathrm{S}}\overline{\mathrm{M}}}$, $R_{n,L}^{\mathrm{S}\overline{\mathrm{M}}}$, and $R_{n,L}^{\mathrm{M}}$, respectively. Finally, from the complementarity of $\overline{\mathrm{S}}\overline{\mathrm{M}}$, $\mathrm{S}\overline{\mathrm{M}}$, and M domains for a randomly generated CNT network we obtain

$$R_{n,L}^{\overline{\mathrm{S}}\overline{\mathrm{M}}} + R_{n,L}^{\mathrm{S}\overline{\mathrm{M}}} + R_{n,L}^{\mathrm{M}} = R_{n,L}. \tag{4.2}$$

The percolation probability function $R_{n,L}$ can be approximated by a cumulative distribution function given by Eq. (2.28) as it was explained in section 2.6. Similarly, the percolation probability function of an M configuration can also be approximated by Eq. (2.28) as follows

$$R_{n,L}^{\mathrm{M}} = R_{f_{\mathrm{M}}n,L}, \tag{4.3}$$

while the probability to attain an $\mathrm{S}\overline{\mathrm{M}}$ configuration is

$$R_{n,L}^{\mathrm{S}\overline{\mathrm{M}}} = R_{f_{\mathrm{S}}n,L}\left(1 - R_{f_{\mathrm{M}}n,L}\right), \tag{4.4}$$

and finally for an $\overline{\mathrm{S}}\overline{\mathrm{M}}$ configuration from Eqs. (4.2), (4.3), and (4.4) we obtain

$$R_{n,L}^{\overline{\mathrm{S}}\overline{\mathrm{M}}} = R_{n,L} - R_{f_{\mathrm{S}}n,L} - R_{f_{\mathrm{M}}n,L} + R_{f_{\mathrm{S}}n,L}R_{f_{\mathrm{M}}n,L}. \tag{4.5}$$

According to Eqs. (2.28) and (4.3)-(4.5) we can approximate the percolation probability functions for as-grown CNT networks using the normalized system size L, the density n, and the finite-size scaling constants for two-dimensional stick systems given in Table 2.1. This is demonstrated in Fig. 4.3. The derived expressions for

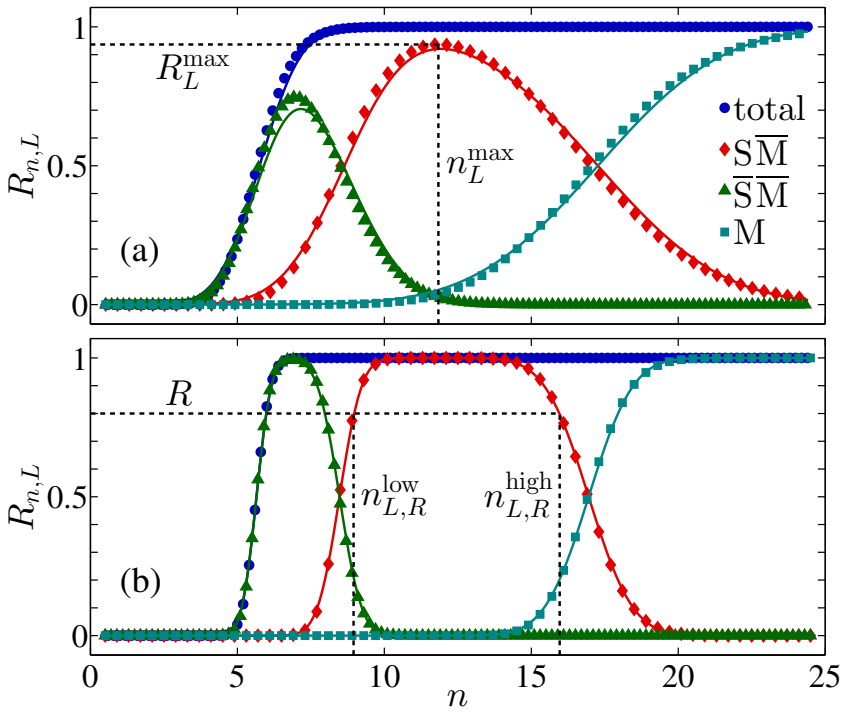

Figure 4.3: The percolation probability dependence on the normalized density n for overall percolation $R_{n,L}$ and different percolation regimes $R_{n,L}^{\text{S}\overline{\text{M}}}$, $R_{n,L}^{\overline{\text{S}}\overline{\text{M}}}$, and $R_{n,L}^{\text{M}}$. The points are the MC simulation results and the solid lines are obtained using Eqs. (2.28) and (4.3)-(4.5). (a) For the normalized system size $L = 5$ percolation probability variance is comparable to the system size and overlaps exist between $\overline{\text{S}}\overline{\text{M}}$, S$\overline{\text{M}}$, and M regimes. Normalized density $n_L^{\max}$ determines value where percolation probability through only s-CNT paths $R_{n,L}^{\text{S}\overline{\text{M}}}$ reaches its maximum $R_L^{\max}$. (b) When the normalized system size is larger, $L = 20$, the percolation regimes become well defined. Values $n_{L,R}^{\text{low}}$ and $n_{L,R}^{\text{high}}$ determine a range of densities where percolation probability of realizations through only s-CNT paths $R_{n,L}^{\text{S}\overline{\text{M}}}$ is higher than a relative number R ($0 \leq R \leq 1$).

the percolation probability functions, i.e., $R_{n,L}$, $R_{n,L}^{\text{S}\overline{\text{M}}}$, $R_{n,L}^{\overline{\text{S}}\overline{\text{M}}}$, and $R_{n,L}^{\text{M}}$, represent an excellent fit to the data calculated using our MC simulations.

For a small system size $L = 5$ the percolation probability variance is large compared to the system size and the overlap exists between $\overline{\text{S}}\overline{\text{M}}$, S$\overline{\text{M}}$, and M regimes, see Fig. 4.3(a). For the densities $n < 8$ the number of $\overline{\text{S}}\overline{\text{M}}$ realizations is higher than the number of S$\overline{\text{M}}$ realizations, while the number of realizations with metallic paths M is negligible. Still, this is far from a satisfactory situation, since the conduction through a combined network of s- and m-CNTs leads to a degradation of the device characteristics, i.e., to lower values of the on-conductance G_{ON}, see Fig. 4.5(a). The

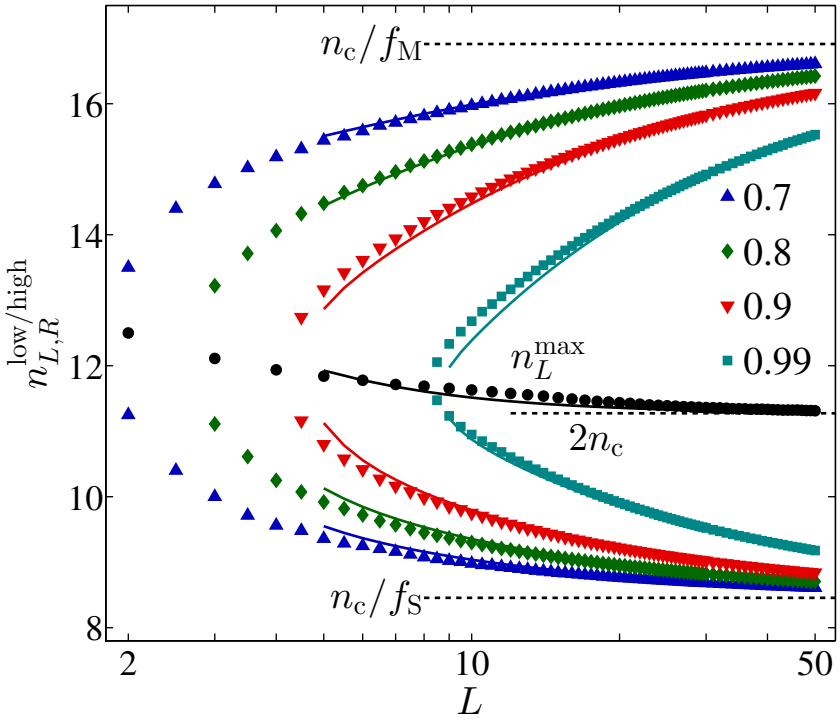

Figure 4.4: The dependence of the $S\overline{M}$-dominant region on the normalized system size L, for different tolerances $R = 0.7, 0.8, 0.9$, and 0.99. The points are the MC simulation results and the solid lines are obtained using our analytic model given by Eqs. (2.28) and (4.3)-(4.5). With increasing system size L, the value of CNT density n_L^{max}, where the percolation probability only through s-CNT paths $R_{n,L}^{S\overline{M}}$ reaches its maximum, converges to $2n_c$, the low-bound density $n_{L,R}^{low}$ to n_c/f_S, and the high-bound density $n_{L,R}^{high}$ to n_c/f_M.

increase of the normalized system size L is beneficial for overall transistor performance. For $L = 20$, see Fig. 4.3(b), the three regimes $\overline{S}\overline{M}$, $S\overline{M}$, and M become well resolved. We also note that the maximum of the $S\overline{M}$ percolation probability R_L^{max} increases with increasing the normalized system size L and converges to a value of 1, see Figs. 4.3(a) and 4.3(b).

Following this, we define a density range with lower $n_{L,R}^{low}$ and upper boundary $n_{L,R}^{high}$, where the probability of percolation only through s-CNT paths $R_{n,L}^{S\overline{M}}$ is higher than a relative number R ($0 \leq R \leq 1$), see Fig. 4.3. As one would expect, the range defined by $n_{L,R}^{high}$ and $n_{L,R}^{low}$ increases with the normalized system size L and decreases with R, see Fig. 4.4. We can further observe interesting features of the shape of the $S\overline{M}$ percolation density range with increasing system size: (i) the position of $S\overline{M}$

percolation probability maximum $n_L^{\max}$ converges to $2n_c$ with increasing system size, (ii) the low-bound density $n_{L,R}^{\text{low}}$ decreases and converges to the percolation threshold of s-CNT paths n_c/f_S, and (iii) the high-bound density $n_{L,R}^{\text{high}}$ increases and converges to the percolation threshold of m-CNT paths n_c/f_M, see Fig. 4.4.

4.2.2 Symmetric-channel on-conductance and on/off ratio

In the rest of this section, we will quantify the dependence of the calculated on-conductance and on/off ratio on the CNT density, length, and system size. The aim of this paper is to restrict the ranges of these parameters for which acceptable transistor characteristics are obtained with a realization probability higher than 99%. For most kinds of integrated circuit applications the acceptable values for on-conductance and on/off ratio are 1 μS and 10^4, respectively [56, 119, 124].

In Fig. 4.5, probability distribution functions of the on-conductance G_{ON} and the on/off ratio G_{ON}/G_{OFF} are given for different CNT densities: $n = 8, 12$, and 16. For $n = 8$, we observe a wide distribution for both the corresponding on-conductance G_{ON} and the on/off ratio G_{ON}/G_{OFF} due to a detrimental influence of mixed paths ($\overline{S}\overline{M}$), see Figs. 4.5(a) and 4.5(d). On the other hand, for $n = 12$, which roughly corresponds to $2n_c$, we observe roughly 10 times higher on-conductance G_{ON} and a narrower distribution of the on/off ratio G_{ON}/G_{OFF}, centered at about 10^4, see Figs. 4.5(b) and 4.5(e). However, due to the small system size $L = 5$ we observe a number of realizations consisting of m-CNT paths with the on/off ratio less than 10. This is an unwanted situation in any application, and it can be resolved by increasing the normalized system size L. Further increase of the CNT density n only degrades the switching on/off performance of random CNT networks. For $n = 16$, the number of short-circuited realizations is approaching 50%, see Fig. 4.5(c) and 4.5(f).

The results are shown in Fig. 4.6 as a function of the CNT normalized density n for $l_{CNT} = 5$ μm and the system size $W_{CH} = L_{CH} = 100$ μm, i.e., the normalized system size $L = 20$. The on-conductance G_{ON} increases with CNT density n and the 1st and 99th percentiles converge to the median value, see Fig. 4.6(a). The difference between the 99th and 1st percentile of the on/off ratio G_{ON}/G_{OFF} reaches a minimum close to $n_{20}^{\max}$ and rapidly increases when the CNT density n becomes

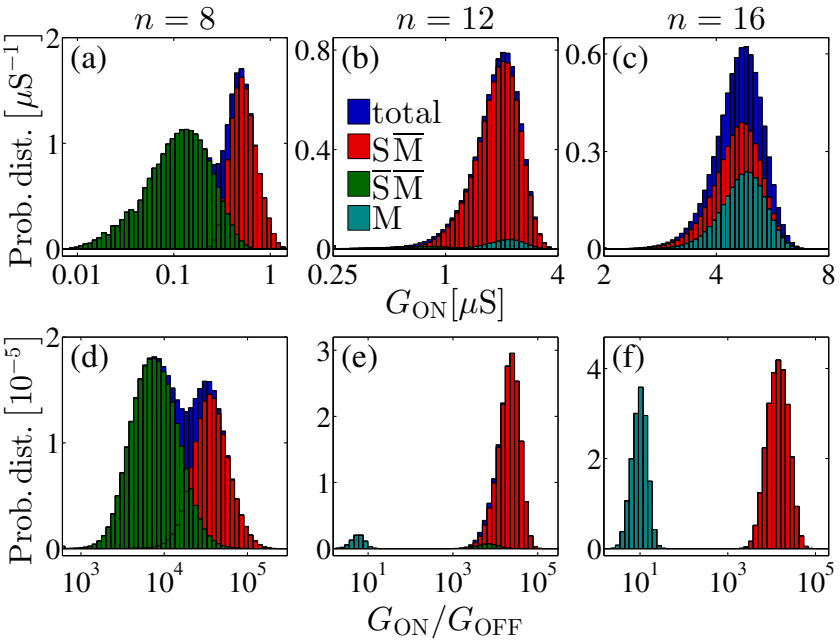

Figure 4.5: The probability distribution functions of the on-conductance G_{ON} (a), (b), and (c) and the on/off ratio $G_{\mathrm{ON}}/G_{\mathrm{OFF}}$ (d), (e), and (f) for overall and particular conduction regimes $\overline{\mathrm{S}}\overline{\mathrm{M}}$, $\mathrm{S}\overline{\mathrm{M}}$, and M are given for different CNT densities. The CNT length is $l_{\mathrm{CNT}} = 5$ μm, the channel length is $W_{\mathrm{CH}} = L_{\mathrm{CH}} = 25$ μm, i.e., the normalized system size is $L = 5$, and the number of independent MC realization is higher than 10^7.

higher than $n^{\mathrm{high}}_{20,0.99}$, see Fig. 4.6(b). For densities higher than $n^{\mathrm{high}}_{20,0.99}$ the percolation probability of M configurations $R^{\mathrm{M}}_{n,L}$ is higher than 1%, i.e., $R^{\mathrm{M}}_{n,L} > 1\%$, and therefore the 1st-percentile realization belongs to the M regime and a sharp decrease in on/off behavior is obtained. One can observe that the maximum of the on/off ratio is between the densities $n^{\mathrm{low}}_{20,0.99}$ and $n^{\mathrm{high}}_{20,0.99}$. More than 99% of realized devices exhibit simultaneously on-conductance higher than 1 μS and an on/off ratio higher than 10^4 when the normalized density n is close to n^{max}_{20}, see Figs. 4.6(a) and 4.6(b).

A similar behavior of the on-conductance G_{ON} and on/off ratio $G_{\mathrm{ON}}/G_{\mathrm{OFF}}$ can be observed in Fig. 4.7(a) with increasing the normalized system size L. While the percentiles of the on-conductance G_{ON} experience continuous convergence to the infinite system value, the on/off ratio exhibits a sharp transition in the 1st-percentile behavior at the normalized system size $L \approx 7$. For a system size bellow $L < 7$ the percolation probability of realizations through only m-CNTs is higher than 1%, i.e., $R^{\mathrm{M}}_{n,L} > 1\%$, and therefore the 1st-percentile realization is short-circuited

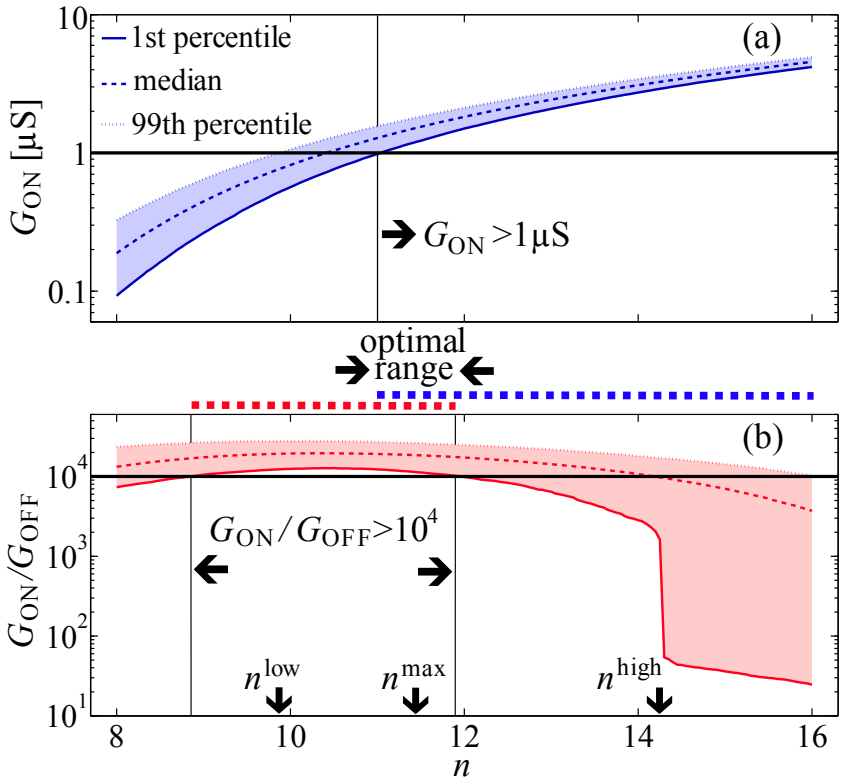

Figure 4.6: On-conductance G_{ON} (a) and on/off ratio G_{ON}/G_{OFF} (b) as a function of the normalized CNT density n for a symmetric TFT with the CNT length l_{CNT} = 5 μm and the channel size $L_{CH} = W_{CH}$ = 100 μm, i.e., the normalized system size $L = 20$. The solid line represents the 1st percentile, while the dashed and dotted lines correspond to the median and 99th percentile, respectively, of the device population. The arrows denote regions where more than 99% of realized devices have: (a) on-conductance higher than 1 μS (horizontal bold line) or (b) an on/off ratio higher than 10^4 (horizontal bold line). The positions of the lower $n^{low}_{20,0.99}$ and higher $n^{high}_{20,0.99}$ bounds of the 0.99 percolation probability for the $S\overline{M}$ regime are also given, as well as the position of $S\overline{M}$ probability maximum n^{max}_{20}.

with $G_{ON}/G_{OFF} < 10$, see Fig. 4.5. On the other hand, more than 99% of realized devices exhibit simultaneous on-conductance higher than 1 μS and an on/off ratio higher than 10^4 when the normalized system size is $L > 16$, see Fig. 4.7(a).

The influence of CNT length l_{CNT} on the transistor performance is explored in Fig. 4.7(b). Here, the normalized system size is fixed and large, $L = 20$, in order to minimize the influence of finite-size scaling effects on the transistor performance, see Ref. [125]. Therefore, on-conductance G_{ON} and on/off ratio G_{ON}/G_{OFF} depend only on the electrical characteristics of individual nanotubes, i.e., their length l_{CNT},

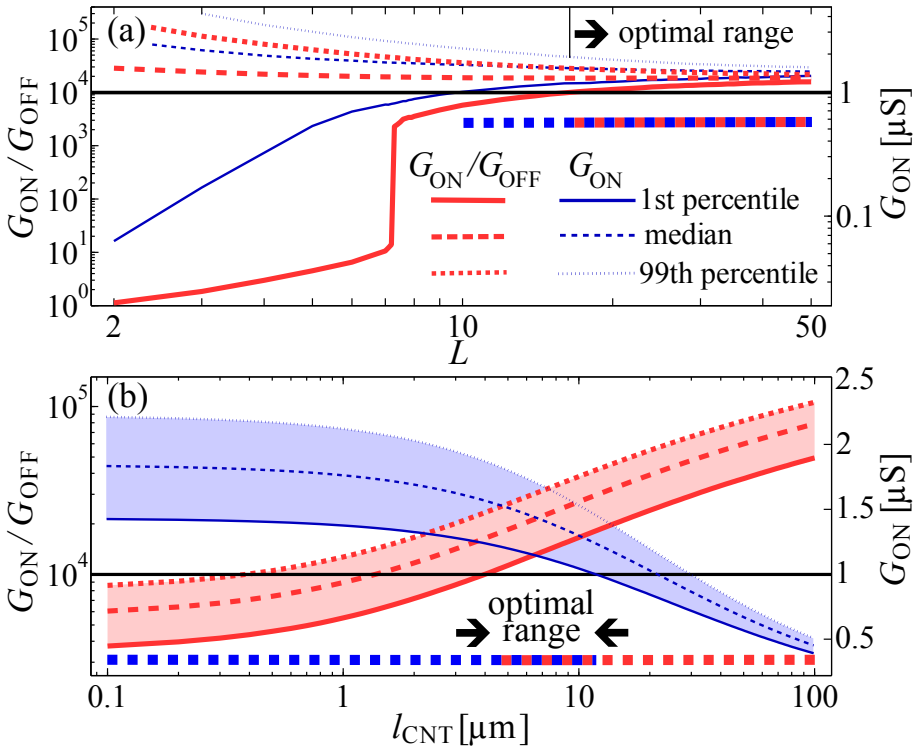

Figure 4.7: The dependence of on-conductance G_{ON} and the on/off ratio G_{ON}/G_{OFF} on (a) the normalized system size L for symmetric-channel TFTs with CNT length $l_{CNT} = 5$ μm and a normalized density equal to n_L^{max} and (b) the CNT length l_{CNT} for a symmetric system with the normalized size $L = 20$ and a normalized CNT density n equal to $n_{20}^{max} = 11.45$. The solid lines represent the 1st percentile, while the dashed and dotted lines correspond to the median and 99th percentile, respectively, of the device population. The arrows denote regions where more than 99% of realized devices have on-conductance higher than 1 μS and an on/off ratio higher than 10^4 (horizontal bold lines).

in accordance with Eq. (4.1). When the CNT length l_{CNT} is larger than the electron mean free path, i.e., $l_{CNT} > 1$ μm, diffusive transport in CNTs becomes dominant and the on-conductance G_{ON} of the network starts to decrease linearly with the CNT length, see Fig. 4.7(b). At the same time, due to an increased resistance of m-CNTs, leak-currents in the off-state through the m-CNTs decrease and the on/off ratio improves with increasing CNT length, see Fig. 4.7(b). It is important to note that in this trade-off, the improvement of the on/off ratio is one order of magnitude with increasing l_{CNT} from 1 μm to 10 μm while G_{ON} decreases only 10%. However, more than 99% of realized devices exhibit simultaneously high on-conductance and a

high on/off ratio when the CNT length is between $l_{\mathrm{CNT}} = 4-12\ \mu$m, see Figs. 4.7(b).

4.3 Asymmetric-channel results

Asymmetric systems have lower finite-size scaling exponents than symmetric systems. This results in more pronounced finite-size scaling behavior than in the symmetric case and allows us even more design freedom. In this section we will performed a parameter study to find the optimal channel dimensions for asymmetric-channel CNT TFTs.

4.3.1 Asymmetric-channel percolation probability

Similarly to the case of the symmetric channel, the overall percolation probability function of an asymmetric channel $R_{n,L,W}$ can be approximated by the cumulative distribution function given by Eq. (2.28) using the average percolation density $\langle n\rangle_{L,W}$ given by Eq. (2.20) and the percolation density standard deviation $\Delta_{L,W}$ given by Eq. (2.21), where the corresponding finite-size scaling exponents are given in Table (2.1).[1] Also, the percolation probability functions for the three regimes of CNT percolation (M, S$\overline{\mathrm{M}}$, and $\overline{\mathrm{S}}\overline{\mathrm{M}}$) can be calculated using Eqs. (4.3), (4.4), and (4.5), respectively. We have previously found in Chapter 2 that the average percolation density of asymmetric systems $\langle n\rangle_{L,W}$ has a lower exponent, i.e., the first-order effects are presented through the exponent $-1/\nu$, compared to the second-order effects in the case of symmetric systems and the exponent $-1/\nu - \theta_1$. This results in a more pronounced finite-size scaling behavior in the asymmetric case for the average percolation density $\langle n\rangle_{L,W}$ and the percolation density standard deviation $\Delta_{L,W}$.

Using Eqs. (2.28) and (4.3)-(4.5) we can approximate the percolation probability functions for as-grown CNT networks using the normalized system size $\mathcal{L}$, the aspect ratio r, the density n, the fraction of the m-CNTs f_{M}, and the finite-size scaling coefficients and exponents for the two-dimensional stick systems. This is demonstrated

[1] As already noted, the conversion of the normalized channel length L and width W to the normalized channel size $\mathcal{L}$ and aspect ratio r can be done according to $\mathcal{L} = \sqrt{LW}$ and $r = L/W$, and in the opposite direction $L = \mathcal{L}\sqrt{r}$ and $W = \mathcal{L}/\sqrt{r}$.

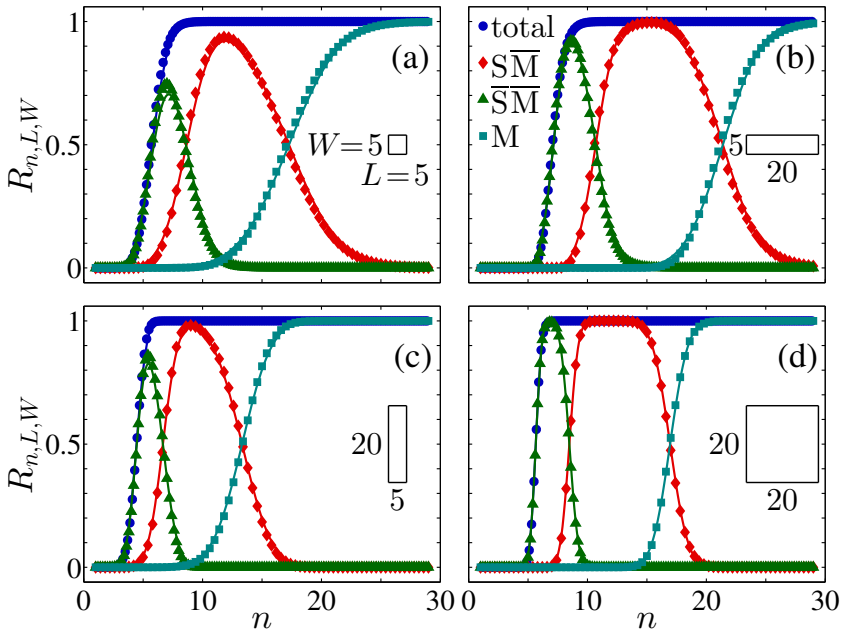

Figure 4.8: The percolation probability functions of two symmetric (a) and (d) and two asymmetric systems (b) and (c). Different percolation characteristics are shown: for overall CNT percolation $R_{n,L,W}$ and for three operation regimes $R^{\text{S}\overline{\text{M}}}_{n,L,W}$, $R^{\overline{\text{S}}\overline{\text{M}}}_{n,L,W}$, and $R^{\text{M}}_{n,L,W}$. The points are the MC simulation results and the solid lines are obtained using Eqs. (2.28) and (4.3)-(4.5).

in Fig. 4.8, where the derived expressions for the percolation probability functions represent an excellent fit to the data calculated using our MC simulations. Two symmetric systems with $L = 5$ and 20 are compared with the asymmetric ones with the aspect ratios $r = 1/4$ and 4. The overlap between $\overline{\text{S}}\overline{\text{M}}$, S$\overline{\text{M}}$, and M regimes for the long-channel system with $r = 4$ is lower in comparison to the narrow-channel configuration with $r = 1/4$, see Figs. 4.8(b) and 4.8(c). Unfortunately, long-channel configurations, e.g., $r = 4$, suffer from a low on-conductance due to the long pathways for the electrical transport in the source-to-drain direction [51, 126]. However, the CNT density n is proportional to the collection time during a chemical vapor deposition process and it can be controlled precisely by adjusting the collection time as shown in Ref. [39]. The precise control of the density n during the CNT synthesis process enables production of transistors with the narrow S$\overline{\text{M}}$ density regions, i.e., narrow channels. Hence, we can conclude that decrease of the channel length L, i.e., decrease of the aspect ratio r, is a good strategy for the performance improvement for two reasons: (i) the on-conductance increases with decreasing the aspect

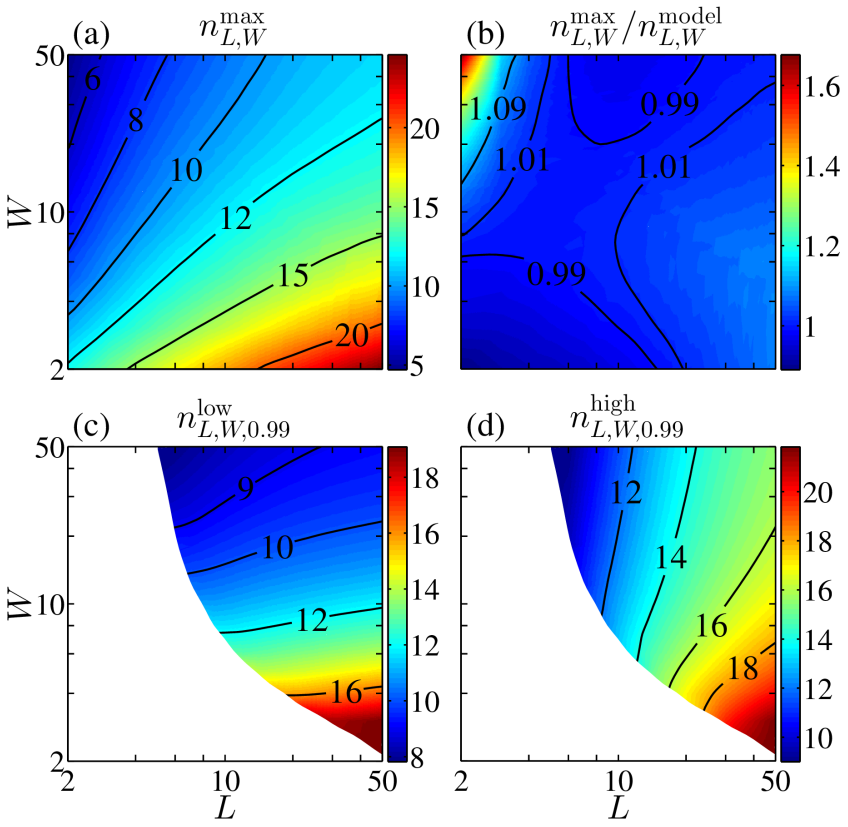

Figure 4.9: The dependence of (a) the normalized density $n_{L,W}^{\max}$ where the probability of S$\overline{\text{M}}$ percolation reaches maximum and (b) the ratio between the MC simulation results $n_{L,W}^{\max}$ on the values $n_{L,W}^{\text{model}}$ obtained using our analytic model given by Eqs. (2.28) and (4.3)-(4.5) on the normalized channel width W and length L. The low-bound $n_{L,W,0.99}^{\text{low}}$ (c) and high-bound density $n_{L,W,0.99}^{\text{high}}$ (d) determine a density range where the probability of S$\overline{\text{M}}$ realizations is higher than 0.99.

ratio [126] and (ii) the percolation through only s-CNT paths for a narrow-channel configuration occurs at lower densities, see Figs. 4.8(b) and 4.8(c), resulting in a faster production of random CNT TFTs.

For asymmetric-channel configurations the dependence of the normalized density where S$\overline{\text{M}}$ percolation probability reaches its maximum $n_{L,W}^{\max}$ on the normalized system dimensions L and W is shown in Fig. 4.9(a). The normalized density $n_{L,W}^{\max}$ increases with increasing normalized channel length L and decreases with increasing width W, see Fig. 4.9(a). The agreement between the MC simulation results $n_{L,W}^{\max}$ and the values $n_{L,W}^{\text{model}}$ obtained from our analytic model given by Eqs. (2.28) and (4.3)-(4.5) is better than 1% for the systems with $L > 5$, see Fig. 4.9(b). From Figs. 4.9(c) and 4.9(d) we expect to achieve 99% only s-CNTs conducting realizations

roughly above the line $L_{\mathrm{CH}}W_{\mathrm{CH}} > 250\, l_{\mathrm{CNT}}^2$. Within that region we see that $n_{L,W,0.99}^{\mathrm{low}}$ primarily depends on the system width W. On the other hand, the upper limit of the 99% confidence region, $n_{L,W,0.99}^{\mathrm{high}}$ depends on both the normalized length L and width W.

4.3.2 Asymmetric-channel on-conductance and on/off ratio

The random CNT TFTs with an asymmetric channel have similar characteristics of the on-conductance G_{ON} and on/off ratio $G_{\mathrm{ON}}/G_{\mathrm{OFF}}$ compared to the symmetric-channel configurations, see Figs. 4.6 and 4.10. The on-conductance G_{ON} also increases with increasing CNT density n and the 1st and 99th percentiles converge to the median value, see Fig. 4.10(a). The difference between the 99th and 1st percentile of the on/off ratio $G_{\mathrm{ON}}/G_{\mathrm{OFF}}$ also reaches its minimum close to the density where the probability of S$\overline{\mathrm{M}}$ percolation reaches its maximum, i.e., $n_{8,50}^{\mathrm{max}}$, and rapidly increases when the CNT density becomes higher than $n_{8,50,0.99}^{\mathrm{high}}$, see Fig. 4.10(b). Similarly, the maximum of the on/off ratio is between densities $n_{8,50,0.99}^{\mathrm{low}}$ and $n_{8,50,0.99}^{\mathrm{high}}$, and more than 99% of realized devices exhibit simultaneously on-conductance higher than 1 μS and an on/off ratio higher than 10^4 when the normalized density n is close to $n_{8,50}^{\mathrm{max}}$, see Figs. 4.10(a) and 4.10(b). Hence, the density $n_{L,W}^{\mathrm{max}}$ for asymmetric, as well as symmetric, configurations can be used as a compromise value for obtaining the optimized transistor performance, see Figs. 4.6 and 4.10. However, narrow-channel configurations generally have a higher on-conductance compared to symmetric channels as noted in Ref. [126]. Indeed, as can be seen from Figs. 4.6(a) and 4.10(a), a narrow-channel TFT with the aspect ratio $r = 8/50$ has roughly $1/r \approx 6$ times higher on-conductance G_{ON} compared to the symmetric-channel configuration with the same normalized channel size $\mathcal{L}$ and CNT length l_{CNT}.

The 1st percentiles of the on-conductance G_{ON} and on/off ratio $G_{\mathrm{ON}}/G_{\mathrm{OFF}}$ are calculated for the same structural parameters L, W, and $n_{L,W}^{\mathrm{max}}$, and different CNT lengths $l_{\mathrm{CNT}} = 4, 8,$ and 12 μm, see Fig. 4.11. In accordance with the results shown for the symmetric-channel configuration in Fig. 4.7(b) we note that with increasing CNT length l_{CNT} the on-conductance G_{ON} decreases, while the on/off ratio $G_{\mathrm{ON}}/G_{\mathrm{OFF}}$ increases, see Fig. 4.11. When the CNT length l_{CNT} is bellow 4 μm

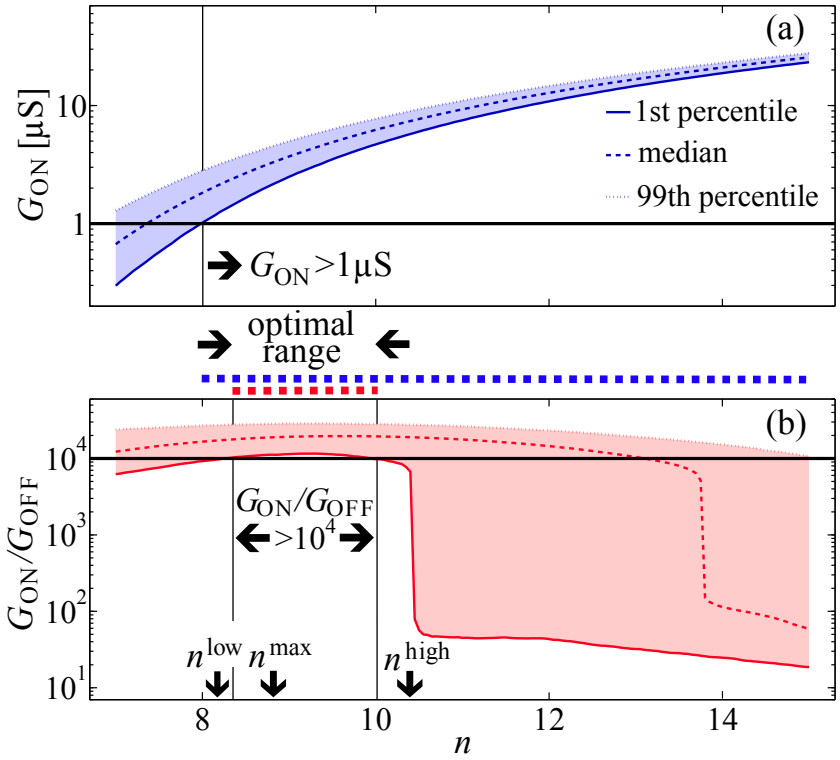

Figure 4.10: On-conductance G_{ON} (a) and on/off ratio G_{ON}/G_{OFF} (b) as a function of the normalized CNT density n for a narrow-channel TFT with the CNT length $l_{CNT} = 5$ μm and the channel dimensions $L_{CH} = 40$ μm and $W_{CH} = 250$ μm, i.e., the normalized system dimensions $L = 8$ and $W = 50$. The solid line represents the 1st percentile, while the dashed and dotted lines correspond to the median and 99th percentile, respectively, of the device population. The arrows denote regions where more than 99% of realized devices have: (a) on-conductance higher than 1 μS (horizontal bold line) or (b) on/off ratio higher than 10^4 (horizontal bold line). The positions of the lower $n^{low}_{8,50,0.99}$ and higher $n^{high}_{8,50,0.99}$ bounds of the 0.99 percolation probability for $S\overline{M}$ regime are also given, as well as the position of $S\overline{M}$ probability maximum $n^{max}_{8,50}$.

ballistic electrical transport becomes dominant and the on/off ratio becomes lower than 10^4, see Figs. 4.11(b), 4.11(d), and 4.11(f). On the other hand, when l_{CNT} is higher than 20 μm, high on-conductance can be attained only for a very large channel with dimensions of the order of 1 mm, see Fig. 4.11(e). Hence, the CNT length in the range $l_{CNT} = 4 - 20$ μm results in an acceptable balance between the on-conductance and on/off performance of CNT TFTs.

Regions A and B in Fig. 4.11 represent the CNT networks with a low 1st-percentile value of the on-conductance G_{ON}. Region A is defined as a region where

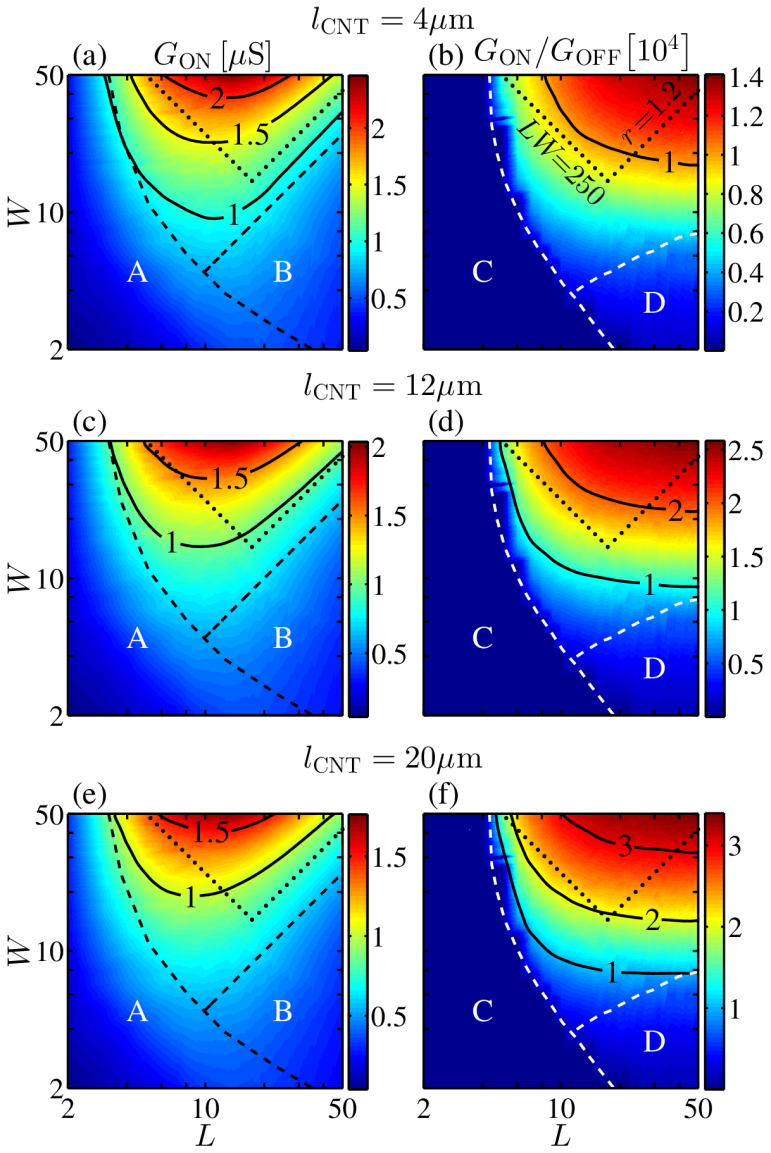

Figure 4.11: The results for the 1st percentile of the on-conductance G_{ON} ((a), (c), and (e)) and the on/off ratio G_{ON}/G_{OFF} ((b), (d), and (f)) calculated at $n^{max}_{L,W}$ as a function of the normalized channel width W and length L for different CNT lengths $l_{CNT} = 4, 12$, and 20 μm. Region A represents CNT TFT configurations with a probability of $\overline{\text{S}}\overline{\text{M}}$ percolation higher than 1%, i.e., $R^{\overline{\text{S}}\overline{\text{M}}}_{n,L,W} > 1\%$, while region B represents configurations with a high aspect ratio (here $r > 2$). TFTs in the C region feature networks with a probability of M percolation higher than 1%, i.e., $R^{\text{M}}_{n,L,W} > 1\%$, while the region D denotes networks with a high CNT density (here $n > 15$). The area above the dotted lines ($LW = 250$ and $L/W = 1.2$) can be used as an approximation of the region where the random CNT TFTs simultaneously attain high on-conductance and a high on/off ratio.

the probability of $\overline{\mathrm{SM}}$ percolation is higher than 1%, i.e., $R^{\overline{\mathrm{SM}}}_{n,L,W} > 1\%$, and therefore the 1st-percentile realization is a mixed path with low-conducting s-CNT/m-CNT junctions. The realizations in region B have a high value of the aspect ratio r and therefore a low overall on-conductance [126]. On the other hand, regions C and D in Fig. 4.11 represent the CNT networks with a low 1st-percentile value of the on/off ratio $G_{\mathrm{ON}}/G_{\mathrm{OFF}}$. The TFTs in region C feature networks with a probability of percolation through only m-CNTs higher than 1%, i.e., $R^{\mathrm{M}}_{n,L,W} > 1\%$, and therefore the 1st-percentile realization is short-circuited having a very low $G_{\mathrm{ON}}/G_{\mathrm{OFF}}$. The networks operating in D region are not short-circuited but the on/off ratio is low because of high leak-currents in off-state through the high-density m-CNTs. We can conclude that the optimal dimensions of the CNT TFT channel regarding the device switching performance are those outside the regions A, B, C, and D shown in Fig. 4.11. The dotted lines approximate the region where CNT TFTs attain high on-conductance and, at the same time, a high on/off ratio. Therefore, the random CNT TFTs with a channel aspect ratio $L_{\mathrm{CH}}/W_{\mathrm{CH}} < 1.2$ and a normalized size $L_{\mathrm{CH}}W_{\mathrm{CH}}/l^2_{\mathrm{CNT}} > 250$ with a probability higher than 99% exhibit on-conductance higher than 1 μS and, at the same time, an on/off ratio higher than 10^4.

4.4 Comparison of conductance model and experimental results

In this section we compare the results obtained using our conductance model with experimental results from recently published papers of other authors. The experimental results from Ref. [58] (i.e., its Fig. 3) are compared with the results obtained using our conductance model in Fig. 4.12. The parameters of the model are the same as those measured in Ref. [58], i.e., the channel length is $L_{\mathrm{CH}} = 10$ μm, its width is $W_{\mathrm{CH}} = 35$ μm, and the CNT length is $l_{\mathrm{CNT}} = 2.5$ μm. Hence, the normalized length and width of the network are $L = 4$ and $W = 14$, respectively. Since Fig. 3 in [58] shows a gate response of the source-drain current I at applied low voltage $V = 0.1$ V, the conversion to on- and off-conductance is done according to $G = I/V$ for gate voltages equal to -4 V and 6 V, respectively. The values of CNT densities

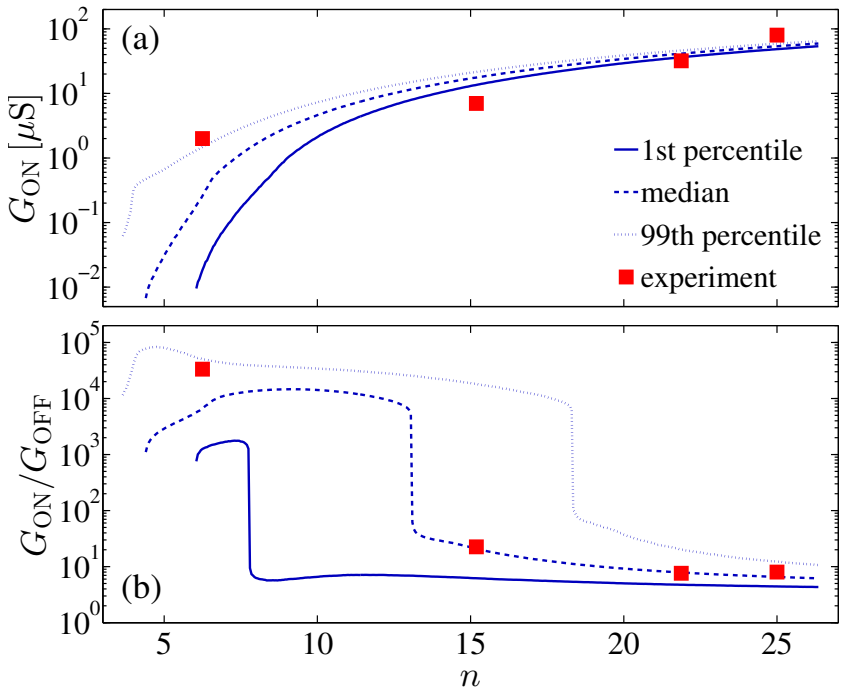

Figure 4.12: On-conductance G_{ON} (a) and on/off ratio G_{ON}/G_{OFF} (b) as a function of the normalized density n. The lines represent results obtained using our conductance model, while the points represent experimental results from Ref. [58] (its Fig. 3). Parameters of the model are the same as those measured in Ref. [58], i.e., the channel length is $L_{CH} = 10$ μm, its width is $W_{CH} = 35$ μm, and the CNT length is $l_{CNT} = 2.5$ μm.

for the experimental points $\rho = 1, 3, 3.5$, and 4.0 μm^{-2} are taken from Ref. [47] and the conversion to the normalized CNT density n is done according to $n = \rho\, l_{CNT}^2$. As can be seen in Fig. 4.12, the excellent agreement is obtained between the experimental points and the results calculated using our conductance model. As expected, the on-conductance G_{ON} increases with the normalized density n, and a sharp drop of on/off ratio G_{ON}/G_{OFF} is obtained at a high density. The experimental values of the on-conductance are high, i.e., higher than 1 μS, since the realized networks present narrow-channel configurations with a low value of the aspect ratio $r = 2/7$, see [126]. As our analytic model, given by Eqs. (2.28) and (4.3)-(4.5), predicts, the probability of short-circuited realization for the last three experimental points, with the density $n > 15$, is higher than 80%, i.e., $R^{M}_{n>15,4,14} > 80\%$, and therefore, a low on/off ratio $G_{ON}/G_{OFF} < 20$ was obtained in the experiment, as can be seen in Fig. 4.12. For the first experimental point ($n \approx 6$), the probability of a short-circuited percolation

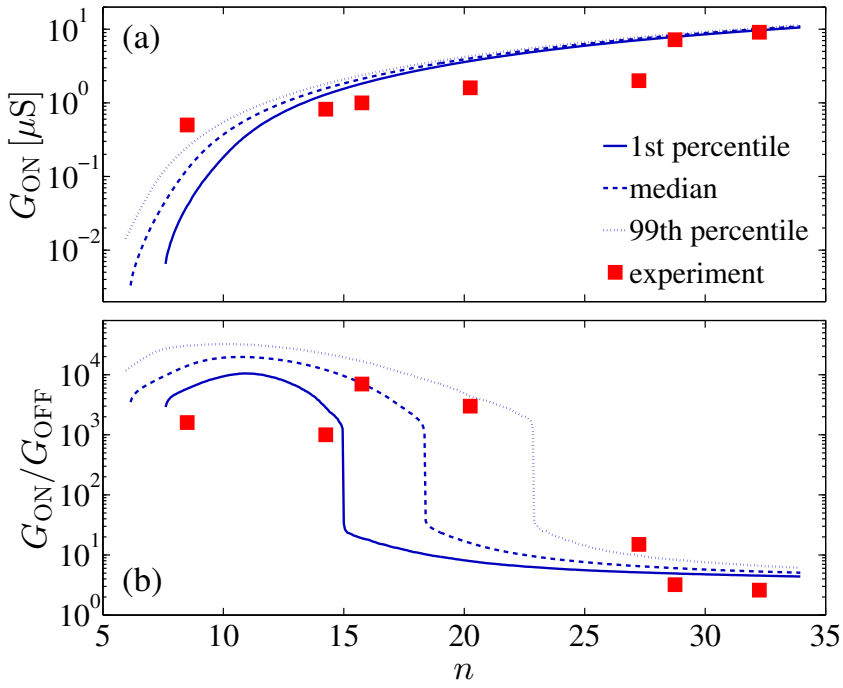

Figure 4.13: On-conductance G_{ON} (a) and on/off ratio G_{ON}/G_{OFF} (b) as a function of the normalized density n. The lines represent results obtained using our conductance model, while the points represent experimental results from Ref. [51] (its Fig. 2(b)). Parameters of the model are the same as those measured in Ref. [51], i.e., the channel length is $L_{CH} = 100$ μm, its width is $W_{CH} = 50$ μm, and the CNT length is $l_{CNT} = 5$ μm.

is low, i.e., $R^{M}_{6,4,14} < 1\%$, and therefore, a high on/off ratio G_{ON}/G_{OFF} was obtained in the experiment. However, high probability of $\overline{SM}$ percolation for the first experimental point, i.e., $R^{\overline{SM}}_{6,4,14} > 60\%$, is a reason for a high variance of on/off ratio, i.e., a lower value of its 1st percentile $G_{ON}/G_{OFF} \sim 10^3$, see Fig. 4.5(d).

The experimental results from Ref. [51] (i.e., its Fig. 2(b)) are compared with the results obtained using our conductance model in Fig. 4.13. The parameters of the model are the same as those measured in Ref. [51], i.e., the channel length is $L_{CH} = 100$ μm, its width is $W_{CH} = 50$ μm, and the CNT length is $l_{CNT} = 5$ μm. Hence, the normalized length and width of the network are $L = 20$ and $W = 10$, respectively. The conversion from the CNT density ρ to the normalized CNT density n is done according to $n = \rho\, l^2_{CNT}$. As can be seen in Fig. 4.13, a good agreement is obtained between the experimental results and the results calculated using our conductance model. As the analytic model predicts (see section 4), the last three

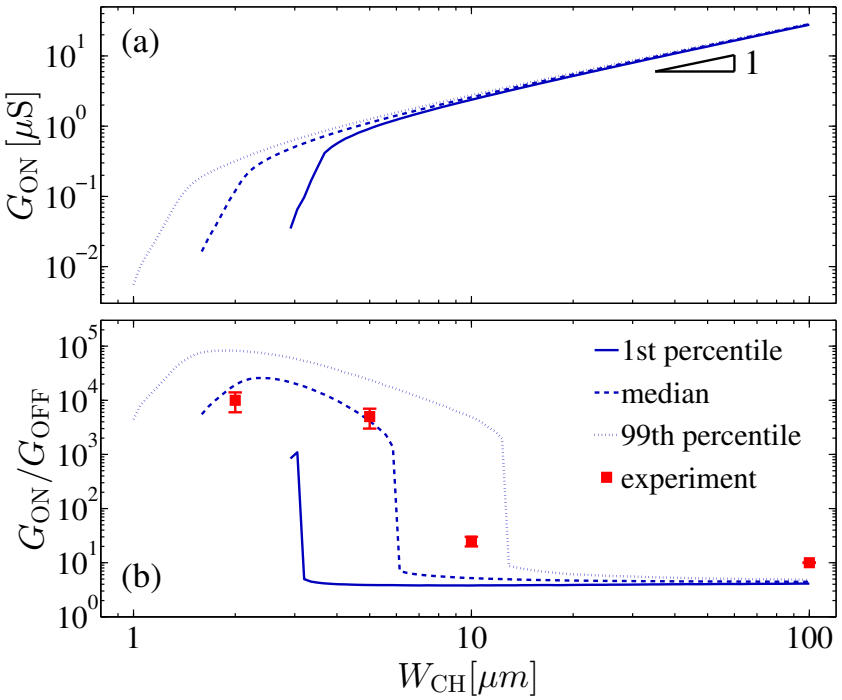

Figure 4.14: On-conductance G_{ON} (a) and on/off ratio G_{ON}/G_{OFF} (b) as a function of the channel width W_{CH}. The lines represent results obtained using our conductance model, while the points represent experimental results from Ref. [34] (its Fig. 2(a)). Parameters of the model are the same as those measured in [34], i.e., the channel length is $L_{CH} = 100$ μm, CNT length is $l_{CNT} = 5$ μm, and the normalized density is $n = 40$.

experimental points, with the density $n > 25$, have the percolation probability of short-circuited realizations $R^{M}_{n>25,20,10}$ higher than 99% and therefore, low on/off ratio $G_{ON}/G_{OFF} < 20$ was obtained, as can be seen in Fig. 4.13. At the same time, the first two experimental results with $n < 15$ have the probability of short-circuited realizations $R^{M}_{n<15,20,10}$ lower than 1% and therefore, a high on/off ratio G_{ON}/G_{OFF} was obtained in the experiment.

Finally, the experimental results from Ref. [34] (i.e., its Fig. 2(a)) are compared with the results obtained using our conductance model in Fig. 4.14. The parameters of the model are the same as those measured in Ref. [34], i.e., the channel length is $L_{CH} = 100$ μm, the CNT length is $l_{CNT} = 5$ μm, and the normalized density is $n = 40$. Hence, the normalized length of the network is $L = 20$. As can be seen in Fig. 4.14, the excellent agreement is obtained between the experimental results and the results calculated using our conductance model. As the analytic

model predicts (see section 4), the last two experimental points with $W_{CH} \geq 10$ μm ($W \geq 2$) have the percolation probability of short-circuited M realizations $R^{M}_{40,20,W\geq 2}$ higher than 95% and, therefore, low on/off ratio $G_{ON}/G_{OFF} < 30$ was obtained in the experiment, as can be seen from Fig. 4.14. For the first experimental point, i.e., $W_{CH} = 2$ μm, the overall percolation probability is lower than 85%, i.e., more than 15% of all realizations are nonconducting. Therefore, this configuration is not applicable for the transistor mass-production because the repeatability and the uniformity of realized devices are uncertain. Even if nonconducting realizations are rejected, the on-conductance of remaining realizations is very low, of the order of 0.1 μS, see Fig. 4.14(a). At the end, we note that our conductance model confirms linear increase of the on-conductance G_{ON} with increasing channel width W_{CH} when $W_{CH} > 20$ μm (i.e., $W > 4$), see Fig. 4.14(a).

4.5 Conclusions

In this Chapter, we present numerical simulation results for the switching performance of transistors based on random networks of as-grown CNTs. The CNT thin films studied here are considered as a suitable material for low-cost, flexible, and transparent field-effect transistors. One factor that makes CNT films complex is that they contain both metallic and semiconducting nanotubes. Only the s-CNTs have highly modulated conductance by the gate and only junctions between CNTs of the same type are highly conductive. Therefore, the random CNT TFTs that percolate only through s-CNT paths can simultaneously attain high on-conductance and a high on/off ratio. As a result, a key limitation in scaling up the production of random CNT TFTs with a high on-current and on/off ratio is a requirement to achieve uniform performance of the realized devices.

We determine the probabilities of different conduction regimes for as-grown CNT networks and derive expressions which represent an excellent fit to the data calculated using numerical simulations. We also show that the fraction of 1:2 of metallic to semiconducting nanotubes provides sufficient design freedom. We avoid creating m-CNT paths, while at the same time determine a density range where the

rate of realizations that percolate only through s-CNT paths is higher than 99%. Since there is a trade-off between the on-conductance and on/off ratio regarding the CNT density, we show that the position of the only s-CNT percolation probability maximum can be used as a good balance for the CNT density value. In the CNT conductance model we have included diffusive electrical transport through CNTs typical for rodlike nanostructures whose length is larger than the mean free path of the electrons. This enables us to consider the influence of the CNT length on the device characteristics. When the CNT length increases, diffusive transport in the CNTs becomes dominant and on-conductance decreases with CNT length. At the same time, because of the increased resistance of m-CNTs, the leak-currents in the off-state through the m-CNTs decrease and the on/off ratio improves. This results in a further trade off, however, the improvement of the on/off ratio is much larger than the detrimental loss of the on-conductance.

Asymmetric systems have lower finite-size scaling exponents than symmetric systems. This results in more pronounced finite-size scaling behavior than in the symmetric case and enables us even more design freedom. We performed a parameter study to find the optimal channel dimensions for CNT TFTs. We present a region of the channel dimension where most of the random CNT realizations have satisfactory transistor performance. According to the criteria of high on-conductance at the same time as a high on/off ratio, within the 99% confidence range, the optimal region of the channel dimensions can be estimated with aspect ratio $L_{\mathrm{CH}}/W_{\mathrm{CH}} < 1.2$ and size $L_{\mathrm{CH}}W_{\mathrm{CH}}/l_{\mathrm{CNT}}^2 > 250$. This conclusion remains valid when the CNT length belongs to the range $l_{\mathrm{CNT}} = 4 - 20$ μm, resulting in an acceptable balance between the on-conductance and on/off performance of the random CNT TFTs. We have also demonstrated that the on-conductance and on/off ratio results obtained using our conductance model show excellent agreement with recently published experimental results. Hence, we conclude that the channel dimensions L_{CH} and W_{CH}, CNT length l_{CNT}, and density n are the only parameters needed for the description and optimization of transport processes in TFTs based on random networks of as-grown CNTs.

Chapter 5 Modeling and optimization of quantum cascade laser characteristics

In recent years the scientific community has witnessed rapid progress in the development of unipolar semiconductor quantum cascade lasers (QCLs) [60, 61, 63–66, 71–74]. In the mid- and far-infrared spectral range, these powerful light sources are particularly appreciated for the wide scope of operating wavelengths which can be achieved by using the same heterostructure material combination. The wavelength tunability is realized by altering the active region design, i.e., modifying the layers' widths and composition [63–65]. The QCL emission is based on intersubband transitions between specific subbands within a multiple quantum well (QW) heterostructure. The typical design of the QCL active region entails a three-level system. An intense magnetic field parallel to the growth direction of semiconductor layers breaks the two-dimensional (2D) in-plane continuous energy spectrum into discrete Landau levels. This results in an increase of otherwise short carrier lifetime (of the order of 1 ps) in the excited state [64–66, 75]. The desired emission wavelength defines the necessary separations between the active laser energy states, while the spacing between the lower laser level and the ground state is set by LO-phonon energy. The lifetime of electrons in the excited laser state is strongly influenced and modulated by the applied magnetic field which results in oscillations in the laser emission intensity. Leuliet *et al.* [66] attributed this effect to two scattering mechanisms:

(1) inelastic scattering by LO-phonons; and

(2) elastic scattering by interface roughness.

Considering that the scattering processes between the two states depend on their energy spacing, certain relaxation mechanisms can be enhanced or inhibited by varying the magnetic field strength, although they may be influenced by the operating tem-

perature as well. Hence, detailed understanding of various scattering mechanisms, relevant for laser operation, may be an important factor in improving its features and represents a key issue in efficient design of QCLs. LO-phonon scattering is well explained in previous theoretical and experimental works [64, 80]. Increasing magnetic field reduces the number of levels under consideration and changes the energy differences between individual levels, thus affecting the lifetime of carriers in higher states. On the other hand, the influence of interface roughness scattering remained less clear. The strength of the interface roughness scattering in a particular sample is determined by the actual morphology of the interfaces. The common description of the effects of interface roughness scattering assumes a Gaussian correlation of interface steps with an average step height and a correlation length [66, 127–130]. In contrast to LO-phonon, interface roughness scattering does not depend on temperature. As a result, efficiency of the interface roughness scattering mechanism is expected to remain constant with increasing temperature, while the efficiency of LO-phonon scattering is reduced due to their higher absorption [81].

In this Chapter we study the electron relaxation rates for the upper state of the laser transition, due to electron–LO-phonon interactions and interface roughness scattering, for a structure subjected to a magnetic field parallel to the confinement direction. The QCL under consideration comprises a triple quantum well (TQW) GaAs/$Al_{0.33}Ga_{0.67}$ and is intended for operation at 11.4 μm. To understand the effects of interface roughness scattering and compare it with LO-phonon scattering, we have studied relaxation times and optical gain for different temperatures and magnetic fields. The electron distribution over the states of the system is found by solving the full set of rate equations that describe the electron transport between levels, and subsequently used to determine the optical gain.

In section 5.1, we present a theoretical description of a realistic QCL active region and introduce models for LO-phonon scattering and interface roughness scattering rate with and without a presence of an external magnetic field. The nonlinear rate equations which describe population change in each Landau level are presented as well. The stationary solution of these equations allows evaluating the degree of population inversion and resulting optical gain. Section 5.2 brings numerical

results of the scattering rates and the total relaxation rate from the upper laser state, for a wide range of magnetic fields 3−60 T and two temperatures $T = 77$ K and 300 K. Using the calculated scattering rates as input data, rate equations are solved and population inversion and the optical gain are obtained. For both the population inversion and the gain, interface roughness scattering is shown to have a significant influence in terms of reducing the predicted magnitude, especially at low temperatures. Finally, in section 5.3 we present an efficient numerical algorithm for optimization of GaAs/AlGaAs quantum cascade laser active region parameters considering the combined action of both studied scattering mechanisms.

5.1 Theoretical considerations

The active region of the QCL structure under consideration comprises three coupled QWs biased by an external electric field E as displayed in Fig. 5.1. In the absence of the magnetic field this system has three energy states, i.e. subbands ($n = 1, 2,$ and 3), and the laser transition occurs between subbands $n = 3$ and $n = 2$. This active region is surrounded by suitable emitter/collector regions in the form of superlattices, designed as Bragg reflectors, which inject electrons into state $n = 3$ on one side, and allow for rapid extraction of carriers from the lowest subband $n = 1$, on the other side. The energy difference between E_2 and E_1 should match the LO-phonon energy in order to ensure fast depopulation via LO-phonon scattering and maintain a short lifetime for the lower laser level. In addition, we introduce in our calculations the interface roughness scattering as additional nonradiative relaxation mechanism. The influences of these two mechanisms are compared in the following section.

The injection of carriers into the active region and extraction from the lower subband is achieved via resonant tunneling. In the absence of an external magnetic field, the electronic subbands from Fig. 5.1 have a free particle-like energy dispersion in the direction parallel to the QW planes $E_n + \hbar^2 k_{||}^2 / 2m_{||n}(E_n)$, where $m_{||n}(E_n)$ is the energy-dependent in-plane effective mass and $k_{||}$ is the in-plane wave vector. However, when this structure is subjected to a strong magnetic field B in the z-

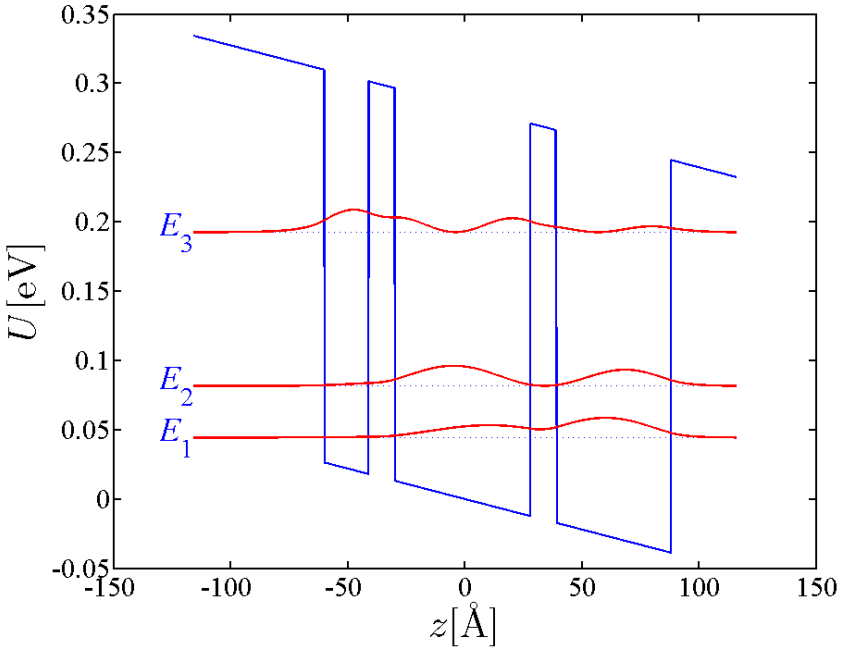

Figure 5.1: The conduction-band diagram of the active region of GaAs/ $Al_{0.33}Ga_{0.67}As$ QCL described in Ref. [64], in an electric field of 44 kVcm^{-1}. The subband positions at zero magnetic fields, together with the corresponding wave functions squared, are also displayed.

direction, continuous subbands transform into series of individual (strictly discrete) states, the total energies of which are [65] $E_{n,l} \approx E_n + (l + 1/2)\hbar\omega_{c_n}$ where $l = 0, 1, 2, ...$ is the Landau index, $E_n \equiv E_n(k_{||} = 0)$, the term $(l + 1/2)\hbar\omega_{c_n}$ originates from the in-plane kinetic energy part of the subband, and $\omega_{c_n} = eB/m_{||n}$ is the corresponding cyclotron frequency. The values of B which give rise to resonant LO-phonon emission are found by solving the equation $E_{3,0} - E_{n,l} = \hbar\omega_{LO}$ where $n = 1, 2$, while $\hbar\omega_{LO}$ is the LO-phonon energy.

According to Refs. [66, 75], to account for the variations of the well widths, a Gaussian probability density is introduced:

$$\Pi(L_i) = \frac{1}{\sigma\sqrt{2\pi}} e^{-(L_i - L_{i0})^2/2\sigma^2} \tag{5.1}$$

for the ith well width L_i, $i = 1, 2, 3$. In order to keep the results as analytical as possible, we assume that around a mean value L_{i0} the energy difference varies

linearly with L_i, i.e.,

$$E_{n_\mathrm{i},l_\mathrm{i}}(L_i) - E_{n_\mathrm{f},l_\mathrm{f}}(L_i) \approx E_{n_\mathrm{i},l_\mathrm{i}}(L_{i0}) - E_{n_\mathrm{f},l_\mathrm{f}}(L_{i0}) - \gamma(L_i - L_{i0}). \tag{5.2}$$

with the factor γ taken the same for all Landau levels, according to [66, 75].

By introducing Eqs. (5.1) and (5.2) into the Fermi golden rule, we obtain the following function:

$$\begin{aligned} J^\mathrm{s} &= \int_{-\infty}^{\infty} \Pi(L_i)\delta[E_{n_\mathrm{i},l_\mathrm{i}} - E_{n_\mathrm{f},l_\mathrm{f}} - \Delta E_\mathrm{s}]dL_i \\ &= \frac{1}{\delta\sqrt{2\pi}} e^{-\left(E_{n_\mathrm{i},l_\mathrm{i}} - E_{n_\mathrm{f},l_\mathrm{f}} - \Delta E_\mathrm{s}\right)^2/2\delta^2}, \end{aligned} \tag{5.3}$$

where $\delta = \sigma\gamma$ is the width of the Gaussian distribution of energy difference $E_{n_\mathrm{i}} - E_{n_\mathrm{f}} + (l_\mathrm{i}\omega_{c_{n_\mathrm{i}}} - l_\mathrm{f}\omega_{c_{n_\mathrm{f}}})\hbar + \hbar(\omega_{c_{n_\mathrm{i}}} - \omega_{c_{n_\mathrm{f}}})/2 - \Delta E_\mathrm{s}$, and "s" denotes the scattering mechanism (electron-LO-phonon scattering (LO) or interface roughness (IR) scattering). In our notation $\Delta E_\mathrm{LO} = \hbar\omega_\mathrm{LO}$ and $\Delta E_\mathrm{IR} = 0$. The terms $E_{n,l}$ represent the total energies of Landau levels and a more detailed explanation of their calculation will be provided in the continuation of this section, see Eq. (5.19).

5.1.1 Electron-LO-phonon scattering in magnetic field

The electron-LO-phonon scattering rates for phonon emission between the initial state $E_{n_\mathrm{i},l_\mathrm{i}}$ and the final state $E_{n_\mathrm{f},l_\mathrm{f}}$ may be found from

$$\frac{1}{\tau^\mathrm{LO}_{(n_\mathrm{i},l_\mathrm{i})\to(n_\mathrm{f},l_\mathrm{f})}} = \frac{2\pi}{\hbar}\sum_{\vec{q}} |\langle n_\mathrm{f}, l_\mathrm{f}, k_{x_\mathrm{f}}, n_q + 1|\hat{H}_{\mathrm{e-ph}}(\vec{q})|n_\mathrm{i}, l_\mathrm{i}, k_{x_\mathrm{i}}, n_q\rangle|^2 J^\mathrm{LO}. \tag{5.4}$$

In this expression, electron-LO-phonon Hamiltonian $\hat{H}_{\mathrm{e-ph}}(\vec{q})$ is the sum of the interaction Hamiltonians with each phonon mode defined by its 3D wave vector $\vec{q}$, see Ref. [75], and k_{x_i} and k_{x_f} are the initial and the final state wave vector components, respectively. From the previous equation one obtains the following

analytical expression for the scattering rate:

$$\frac{1}{\tau^{\mathrm{LO,\{e\}}}_{(n_\mathrm{i},l_\mathrm{i})\to(n_\mathrm{f},l_\mathrm{f})}} = \frac{e^2\omega_\mathrm{LO}}{4\epsilon_0}\left(\frac{1}{\epsilon_\infty}-\frac{1}{\epsilon_\mathrm{s}}\right) \times \frac{1}{\delta\sqrt{2\pi}} e^{-\left(E_{n_\mathrm{i},l_\mathrm{i}}-E_{n_\mathrm{f},l_\mathrm{f}}-\hbar\omega_\mathrm{LO}\right)^2/2\delta^2}(n_q+1) \times \int_0^\infty |F(q_{||})|^2 G(q_{||}) dq_{||}, \tag{5.5}$$

where ϵ_∞ and ϵ_s are the static and the high-frequency relative dielectric constant, respectively, ϵ_0 is the vacuum dielectric permittivity and $n_q = [\exp(\hbar\omega_\mathrm{LO}/k_\mathrm{B}T)-1]^{-1}$ is the mean number of LO-phonons. Furthermore, $q_{||}$ is the in-plane component of the phonon wave vector $\vec{q} = (q_z, q_{||})$ and $F(q_{||})$ is the lateral overlap integral

$$|F(q_{||}, l_\mathrm{i}, l_\mathrm{f})|^2 = e^{-(q_{||}^2/2\beta^2)}\frac{l_\mathrm{i}!}{l_\mathrm{f}!}\left(\frac{q_{||}^2}{2\beta}\right)^{l_\mathrm{f}-l_\mathrm{i}}\left[L_{l_\mathrm{i}}^{l_\mathrm{f}-l_\mathrm{i}}\left(\frac{q_{||}^2}{2\beta}\right)\right]^2, \tag{5.6}$$

where $\beta = \sqrt{eB/\hbar}$ is the magnetic length and $L_m^k(x)$ represents the associate Laguerre polynomial. Finally, $G(q_{||})$ stands for the form factor given by

$$G(q_{||}) = \int\int \eta_\mathrm{i}^*(z)\eta_\mathrm{f}(z)\eta_\mathrm{i}(z')\eta_\mathrm{f}^*(z')e^{-q_{||}|z-z'|}dzdz', \tag{5.7}$$

where η_i and η_f denote the z-dependent parts of the electronic wave functions. The electron-LO-phonon scattering rate for phonon absorption [81] is

$$\frac{1}{\tau^{\mathrm{LO,\{a\}}}_{(n_\mathrm{f},l_\mathrm{f})\to(n_\mathrm{i},l_\mathrm{i})}} = \frac{1}{\tau^{\mathrm{LO,\{e\}}}_{(n_\mathrm{i},l_\mathrm{i})\to(n_\mathrm{f},l_\mathrm{f})}}\frac{1}{e^{\hbar\omega_\mathrm{LO}/kT}}. \tag{5.8}$$

Phonon absorption is significant at room temperature ($T = 300$ K) and it almost vanishes at low temperatures ($T = 77$ K).

5.1.2 Electron-LO-phonon scattering without magnetic field

When the magnetic field is not present, the electron-LO-phonon scattering rate may be evaluated from

$$\frac{1}{\tau^{\mathrm{LO}}_{n_\mathrm{i}\to n_\mathrm{f}}(B=0)} = \frac{2\pi}{\hbar}\sum_{\vec{q}}\left|\langle n_\mathrm{f}, \vec{k}_\mathrm{f}, n_q+1|\hat{H}_\mathrm{e-ph}(\vec{q})|n_\mathrm{i}, \vec{k}_\mathrm{i}, n_q\rangle\right|^2 J^\mathrm{LO}. \tag{5.9}$$

The Hamiltonian $\hat{H}_{\mathrm{e-ph}}$ is in this case the sum of interaction Hamiltonians with each phonon mode defined by its 3D wave vector $\vec{q}$, see Ref. [131], and $\vec{k_{\mathrm{i}}}$ and $\vec{k_{\mathrm{f}}}$ are the initial and the final state in-plane wave vectors, respectively. From the previous equation one obtains the following expression for the scattering rate in the absence of magnetic field:

$$\frac{1}{\tau^{\mathrm{LO}}_{n_{\mathrm{i}}\to n_{\mathrm{f}}}(B=0)} = \frac{e^2\omega_{\mathrm{LO}}m}{4\pi\hbar^2\epsilon_0}\left(\frac{1}{\epsilon_\infty}-\frac{1}{\epsilon_{\mathrm{s}}}\right)(n_q+1)\int_0^\pi \frac{G(q_{||})}{q_{||}}d\theta, \tag{5.10}$$

where $G(q_{||})$ and $q_{||}$ are the form factor and the in-plane component of phonon wave vector, respectively. The form factor is already defined in Eq. (5.7) and $q_{||}^2 = 2m(E_{\mathrm{i}} - E_{\mathrm{f}} - \hbar\omega_{\mathrm{LO}})/\hbar^2$.

5.1.3 Interface roughness scattering in magnetic field

We use the model for interface roughness scattering proposed by Leuliet *et al.* in Ref. [66]. This model assumes the in-plane terasse-like surface defects, as explained in Ref. [132]. In order to evaluate the interface roughness scattering rate, we introduce spatial distribution of roughness which follows the Gaussian correlation function [66, 127–130]:

$$\langle\Delta(\vec{r})\Delta(\vec{r}')\rangle = \Delta^2 e^{-|\vec{r}-\vec{r}'|^2/\Lambda^2}, \tag{5.11}$$

with Δ being the mean height of the roughness and Λ the correlation length. We also introduce the corresponding perturbation Hamiltonian [66],

$$\hat{H}_{\mathrm{IR}} = U_0\delta(z-z_i)\Delta(x,y), \tag{5.12}$$

where U_0 is the barrier height at interface position z_i.

The electron-interface roughness scattering rate can be calculated from:

$$\left\langle \frac{1}{\tau^{\mathrm{IR}}_{(n_{\mathrm{i}},l_{\mathrm{i}})\to(n_{\mathrm{f}},l_{\mathrm{f}})}}(z_i)\right\rangle = \frac{2\pi}{\hbar}\left\langle \sum_{k_{x_{\mathrm{i}}},k_{x_{\mathrm{f}}}} \left\langle |n_{\mathrm{f}},l_{\mathrm{f}},k_{x_{\mathrm{f}}}|\hat{H}_{\mathrm{IR}}|n_{\mathrm{i}},l_{\mathrm{i}},k_{x_{\mathrm{i}}}|^2\right\rangle\right\rangle J^{\mathrm{IR}}. \tag{5.13}$$

In the above expression, the averaging is performed over space (as follows from

Eq. (5.11)), and over the initial state wave vector component k_{x_i}:

$$\left\langle \frac{1}{\tau^{\mathrm{IR}}_{(n_\mathrm{i},l_\mathrm{i})\to(n_\mathrm{f},l_\mathrm{f})}}(z_i) \right\rangle = \frac{\sqrt{2}}{\hbar\delta} e^{-\frac{\left(E_{n_\mathrm{i},l_\mathrm{i}}-E_{n_\mathrm{f},l_\mathrm{f}}\right)^2}{2\delta^2}} |F_\mathrm{if}|^2 \Delta^2 \Lambda\alpha \times \int_{-\infty}^{+\infty} e^{-\frac{(\Delta k_x)^2}{2}\left[\frac{2+\Lambda^2\beta^2}{2\beta^2}\right]} \zeta(\Delta k_x) d(\Delta k_x). \tag{5.14}$$

Here, $\Delta k_x = k_{x_\mathrm{i}} - k_{x_\mathrm{f}}$, $F_\mathrm{if} = U_0 \eta^*_\mathrm{i}(z_i)\eta_\mathrm{f}(z_i)$ and $\alpha = \beta^2/\left(\pi l_\mathrm{f}! l_\mathrm{i}! 2^{l_\mathrm{f}+l_\mathrm{i}}\right)$. The form factor $\zeta(\Delta k_x)$ is given by:

$$\begin{aligned}\zeta(\Delta k_x) = \int\int \exp\left(-\beta^2\left[t^2+(t-\omega)^2\right] - \frac{\omega^2}{\Lambda^2}\right) \\ \times H_{l_\mathrm{i}}\left[\beta t - \frac{\Delta k_x}{2\beta}\right] H_{l_\mathrm{i}}\left[\beta(t-\omega) - \frac{\Delta k_x}{2\beta}\right] \\ \times H_{l_\mathrm{f}}\left[\beta t + \frac{\Delta k_x}{2\beta}\right] H_{l_\mathrm{f}}\left[\beta(t-\omega) + \frac{\Delta k_x}{2\beta}\right] dt dw\end{aligned} \tag{5.15}$$

and H_j is the Hermite polynomial of order j.

5.1.4 Interface roughness scattering without magnetic field

The electron-interface roughness scattering rate can be calculated from:

$$\left\langle \frac{1}{\tau^{\mathrm{IR}}_{n_\mathrm{i}\to n_\mathrm{f}}(B=0)}(z_i) \right\rangle = \frac{2\pi}{\hbar} \left\langle \sum_{\vec{k}_\mathrm{i},\vec{k}_\mathrm{f}} \left\langle |n_\mathrm{f},\vec{k}_\mathrm{f}|\hat{H}_\mathrm{IR}|n_\mathrm{i},\vec{k}_\mathrm{i}|^2 \right\rangle \right\rangle J^{\mathrm{IR}}. \tag{5.16}$$

The Hamiltonian $\hat{H}_\mathrm{IR}$ is the same as in the case with magnetic field, i.e., Eq. (5.12). The averaging is performed over space, and over amplitude of the initial k_i and the final k_f state wavevector. The following expression for interface roughness scattering rate without magnetic field is obtained:

$$\left\langle \frac{1}{\tau^{\mathrm{IR}}_{n_\mathrm{i}\to n_\mathrm{f}}(B=0)}(z_i) \right\rangle = \frac{\sqrt{2\pi}}{4\hbar\delta} e^{-\frac{(\Delta E_\mathrm{if})^2}{2\delta^2}} |F_\mathrm{if}|^2 (\Delta\Lambda)^2 \times \int_0^{+\infty} e^{-\frac{\frac{\hbar^4}{4m^2}}{2\delta^2}x^2 - \left[\frac{\Lambda^2}{4} - \frac{\frac{\hbar^2}{m}\Delta E_\mathrm{if}}{2\delta^2}\right]x} dx, \tag{5.17}$$

where $\Delta E_\mathrm{if} = E_\mathrm{i} - E_\mathrm{f}$ is the energy difference between the initial and the final state.

5.1.5 Rate equations and optical gain

The interface roughness scattering takes place at all surfaces in the system, hence we can write the expression for the total scattering rate of the system using previously derived expressions for the scattering rates in the presence/absence of magnetic field:

$$\frac{1}{\tau} = \frac{1}{\tau^{\mathrm{LO}}} + \sum_{z_i} \left\langle \frac{1}{\tau^{\mathrm{IR}}}(z_i) \right\rangle . \tag{5.18}$$

Finally, if one wants to compare the effects of electron-LO-phonon scattering and electron-interface roughness scattering, two things can be noted: (1) due to the nature of electron-interface roughness interactions, scattering rates for transition from lower to upper and from upper to lower energy level are equal; and (2) the LO-phonon scattering has maximum influence when the energy difference between two states is close to phonon energy, i.e., $\Delta E_{\mathrm{LO}} = \hbar\omega_{\mathrm{LO}}$. On the other hand, the effects of interface roughness are maximal when the energy difference approaches zero. Therefore, the two mechanisms of scatterings are complementary.

When the magnetic field B is applied, continuous subbands E_n transform into discrete Landau levels. The expression for energies $E_{n,l}$ is given by Ekenberg [133] as

$$E_{n,l} = E_n + \left(l + \frac{1}{2}\right) \frac{\hbar e B}{m_{||n}} + \left[\left(8l^2 + 8l + 5\right) \langle \alpha_0 \rangle + \left(l^2 + l + 1\right) \langle \beta_0 \rangle\right] \frac{e^2 B^2}{2\hbar^2}. \tag{5.19}$$

In Eq. (5.19), $m_{||n}$ represents the parallel effective mass of the nth subband in the absence of the magnetic field [133], while α_0 and β_0 are the nonparabolicity parameters.

The optical gain corresponds to transitions $(3, l) \rightarrow (2, l)$ and is given by [80, 134]

$$g_{3\to 2} = \frac{2e^2\pi^2}{\bar{n}\epsilon_0} \frac{d_{3\to 2}^2}{\lambda} \sum_l \delta(E_{3,l} - E_{2,l} - \hbar\omega)(N_{3,l} - N_{2,l}), \tag{5.20}$$

where $\bar{n}$ is the material refractive index, λ and ω denote the wavelength and the frequency of the emitted light, respectively, while $N_{3,l} - N_{2,l}$ represents the degree of population inversion. The Dirac function in the above equation is replaced in

numerical calculations by a Lorentzian with the linewidth parameter Γ as follows

$$\delta(E_{3,l} - E_{2,l} - \hbar\omega) \to \frac{1}{\pi} \frac{\Gamma}{[E_{3,l} - E_{2,l} - \hbar\omega]^2 + \Gamma^2}. \tag{5.21}$$

The energy difference between states is dependent on the Landau index l, $E_{3,l} - E_{2,l} \approx E_3 - E_2 + \left(l + \frac{1}{2}\right) \hbar eB \left(\frac{1}{m_{||3}} - \frac{1}{m_{||2}}\right)$. Therefore, the Dirac function (i.e. the Lorentzian) cannot be put in the front of summation in Eq. (5.20). The transition matrix element is calculated as $d_{3\to2} = \int \eta_3^*(z) z \eta_2(z) dz$, where the wavefunctions η_n are found by solving the Schrödinger equation in the form [133]

$$\frac{d^2}{dz^2}\alpha_0 \frac{d^2\eta_n}{dz^2} - \frac{\hbar^2}{2} \frac{d}{dz} \frac{1}{m} \frac{d\eta_n}{dz} + U(z)\eta_n = E_n \eta_n. \tag{5.22}$$

Here, m represents the effective mass at the conduction-band minimum.

To calculate the optical gain we need to find the inverse population which is the solution of a nonlinear system of rate equations:

$$N_i \sum_{j \neq i} \frac{\bar{f}_j}{\tau_{i\to j}} - \bar{f}_i \sum_{j \neq i} \frac{N_j}{\tau_{j\to i}} + \frac{J_i}{e} = 0, \tag{5.23}$$

where indices $i, j = 1, 2, \ldots$ denote the electronic states sorted by energy and

$$\bar{f}_i = 1 - \frac{\pi\hbar}{eB} N_i \tag{5.24}$$

is the probability that the state i is not occupied according to the Fermi-Dirac distribution. The electrons arrive in the active region by a constant current, and they are injected only into a limited number of Landau levels of the excited laser state, i.e. levels $(3, 0), \ldots, (3, l_{3,\max})$. The injection current can be represented as a sum of all currents J_i which inject electrons into levels $(3, l_3)$, and in a similar manner, the extraction current can be expressed as a sum of all currents J_i which extract the electrons from levels $(1, l_1)$. The energy values of maximal Landau levels for each subband described by $l_{1,\max}, l_{2,\max}$ and $l_{3,\max}$, are taken in this work to be roughly $E_{3,0} + 5k_BT$ and it is reasonable to assume that the levels above are almost empty, see Ref. [80]. The system of nonlinear rate equations (5.23) can be

successively solved by solving the corresponding system of linear equations in each of the successive steps [7, 8]. The CGM explained in Appendix D can be separately applied in each step for solving the obtained systems of linear equations.

In the absence of an external magnetic field, the electronic subbands have free particle-like energy dispersion in the direction parallel to the QW planes, which in the parabolic approximation reads as $E_{||} = \hbar^2 k_{||}^2 / 2m^*$, where m^* is the effective mass and $k_{||}$ is the in-plane wave vector. The non-radiative lifetime for the state $|3, k_{||}\rangle$ is limited by the electron-LO-phonon scattering into the two lower subbands of the active region, and the optical gain may be described by the following expression:

$$g_{3\to2}(B=0) = \frac{e^2\omega}{2\bar{n}\epsilon_0 c}\int_0^{+\infty} F_{3\to2}|d_{3\to2}|^2\delta(E_3 - E_2 - \hbar\omega)d(k_{||}^2), \tag{5.25}$$

where ϵ_0 is the vacuum dielectric permittivity, c is the speed of light in vacuum, $\hbar\omega$ is the photon energy, $F_{3\to2}$ stands for the difference of Fermi-Dirac functions for the initial and the final state, while $d_{i\to f} = \langle\eta_i|z|\eta_f\rangle$ is the transition matrix element, and η_i and η_f denote the z-dependent parts of the wave functions.

5.2 Numerical results

The active region of a QCL based on GaAs/$Al_{0.33}Ga_{0.67}As$ heterostructure, described in [64] and designed to emit radiation at ~ 11.2 μm, is displayed in Fig. 5.1. The layer widths are 56, 19, 11, 58, 11, 49 and 28 Å, going from the emitter towards the collector barrier, and the electric field is 44 kVcm^{-1}. The material parameters for GaAs used in the calculation are $m_{\mathrm{GaAs}} = 0.067m_0$, for AlAs $m_{\mathrm{AlAs}} = 0.15m_0$, and for $Al_{0.33}Ga_{0.67}As$ $m = 0.33m_{\mathrm{AlAs}} + 0.67m_{\mathrm{GaAs}} \approx 0.094m_0$ (m_0 is the free electron mass), $\bar{n} = 0.33$ and the conduction-band discontinuity between GaAs and $Al_{0.33}Ga_{0.67}As$ is $\Delta E_c = 283.4$ meV. In the absence of magnetic field, the three subbands are at energies $E_1 = 44.5$ meV, $E_2 = 81.8$ meV and $E_3 = 192.7$ meV, with the lasing transition energy of $E_3 - E_2 = 110.9$ meV, in full agreement with experimental data [135]. Numerical parameters used in calculations are $\epsilon_\infty = 10.67$, $\epsilon_s = 12.51$, $\hbar\omega_{\mathrm{LO}} = 36.25$ meV, $\delta = 6$ meV, $\Delta = 1.5$ Å, $\Lambda = 60$ Å, and $T = 77$ K and 300 K, see Refs. [66, 75]. The linewidth parameter of Lorentzian given by Eq. (5.21)

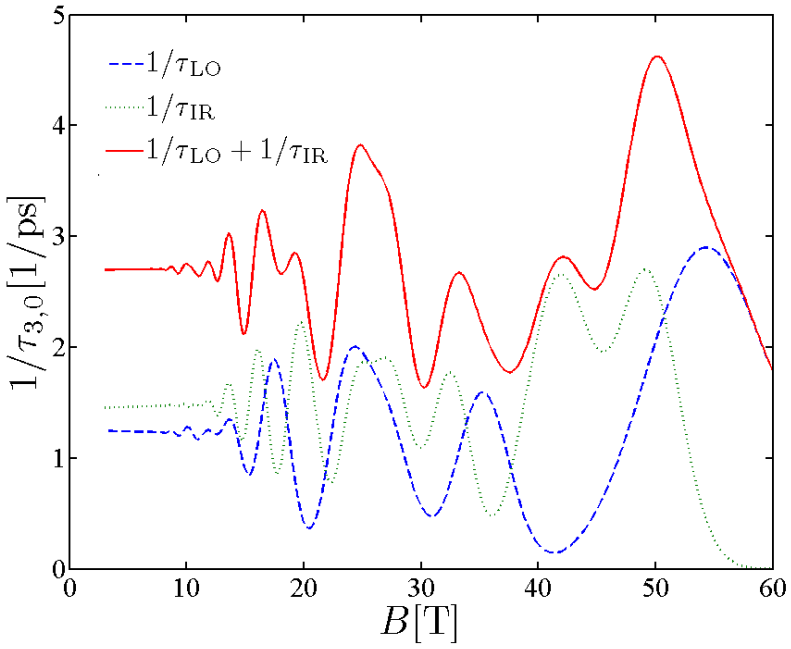

Figure 5.2: The total electron relaxation rate due to the electron LO-phonon scattering and interface roughness scattering for transitions from the ground laser level of the third subband into the two sets of Landau levels of the lower subbands, for magnetic fields in the range of $B = 3-60$ T and at temperature $T = 77$ K.

in the numerical calculations is taken from Ref. [136] as $\Gamma = 4.25$ meV. Nonparabolicity parameters α_0 and β_0 are taken as -2107 eVÅ^4 and -2288 eVÅ^4 for GaAs wells and -1164 eVÅ^4 and -1585 eVÅ^4 for $Al_{0.33}Ga_{0.67}As$ barriers [133].

The scattering rate for the phonon absorption increases exponentially with temperature, see Eq. (5.8). In the following text, we will therefore first present results for the low temperatures ($T = 77$ K) when the phonon absorption is expected to be negligible and thereafter at room temperature ($T = 300$ K) where it is significant.

The total relaxation rate for transitions from the ground Landau level of the third subband (into which the majority of carriers are injected) into the sets of Landau levels of the two other subbands is shown in Fig. 5.2, for the magnetic fields in the range of $B = 3-60$ T and temperature $T = 77$ K. Oscillations of the relaxation rate with B are very pronounced, and very prominent peaks are found at values of the magnetic field which satisfy the resonance conditions for LO-phonon emission. If the relaxation rates due to interface roughness and LO-phonon scattering are

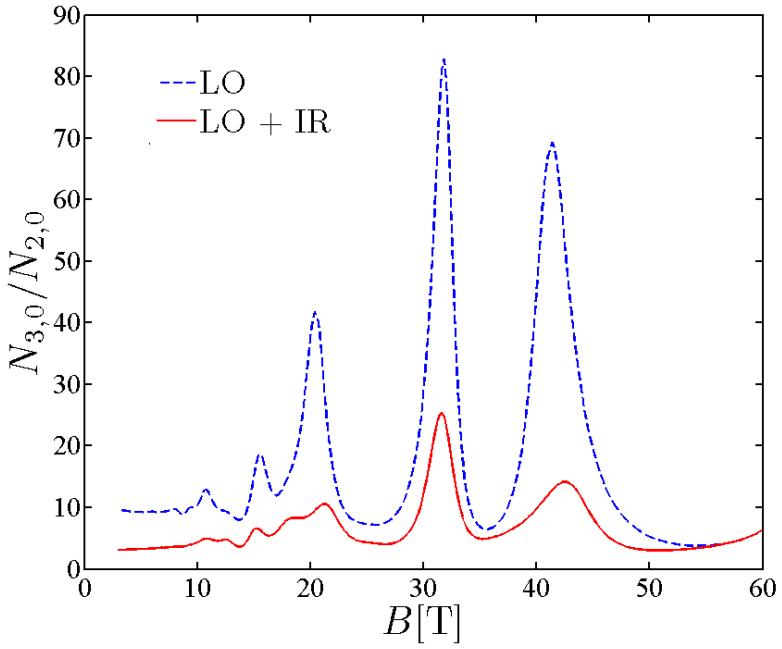

Figure 5.3: The ratio of the total electron areal densities due to the electron LO-phonon and interface roughness scattering, in the ground laser levels of the third and the second subband, as a function of the magnetic field and at temperature $T = 77$ K.

compared, one can see that the local relaxation rate maximum are of the same order of magnitude and not correlated with respect to the applied magnetic field. This is due to the fact that interface roughness scattering has the largest influence when the energy difference between states is diminishing. In contrast, for LO-phonon scattering, when the arrangement of laser levels is such that there is a level situated at $\hbar\omega_{\mathrm{LO}}$ below the state $(3, 0)$, this type of scattering is enhanced. One can also see that the peaks at magnetic fields $B < 20$ T are a result of combined action of two scattering mechanisms. As already pointed out, the interface roughness scattering is enhanced when the energy spacing between levels is vanishingly small, while the LO-phonon scattering rates peak if this spacing is close to phonon energy. For that reason, at magnetic fields below 10 T, when the energy levels become dense, electron relaxation rates due to the interface roughness scattering exceed those of LO-phonon scattering.

Assuming a constant current injection, the modulation of lifetimes of all the states in the system results in either suppression or an enhancement of population

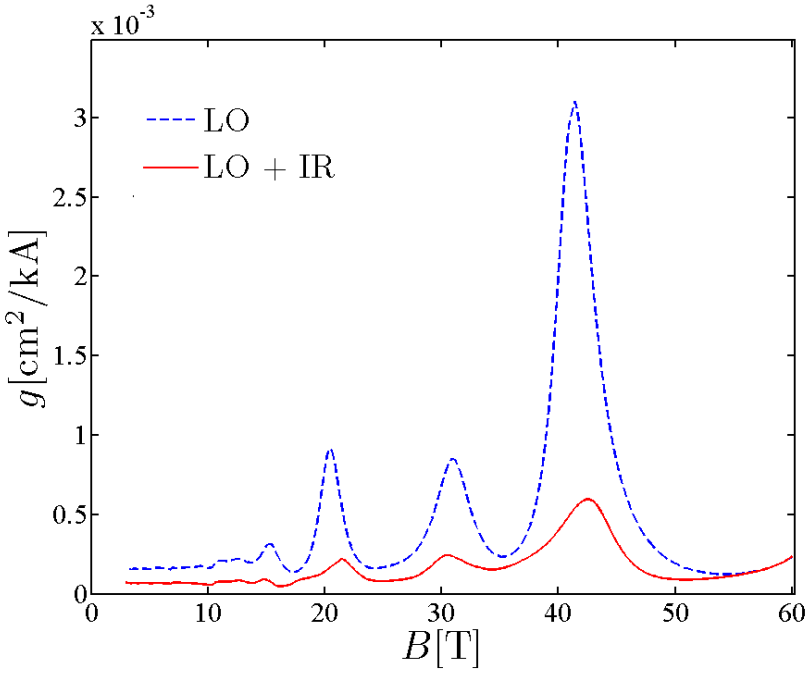

Figure 5.4: The optical gain (per unit injection current) as a function of the applied magnetic field in range $B = 3-60$ T at temperature $T = 77$ K.

inversion between states $(3,0)$ and $(2,0)$, see Fig. 5.3, and therefore in modulation of the optical gain per unit injection current $g = g_{3\to2}/J$ as well, see Fig. 5.4. The first significant minimum of the optical gain is at the magnetic field of $B = 24.2$ T and the positions of relevant states in this case are displayed in Fig. 5.5. Electron relaxation from the state $(3,0)$ is maximized, see Fig. 5.2, because there are two states $(2,2)$ and $(1,3)$ with energies close to $E_{3,0} - \hbar\omega_{\mathrm{LO}}$, together with the state $(1,4)$ very similar to $(3,0)$, and the lifetime for the upper laser state is as low as $\tau_{3,0} = 0.26$ ps. As a result of high relaxation rate, the inverse population is low, see Fig. 5.3.

Quite a different situation occurs at magnetic field around $B = 41.4$ T. The configuration of relevant electronic states, shown in Fig. 5.6, leads to a maximally suppressed LO-phonon relaxation rate from $(3,0)$, because there are no lower states with energy $E_{3,0} - \hbar\omega_{\mathrm{LO}}$ in the proximity, see Fig. 5.6. Still, since the scattering on interface roughness is also present, the maximums of inverse population and optical gain are shifted towards the higher values of the magnetic field ($B = 42.5$ T). The calculated lifetime is $\tau_{3,0} = 0.36$ ps. The most significant effect of the interface

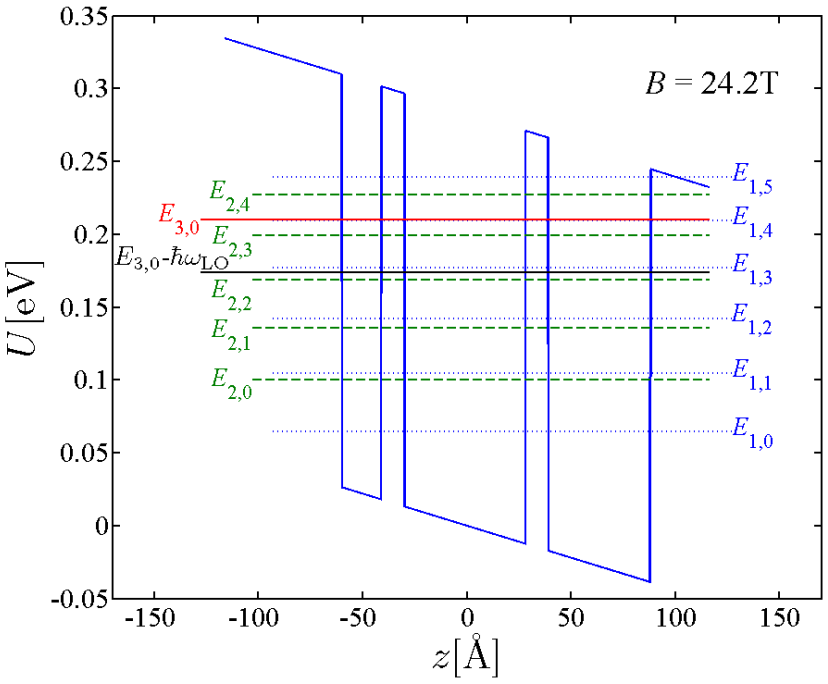

Figure 5.5: Positions of discrete states in the active region for the magnetic field of $B = 24.2$ T, where the optical gain has a local minimum.

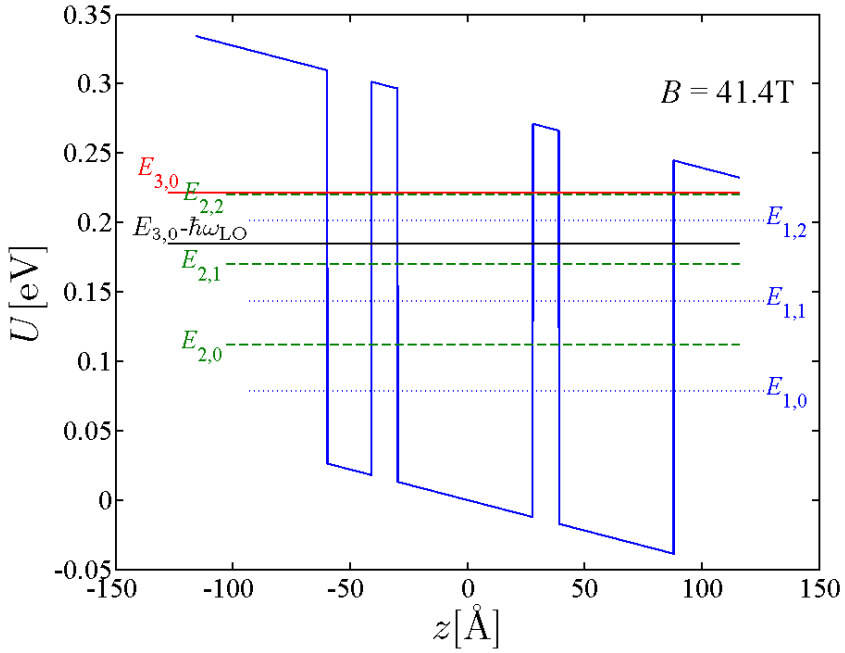

Figure 5.6: Positions of discrete states in the active region for the magnetic field of $B = 41.4$ T, where optical gain has a maximum.

roughness scattering is the reduction in the magnitude of inverse population, which results in reduced optical gain, see Figs. 5.3 and 5.4. Finally, we should note that

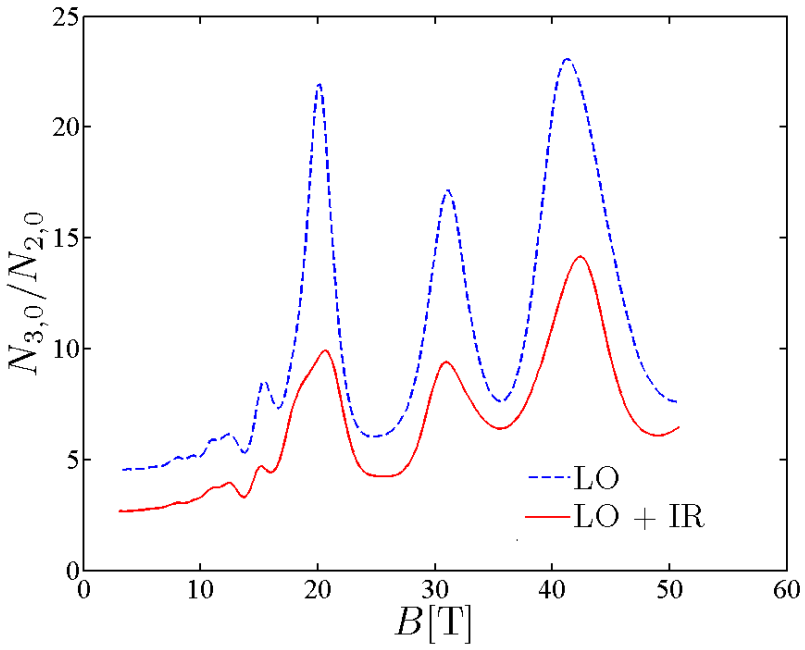

Figure 5.7: The ratio of the total electron areal densities due to the electron LO-phonon and interface roughness scattering, in the ground laser levels of the third and the second subband, as a function of the magnetic field and at temperature $T = 300$ K.

introduction of interface roughness scattering did not create new resonant peaks. It only resulted in relatively small shift ($\sim$1 T) of the existing peaks.

At room temperature $T = 300$ K, the total electron relaxation rate due to the electron LO-phonon scattering is higher ($\sim$1.6 times) than at temperature $T = 77$ K. This increase in relaxation rate is caused by the temperature dependence of the distribution of phonon energies which enters Eq. (5.5). The increase in temperature has a significant effect on the reduction in inversion population due to intensified absorption of LO-phonons, as well as emission, which is evident from Fig. 5.7. At the same time, the scattering on interface roughness is independent of temperature. Consequently, the influence of interface roughness scattering on inversion population is less pronounced at higher temperatures, which can be verified by comparing the results obtained for the optical gain at 300 K, see Fig. 5.8, with the results from Fig. 5.4.

Finally, we should note the QCL operating in the mid-infrared spectral range was chosen to validate our model since experimental data were readily available [64];

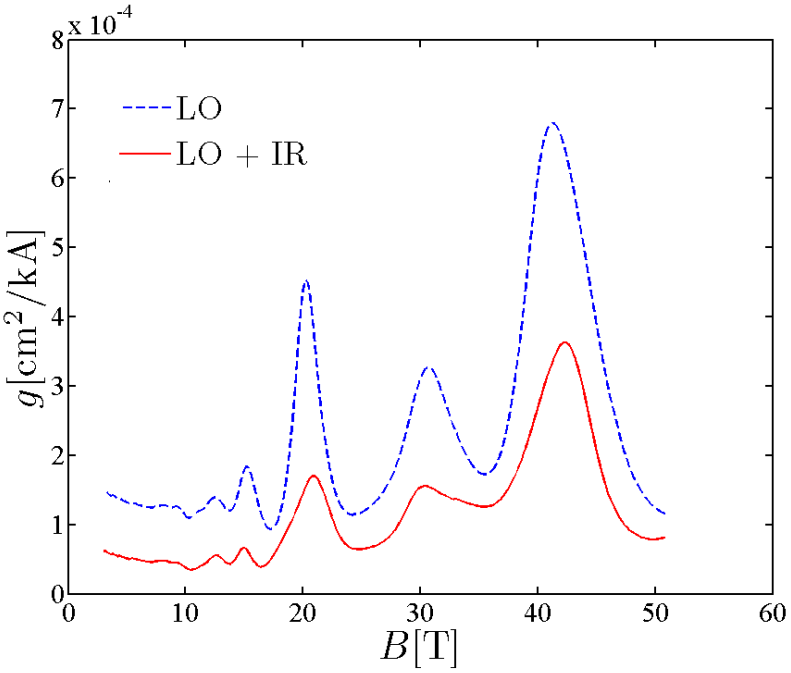

Figure 5.8: The optical gain (per unit injection current) as a function of the applied magnetic field in the range $B = 3-60$ T at temperature $T = 300$ K.

however, the calculations could straightforwardly be modified for the THz spectral range with optimized laser performance at the selected wavelength. The optimization procedure of the QCL active region is described in detail in the next subsection.

5.3 Optimization procedure of the QCL active region

In order to optimize the laser performance at selected wavelength, one must consider the entire free-parameters space and this type of search is best performed by some established method for global optimization, such as simulated annealing algorithm [10] employed in this thesis. This algorithm belongs to the class of stochastic global optimization methods and uses the Metropolis function for the acceptance probability. The annealing algorithm in each step randomly generates new configurations and calculates a fitness function value. Any downhill step is automatically accepted while an uphill step may be accepted according to the Metropolis criteria. The algorithm starts initially with annealing control parameter set to a high value, and as the annealing proceeds, the value of annealing control parameter declines. In

this way, the system is expected to wander initially towards a broad region of the active parameter space containing good solutions and then the search towards minimum is narrowed down. One of the most important phases in the implementation of any simulated annealing algorithm is the selection of a formal fitness function, which should be defined to encompass the goals of optimization. Here, the objective is to optimize the optical gain at selected wavelength, hence the fitness function is taken in the following form [8, 137]

$$F = -\frac{g_{3\to2}(B=0)}{\left[\left(\frac{E_3-E_2}{\hbar\omega}-1\right)^2+\Theta^2\right]\left[\left(\frac{E_2-E_1}{\hbar\omega_{\mathrm{LO}}}-1\right)^2+\Theta^2\right]}, \tag{5.26}$$

where the term in the denominator favours achieving specified emission wavelength (i.e. photon energy $\hbar\omega$) and the LO-phonon resonance. In addition, Θ is a nonzero constant, which ensures that F is strongly driven towards resonance in the course of optimization, while remaining finite at the exact resonance, and $g(B=0)$ is the optical gain in the absence of the magnetic field, given by Eq. (5.25). In numerical calculation, the optical gain can be expressed via the gain coefficient $g^* = (1-\tau_{2\to1}/\tau_{3\to2})\tau_3|d_{3\to2}|^2$, where $\tau_{2\to1}$ and $\tau_{3\to2}$ are the scattering times and τ_3 is the upper laser level lifetime.

5.4 Conclusions

We have set up a rate equation-based model and analyzed the optical gain in the active region of a quantum cascade laser in a magnetic field perpendicular to the structure layers. The magnetic field alters the number of relevant in-plane electronic levels and the corresponding relaxation rates between them, by positioning some states on or off resonance with the upper laser level. In this work, LO-phonon and interface roughness scattering are compared. By examining the model itself, one could note that the interface roughness relaxation has maximal effects when the energy difference between levels is negligible. At the same time, the LO-phonon scattering is enhanced if energy difference is close to resonant phonon energy. From the numerical result it is evident that the inclusion of interface roughness scat-

tering does not introduce additional peaks of inverse population and optical gain with varying magnetic field. However, for magnetic fields smaller then 10 T, when the energy levels become more closely spaced, the electron relaxation rates due to the interface roughness scattering become higher in comparison with LO-phonon relaxation rates. The most prominent effect of the interface roughness scattering is the overall reduction in the inverse population and the optical gain. Obviously, the operating temperature has an additional influence on the balance of the two scattering mechanisms. While the surface roughness scattering does not depend on the temperature, absorption/emission of LO-phonons increases exponentially with temperature. As a consequence, the optical gain resulting from the combined action of these scattering mechanisms is significantly reduced at higher temperatures. Finally, we present an efficient numerical algorithm for optimization of GaAs/AlGaAs quantum cascade laser active region parameters considering the combined action of both studied scattering mechanisms.

Chapter 6 Summary

In this thesis we have proposed different models to describe and optimize effects of structural and geometrical parameters on transport properties of modern nanoelectronic devices, such as transparent conducting nanowire networks, thin-film carbon nanotube transistors, and quantum cascade lasers. At the beginning of Chapter 1 we have presented main results of research in the field of transport processes and main concepts of appropriate statistical methods and models necessary for their understanding. A brief overview of the most important transport processes in each of the considered nanoelectronic devices is presented in the rest of Chapter 1.

In Chapter 2 we have developed an efficient numerical algorithm for the stick-percolation detection. Using this algorithm we have investigated the finite-size scaling effects in percolating widthless stick systems with variable aspect ratios through an extensive Monte Carlo simulation study. A generalized scaling function for rectangular stick systems was introduced to describe the scaling behavior of the first two percolation probability moments. This generalized scaling function, with geometry-dependent prefactors and constant exponents in its expansion, is then used to propose an analytic percolation probability model based on the Gaussian error function.

In Chapter 3 we have developed an efficient numerical algorithm, based on conjugate gradient method, for calculating the electrical conductivity of random nanowire networks. We have proposed a model that explicitly depends on the nanowire density and junction-to-nanowire conductance ratio based on Monte Carlo simulation results. The model describes the transition from the conductivity determined by the structure of a percolating cluster to the conductivity of the dense random nanowire networks. The finite-size scaling effects were also included in the description. Finally, using the proposed model and an analytical approximation for the density-dependent optical transmittance, we have quantified a dependence of the optical

transmittance on the electrical conductivity for the random nanowire networks.

In Chapter 4, the efficient numerical algorithm from Chapter 3 has been adapted for calculating on-conductance and the on/off ratio of random carbon nanotube thin-film transistors. Based on this algorithm we have numerically studied effects of the device parameters (density of carbon nanotubes, channel dimensions and carbon nanotube length) on the electrical transport in order to obtain an optimized and uniform device performance (on-conductance and on/off conductance ratio) without using any post-growth treatment. We have identified the probabilities of different conduction regimes of random carbon nanotube networks using the scaling laws for asymmetric systems of percolating sticks from Chapter 2. Finally, we have demonstrated how geometrical aspects contribute to the feasibility of random carbon nanotube networks as switches with good transistor performance (i.e., high on-current and on/off ratio) and the uniform performance of realized devices.

In Chapter 5, we have presented a detailed theoretical analysis of LO-phonon and interface roughness scattering influence on the operation of GaAs/AlGaAs quantum cascade laser with and without a presence of an external magnetic field. We have demonstrated that the lifetime of the upper state, population inversion and optical gain show strong oscillations as a function of the magnetic field. These oscillations and their magnitude have been found to be a result of the combined action of the two studied mechanisms and strongly affected by temperature. At high temperatures, electrons in the relevant laser states absorb/emit more LO-phonons, which results in reduction in the optical gain. We have shown that the decrease in the optical gain is moderated by the occurrence of interface roughness scattering, which remains unchanged with increasing temperature. Integration of the interface roughness scattering mechanism into the model did not create new resonant peaks in the optical gain. However, it resulted in shifting the existing peaks positions and overall reduction in the optical gain. Finally, we have shown that the optimization of the quantum-cascade-laser performance at a selected wavelength could be performed at entire free-parameters space using simulated annealing algorithm.

Appendix A Analytical derivation of the average stick percolation density and standard deviation

The first percolation moment, i.e., the average stick percolation density, has been already defined as

$$\langle n \rangle_{\mathcal{L},r} = \int_0^\infty n \frac{\partial R_{n,\mathcal{L},r}}{\partial n} dn. \tag{A.1}$$

If we apply integrating by parts, where $u = n$ and $dv = \frac{\partial R_{n,\mathcal{L},r}}{\partial n} dn$, and consequently, $du = dn$ and $v = R_{n,\mathcal{L},r}$, we obtain

$$\langle n \rangle_{\mathcal{L},r} = \lim_{n\to\infty} (n R_{n,\mathcal{L},r}) - \int_0^\infty R_{n,\mathcal{L},r} dn. \tag{A.2}$$

Including expression (2.2) into the previous expression and using one of the fundamental properties of the percolation probability function $\lim_{n\to\infty} R_{n,\mathcal{L},r} = 1$, the previous equation becomes:

$$\langle n \rangle_{\mathcal{L},r} = \frac{1}{\mathcal{L}^2} \lim_{N\to\infty} N - \sum_{N=0}^{\infty} \frac{R_{N,\mathcal{L},r}}{N!} \int_0^\infty (n\mathcal{L}^2)^N e^{-n\mathcal{L}^2} dn. \tag{A.3}$$

Introducing a substitution $\lambda = n\mathcal{L}^2$ and using an identity $\lim_{N\to\infty} N = \sum_{N=0}^{\infty} 1$, we further obtain

$$\langle n \rangle_{\mathcal{L},r} = \frac{1}{\mathcal{L}^2} \sum_{N=0}^{\infty} \left(1 - \frac{R_{N,\mathcal{L},r}}{N!} I_N \right), \tag{A.4}$$

where I_N is an integral

$$I_N = \int_0^\infty \lambda^N e^{-\lambda} d\lambda. \tag{A.5}$$

If we again apply integrating by parts, using now $u = \lambda^N$ and $dv = e^{-\lambda} d\lambda$, and

consequently, $du = N\lambda^{N-1}d\lambda$ and $v = -e^{\lambda}$, a recursive expression is obtained

$$I_N = NI_{N-1}. \tag{A.6}$$

Since $I_0 = 1$, the previous recursive expression becomes

$$I_N = N!. \tag{A.7}$$

Finally, incorporating Eq. (A.7) into Eq. (A.4), the average stick percolation density gets the expected form

$$\langle n \rangle_{\mathcal{L},r} = \frac{1}{\mathcal{L}^2} \sum_{N=0}^{\infty} (1 - R_{N,\mathcal{L},r}). \tag{A.8}$$

The obtained expression allows calculation of the average stick percolation density directly from the discrete percolation probability function $R_{N,\mathcal{L},r}$, which is computationally more efficient, since it avoids using Eq. (A.1) and calculating the continuum percolation probability function $R_{n,\mathcal{L},r}$ with a high resolution.

As already noted, the variance of the percolation probability distribution function can be calculated as $\Delta^2_{\mathcal{L},r} = \langle n^2 \rangle_{\mathcal{L},r} - \langle n \rangle^2_{\mathcal{L},r}$, where

$$\langle n^2 \rangle_{\mathcal{L},r} = \int_0^{\infty} n^2 \frac{\partial R_{n,\mathcal{L},r}}{\partial n} dn. \tag{A.9}$$

If we apply integrating by parts, where $u = n^2$ and $dv = \frac{\partial R_{n,\mathcal{L},r}}{\partial n} dn$, and consequently, $du = 2ndn$ and $v = R_{n,\mathcal{L},r}$, we obtain

$$\langle n^2 \rangle_{\mathcal{L},r} = \lim_{n\to\infty} (n^2 R_{n,\mathcal{L},r}) - 2 \int_0^{\infty} n R_{n,\mathcal{L},r} dn. \tag{A.10}$$

Including expression (2.2) and using the property $\lim_{n\to\infty} R_{n,\mathcal{L},r} = 1$, the previous equation becomes:

$$\langle n^2 \rangle_{\mathcal{L},r} = \frac{1}{\mathcal{L}^4} \lim_{N\to\infty} N^2 - \frac{2}{\mathcal{L}^2} \sum_{N=0}^{\infty} \frac{R_{N,\mathcal{L},r}}{N!} \int_0^{\infty} (n\mathcal{L}^2)^{N+1} e^{-n\mathcal{L}^2} dn. \tag{A.11}$$

Introducing a substitution $\lambda = n\mathcal{L}^2$ and using an identity $\lim_{N\to\infty} N^2 = 2\sum_{N=0}^{\infty}(N+\alpha)$,

where $\alpha \in \mathbb{R}$, we further obtain

$$\langle n^2 \rangle_{\mathcal{L},r} = \frac{2}{\mathcal{L}^4} \sum_{N=0}^{\infty} \left(N + \alpha - \frac{R_{N,\mathcal{L},r}}{N!} I_{N+1} \right), \tag{A.12}$$

where I_{N+1} is an integral

$$I_{N+1} = \int_0^{\infty} \lambda^{N+1} e^{-\lambda} d\lambda. \tag{A.13}$$

Incorporating the previously shown identity $I_{N+1} = (N+1)!$ into Eq. (A.12) we obtain the following expression:

$$\langle n^2 \rangle_{\mathcal{L},r} = \frac{2}{\mathcal{L}^4} \sum_{N=0}^{\infty} \left(N + \alpha - (N+1) R_{N,\mathcal{L},r} \right). \tag{A.14}$$

In order to provide a finite convergence of the previous sum, the real factor α has to be equal to 1, so finally we get

$$\langle n^2 \rangle_{\mathcal{L},r} = \frac{2}{\mathcal{L}^4} \sum_{N=0}^{\infty} (N+1) \left(1 - R_{N,\mathcal{L},r} \right). \tag{A.15}$$

Similar to the previous case, the obtained expression allows calculation of the percolation density variance, and consequently the standard deviation, directly from the discrete percolation probability function $R_{N,\mathcal{L},r}$.

Appendix B Standard errors propagations

The expected statistical error of the discrete percolation probability function $R_{N,\mathcal{L},r}$ is known analytically [98], since each realization of the algorithm gives an independent estimate of $R_{N,\mathcal{L},r}$ which is either 0 or 1 depending on whether or not percolation was occurred in a system with exactly N randomly distributed sticks. If we perform N_{MC} independent realizations, the number of realizations that return 1 is binomially distributed with mean $N_{\mathrm{MC}}R_{N,\mathcal{L},r}$ and variance $N_{\mathrm{MC}}R_{N,\mathcal{L},r}(1-R_{N,\mathcal{L},r})$ [106]. Therefore, our estimate of the standard error of the discrete percolation probability function $R_{N,\mathcal{L},r}$ over N_{MC} realizations is obtained from the simple binomial distribution as

$$\sigma_{R_{N,\mathcal{L},r}} = \sqrt{\frac{R_{N,\mathcal{L},r}(1-R_{N,\mathcal{L},r})}{N_{\mathrm{MC}}}}. \tag{B.1}$$

The standard error of the continuum percolation probability $R_{n,\mathcal{L},r}$ can be estimated applying standard error propagation procedure [106] to the convolution Eq. (2.2) and using the previous standard error estimation of discrete percolation probability:

$$\sigma_{R_{n,\mathcal{L},r}} = e^{-n\mathcal{L}^2}\sqrt{\frac{1}{N_{\mathrm{MC}}}\sum_{N=0}^{\infty}\frac{(n\mathcal{L}^2)^{2N}}{(N!)^2}R_{N,\mathcal{L},r}(1-R_{N,\mathcal{L},r})}. \tag{B.2}$$

Similarly, the standard error of the average stick percolation density $\langle n\rangle_{\mathcal{L},r}$ is estimated from Eqs. (2.3) and (B.1) as

$$\sigma_{\langle n\rangle_{\mathcal{L},r}} = \frac{1}{\mathcal{L}^2}\sqrt{\frac{1}{N_{\mathrm{MC}}}\sum_{N=0}^{\infty}R_{N,\mathcal{L},r}(1-R_{N,\mathcal{L},r})}. \tag{B.3}$$

Finally, the standard error of the percolation density variance $\Delta^2_{\mathcal{L},r}$ is estimated as

$$\sigma_{\Delta^2_{\mathcal{L},r}} = \sqrt{\sigma^2_{\langle n^2\rangle_{\mathcal{L},r}} + 4\langle n\rangle^2_{\mathcal{L},r}\ \sigma^2_{\langle n\rangle_{\mathcal{L},r}}}, \tag{B.4}$$

where $\sigma_{\langle n^2\rangle_{\mathcal{L},r}}$ is obtained from Egs. (2.4) and (B.1) as

$$\sigma_{\langle n^2\rangle_{\mathcal{L},r}} = \frac{2}{\mathcal{L}^4}\sqrt{\frac{1}{N_{\mathrm{MC}}}\sum_{N=0}^{\infty}(N+1)^2 R_{N,\mathcal{L},r}(1-R_{N,\mathcal{L},r})}. \tag{B.5}$$

If the number of independent MC realizations N_{MC} is large enough, the normal distribution can be used as a reasonable approximation of the binomial distribution [106]. Since all analyzed systems in Chapter 2 have more than $N_{\mathrm{MC}} > 10^7$ independent realizations, binomially distributed discrete percolation probability $R_{N,\mathcal{L},r}$ has an approximately normal distribution. For that reason, the standard error of the discrete percolation probability $\sigma_{R_{N,\mathcal{L},r}}$, given by Eq (B.1), actually presents its 68% confidence interval. Therefore, all derived standard errors (B.2)-(B.5) also present 68% confidence intervals for appropriate variables. Finally, standard errors with 95% confidence level, used as the error bars in all figures in Chapter 2, are obtained simply by multiplying the previously given 68% confidence intervals by factor 1.96, see Ref. [106].

We note that all fits in this thesis were done using software package MATLAB R2011b and its built-in least-squares fitting functions. Using appropriate functions for fitting data and the least-squares fitting methods excellent fits were obtained ($R^2 > 0.9999$) in Chapter 2 for all analyzed systems with $\mathcal{L} \geq 16$. All fitting parameters are estimated within 95% confidence level.

Appendix C Calculation of prefactors and exponents of average stick percolation density and standard deviation

In section 2.2, we have analytically shown that the zeroth-order prefactor $a_0(r)$ of the average stick percolation density $\langle n \rangle_{\mathcal{L},r}$ is an odd function on a logarithmic scale, i.e., $a_0(r) = -a_0(1/r)$, while the higher order prefactors $a_i(r)$, where $i \geq 1$, are even functions, i.e., $a_i(r) = a_i(1/r)$. Therefore, the zeroth-order term $\langle n \rangle_{0,\mathcal{L},r}$ of the average stick percolation density $\langle n \rangle_{\mathcal{L},r}$ can be calculated as

$$\langle n \rangle_{0,\mathcal{L},r} = \frac{\langle n \rangle_{\mathcal{L},r} - \langle n \rangle_{\mathcal{L},1/r}}{2}, \tag{C.1}$$

because all higher order terms, expanded applying Eq. (2.20) to $\langle n \rangle_{\mathcal{L},r}$ and $\langle n \rangle_{\mathcal{L},1/r}$, should be mutually canceled, resulting in

$$\langle n \rangle_{0,\mathcal{L},r} = a_0(r)\mathcal{L}^{-1/\nu-\theta_0}. \tag{C.2}$$

Similarly, the first-order term $\langle n \rangle_{1,\mathcal{L},r}$ of the average stick percolation density $\langle n \rangle_{\mathcal{L},r}$ can be approximated as

$$\langle n \rangle_{1,\mathcal{L},r} = \frac{\langle n \rangle_{\mathcal{L},r} + \langle n \rangle_{\mathcal{L},1/r}}{2} - n_{\mathrm{c}}. \tag{C.3}$$

because, in this case, the zeroth-order terms should cancel each other, resulting in

$$\langle n \rangle_{1,\mathcal{L},r} = \mathcal{L}^{-1/\nu} \sum_{i=1}^{\infty} a_i(r)\mathcal{L}^{-\theta_i}. \tag{C.4}$$

For sufficiently large system size $\mathcal{L}$, all higher order terms in the previous expression

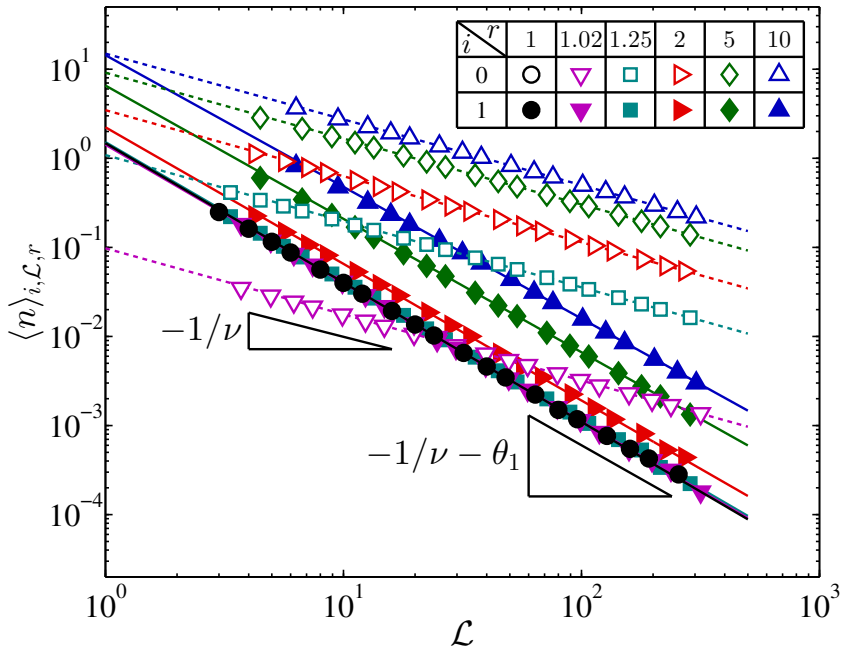

Figure C.1: The zeroth-order $\langle n\rangle_{0,\mathcal{L},r}$ and the first-order term $\langle n\rangle_{1,\mathcal{L},r}$ of average stick percolation density $\langle n\rangle_{\mathcal{L},r}$ plotted as functions of the system size $\mathcal{L}$ for different aspect ratios $r = 1, 1.02, 1.25, 2, 5$, and 10. The points for $\langle n\rangle_{0,\mathcal{L},r}$ (transparent) and $\langle n\rangle_{1,\mathcal{L},r}$ (filled) are obtained from MC simulations and calculated from Eqs. (C.1) and (C.3), respectively. The lines (dashed for $\langle n\rangle_{0,\mathcal{L},r}$ and solid for $\langle n\rangle_{1,\mathcal{L},r}$) are obtained using the least-squares fitting methods. The data are shown on a logarithmic scale to demonstrate power-law convergences of $\langle n\rangle_{0,\mathcal{L},r}$ and $\langle n\rangle_{1,\mathcal{L},r}$ with slopes $-1/\nu$ and $-1/\nu-\theta_1$, respectively.

can be neglected and $\langle n\rangle_{1,\mathcal{L},r}$ can be approximated only by the first-order term

$$\langle n\rangle_{1,\mathcal{L},r} \approx a_1(r)\mathcal{L}^{-1/\nu-\theta_1}. \tag{C.5}$$

The zeroth-order $\langle n\rangle_{0,\mathcal{L},r}$ and the first-order term $\langle n\rangle_{1,\mathcal{L},r}$, obtained from MC simulations and calculated using Eqs. (C.1) and (C.3), respectively, are shown in Fig. C.1 as functions of the normalized system size $\mathcal{L}$ for different aspect ratio r. The points are plotted on a logarithmic scale to demonstrate the power-low dependences assumed by Eqs. (C.2) and (C.5), respectively. When the aspect ratio r is fixed, the zeroth-order terms $\langle n\rangle_{0,\mathcal{L},r}$ fall on a straight line with the same slope $-1/\nu-\theta_0$ for all r, where $\theta_0 = 0$, as shown in Fig. C.1. Similarly, the first-order terms $\langle n\rangle_{1,\mathcal{L},r}$ also fall on straight lines, but with the slope $-1/\nu-\theta_1$, where $\theta_1 = 0.82(2)$. At the

same time, the obtained values of the exponents of $\langle n \rangle_{0,\mathcal{L},r}$ and $\langle n \rangle_{1,\mathcal{L},r}$ confirm the parity assumptions for prefactors $a_i(r)$ and $a_0(r)$, respectively. The prefactors $a_0(r)$ and $a_1(r)$ for systems with $r \geq 1$ are determined as y-axis intercepts in Fig. C.1, while the values for systems with $r < 1$ are obtained using the previously confirmed parity conditions, i.e., $a_0(r) = -a_0(1/r)$ and $a_1(r) = a_1(1/r)$.

In analogy to the previous case, the zeroth-order term $\Delta^2_{0,\mathcal{L},r}$ of the stick percolation density variance $\Delta^2_{\mathcal{L},r}$ can be calculated as

$$\Delta^2_{0,\mathcal{L},r} = \frac{\Delta^2_{\mathcal{L},r} + \Delta^2_{\mathcal{L},1/r}}{2}. \tag{C.6}$$

because the parity of prefactors $b_0(r) = b_0(1/r)$ and $b_i(r) = -b_i(1/r)$, where $i \geq 1$, implies that all higher order terms, expanded applying Eq. (2.21) to the previous expression, should be mutually canceled, resulting in

$$\Delta^2_{0,\mathcal{L},r} = b_0(r)\mathcal{L}^{-2/\nu-\theta_0}. \tag{C.7}$$

Similarly, the first-order term $\Delta^2_{1,\mathcal{L},r}$ of the stick percolation density variance $\Delta^2_{\mathcal{L},r}$ can be determined as

$$\Delta^2_{1,\mathcal{L},r} = \frac{\Delta^2_{\mathcal{L},r} - \Delta^2_{\mathcal{L},1/r}}{2}, \tag{C.8}$$

because for sufficiently large system size $\mathcal{L}$, all higher order terms in the previous expression can be neglected and $\Delta^2_{1,\mathcal{L},r}$ can be approximated by the first-order term

$$\Delta^2_{1,\mathcal{L},r} \approx b_1(r)\mathcal{L}^{-2/\nu-\theta_1}. \tag{C.9}$$

The zeroth-order $\Delta^2_{0,\mathcal{L},r}$ and the first-order term $\Delta^2_{1,\mathcal{L},r}$, obtained from MC simulations and calculated using Eqs. (C.6) and (C.8), respectively, are shown in Fig. C.2 as functions of the normalized system size $\mathcal{L}$ for different aspect ratio r. The points are plotted on a logarithmic scale to demonstrate the power-low dependences assumed by Eqs. (C.7) and (C.9), respectively. When the aspect ratio r is fixed, the zeroth-order terms $\Delta^2_{0,\mathcal{L},r}$ fall on a straight line with the same slope $-2/\nu - \theta_0$ for all r, where $\theta_0 = 0$, as shown in Fig. C.2. Similarly, the first-order terms $\Delta^2_{1,\mathcal{L},r}$ also fall on straight lines, but with the slope $-2/\nu - \theta_1$, where $\theta_1 = 0.82(2)$. At the same

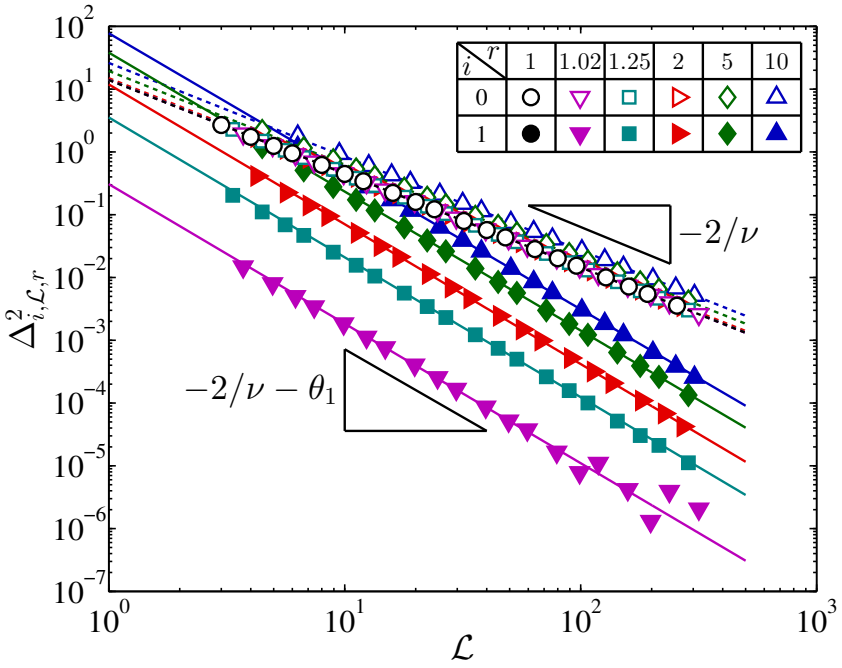

Figure C.2: The zeroth-order $\Delta^2_{0,\mathcal{L},r}$ and the first-order term $\Delta^2_{1,\mathcal{L},r}$ of the stick percolation density variance $\Delta^2_{\mathcal{L},r}$ plotted as functions of the system size $\mathcal{L}$ for different aspect ratios $r = 1, 1.02, 1.25, 2, 5$, and 10. The points for $\Delta^2_{0,\mathcal{L},r}$ (transparent) and $\Delta^2_{1,\mathcal{L},r}$ (filled) are obtained from MC simulations and calculated using Eqs. (C.1) and (C.3), respectively. The lines (dashed for $\Delta^2_{0,\mathcal{L},r}$ and solid for $\Delta^2_{1,\mathcal{L},r}$) are obtained using the least-squares fitting methods. The data are shown on a logarithmic scale to demonstrate power-law convergences of $\Delta^2_{0,\mathcal{L},r}$ and $\Delta^2_{1,\mathcal{L},r}$ with slopes $-2/\nu$ and $-2/\nu - \theta_1$, respectively.

time, the obtained values of the exponents of $\Delta^2_{0,\mathcal{L},r}$ and $\Delta^2_{1,\mathcal{L},r}$ in Fig. C.2 confirm the parity assumptions for prefactors $b_i(r)$ and $b_0(r)$, respectively. The prefactors $b_0(r)$ and $b_1(r)$ for $r \geq 1$ are determined as y-axis intercepts in Fig. C.2, while the values for $r < 1$ are obtained using the previously confirmed parity conditions, i.e., $b_0(r) = b_0(1/r)$ and $b_1(r) = -b_1(1/r)$.

Appendix D Conjugate gradient method

The Conjugate Gradient Method (CGM) is an iterative method for solving a sparse system of linear equations given by the following matrix equation

$$Ax = b, \tag{D.1}$$

where $A \in \mathbb{R}^{n \times n}$ is a known, square, symmetric, positive-definite matrix, $x \in \mathbb{R}^{n \times 1}$ is an unknown vector, and $b \in \mathbb{R}^{n \times 1}$ is a known vector. We note that, a matrix A is positive-definite if, for every non-zero vector z, is satisfied

$$z^{\mathrm{T}} A z > 0. \tag{D.2}$$

In order to demonstrate the basic concepts of CGM, we introduce a quadratic form, that is simply a scalar, i.e., quadratic function of a vector, given by

$$f(x) = \frac{1}{2} x^{\mathrm{T}} A x - b^{\mathrm{T}} x, \tag{D.3}$$

where A is a square matrix and x and b are column vectors. The quadratic form is minimized when its gradient

$$\nabla f(x) = \frac{1}{2} A^{\mathrm{T}} x + \frac{1}{2} A x - b, \tag{D.4}$$

is equal to zero and, at the same time, the matrix A is positive-definite [9, 107]. If the matrix A is symmetric, i.e., $A = A^{\mathrm{T}}$, this equation reduces to

$$\nabla f(x) = Ax - b. \tag{D.5}$$

Setting this gradient to zero, we obtain Eq. (D.1), i.e., the linear system we wish

to solve. Therefore, the solution to $Ax = b$ is a critical point of the quadratic form $f(x)$. If A is positive-definite matrix, as well as symmetric, then this solution is a minimum of the quadratic form $f(x)$, so $Ax = b$ can be solved by finding an vector x that minimizes the quadratic form $f(x)$ given by Eq. (D.3).

The minimization of the quadratic form $f(x)$ is carried out by generating a succession of search directions p_k and improved minimizers x_k. At each iteration a quantity α_k is found that minimizes $f(x_k + \alpha_k p_k)$, and x_{k+1} is set equal to the new point $x_k + \alpha_k p_k$. Also, the residual vector r_{k+1} is iteratively determined at each step as $r_k - \alpha_k A p_k$. The p_k and x_k are built up in such a way that x_{k+1} is also the minimizer of $f(x)$ over the whole vector space of directions already taken, $\{p_1, p_2, ..., p_k\}$. After some number of iterations the system converges to the minimizer over the entire vector space, i.e., to the solution to Eq. (D.1).

The described algorithm converges faster, i.e. in fewer steps, if a preconditioner matrix M is used. The simplest preconditioner is a diagonal matrix whose diagonal entries are identical to those of the system matrix A. Since a diagonal matrix is trivial to invert, this preconditioner can be easy numerically implemented. The process of applying this preconditioner, known as diagonal preconditioning or Jacobi preconditioning, is equivalent to scaling the quadratic form along the coordinate axes. Therefore, the size of quantity α_k at each iteration using Jacobi preconditioner can be calculated as in Refs. [9, 107]

$$\alpha_k = \frac{r_k^{\mathrm{T}} M^{-1} r_k}{p_k^{\mathrm{T}} A p_k}, \tag{D.6}$$

and the direction vector p_{k+1} can be iteratively obtained as

$$p_{k+1} = M^{-1} r_{k+1} + \frac{r_{k+1}^T M^{-1} r_{k+1}}{r_k^T M^{-1} r_k} p_k. \tag{D.7}$$

As one can see from Eqs. (D.6) and (D.7), the dominant operation during an iteration is the matrix-vector product Ap_k. Matrix-vector products generally requires $\mathcal{O}(m)$ operations, where m is the number of non-zero elements in the matrix A. In this thesis all analyzed system matrices A are sparse and, therefore, the matrix-vector products have a time complexity of $\mathcal{O}(n)$. On the other hand, the minimum

number of iterations needed to achieve required error tolerance using CGM for two-dimensional problems is $\mathcal{O}(n^{1/2})$, see Ref. [107]. Therefore, a numerical realization of the CGM algorithm has the total time complexity of $\mathcal{O}(n^{3/2})$.

We also note that the CGM can be used to solve systems where the matrix A is not symmetric, not positive-definite, and even not square. In that case instead of Eq. (D.1) we should consider the following expression: $A^{\mathrm{T}}Ax = A^{\mathrm{T}}b$. Now, the new system matrix $A^{\mathrm{T}}A$ is square, symmetric, and positive-definite, because for any non-zero vector x is satisfied $x^{\mathrm{T}}A^{\mathrm{T}}Ax = ||Ax||^2 > 0$. The only difficulty is that the condition number of created matrix $A^{\mathrm{T}}A$ is the square of that of matrix A, so the overall convergence is significantly slower.

Bibliography

[1] M. Sahimi, *Heterogeneous Materials I: Linear Transport and Optical Properties*, Springer-Verlag, New York (2003). 1, 5

[2] D. Stauffer and A. Aharony, *Introduction to Percolation Theory*, 2nd revised ed., Taylor and Francis, London (2003). 1, 4, 11, 21, 23, 34, 48, 49, 51

[3] M. Plischke and B. Bergersen, *Equilibrium Statistical Physics*, 3rd ed., World Scientific, Singapore (2005). 1, 25

[4] M. Žeželj, I. Stanković, and A. Belić, Finite-size scaling in asymmetric systems of percolating sticks, *Phys. Rev. E* **85**, 021101 (2012). 1, 13, 27, 41, 48, 58

[5] M. Žeželj and I. Stanković, From percolating to dense random stick networks: Conductivity model investigation, *Phys. Rev. B* **86**, 134202 (2012). 1, 58

[6] M. Žeželj and I. Stanković, Random networks of carbon nanotubes optimized for transistor mass-production: Searching for ultimate performance, *Semicond. Sci. Technol.* **31**, 105015 (2016). 1, 57, 58

[7] M. Žeželj, V. Milanović, J. Radovanović, and I. Stanković, Influence of interface roughness scattering on output characteristics of GaAs/AlGaAs quantum cascade laser in a magnetic field, *J. Phys. D: Appl. Phys.* **44**, 325105 (2011). 1, 10, 93

[8] J. Smiljanić, M. Žeželj, V. Milanović, J. Radovanović, and I. Stanković, MATLAB-based program for optimization of quantum cascade laser active region parameters and calculation of output characteristics in magnetic field, *Comput. Phys. Commun.* **185**, 998 (2014). 1, 10, 93, 100

[9] W. H. Press, S. A. Teukolsky, W. T. Vetterling, and B. P. Flannery, *Numerical Recipes in C: The Art of Scientific Computing*, 2nd ed., Cambridge University Press, United States (1992). 1, 113, 114

[10] S. Kirkpatrick, C. D. Gelatt, and M. P. Vecchi, Optimization by simulated annealing, *Science* **220**, 671 (1983). 2, 99

[11] J. Li and G. P. Pandey, Advanced physical chemistry of carbon nanotubes, *Annu. Rev. Phys. Chem.* **66**, 331 (2015). 2, 6, 61

[12] S. Sorel, P. E. Lyons, S. De, J. C. Dickerson, and J. N. Coleman, The dependence of the optoelectrical properties of silver nanowire networks on nanowire length and diameter, *Nanotechnology* **23**, 185201 (2012). 2, 4, 55

[13] S. M. Bergin, Y.-H. Chen, A. R. Rathmell, P. Charbonneau, Z.-Y. Lib, and B. J. Wiley, The effect of nanowire length and diameter on the properties of transparent, conducting nanowire films, *Nanoscale* **4**, 1996 (2012). 4, 53, 54, 55

[14] D. Langley, G. Giusti, C. Mayousse, C. Celle, D. Bellet, and J.-P. Simonato, Flexible transparent conductive materials based on silver nanowire networks: A review, *Nanotechnology* **24**, 452001 (2013). 4, 53

[15] C. Gomes da Rocha, H. G. Manning, C. O'Callaghan, C. Ritter, A. T. Bellew, J. J. Boland, and M. S. Ferreira, Ultimate conductivity performance in metallic nanowire networks, *Nanoscale* **7**, 13011 (2015). 4, 36

[16] A. Kim, Y. Won, K. Woo, C.-H. Kim, and J. Moon, Highly transparent low resistance ZnO/Ag nanowire/ZnO composite electrode for thin film solar cells, *ACS Nano* **7**, 1081 (2013). 4

[17] Y.-J. Choi, I.-S. Hwang, J.-G. Park, K. J. Choi, J.-H. Park, and J.-H. Lee, Novel fabrication of an SnO_2 nanowire gas sensor with high sensitivity, *Nanotechnology* **9**, 095508 (2008). 4

[18] A. R. Madaria, A. Kumar, F. N. Ishikawa, and C. Zhou, Uniform, highly conductive, and patterned transparent films of a percolating silver nanowire network on rigid and flexible substrates using a dry transfer technique, *Nano Res.* **3**, 564 (2010). 4, 5, 34

[19] L. Hu, H. S. Kim, J.-Y. Lee, P. Peumans, and Y. Cui, Scalable coating and properties of transparent, flexible, silver nanowire electrodes, *ACS Nano* **4**, 2955 (2010). 4

[20] P. N. Nirmalraj, A. T. Bellew, A. P. Bell, J. A. Fairfield, E. K. McCarthy, C. O'Kelly, L. F. C. Pereira, S. Sorel, D. Morosan, J. N. Coleman, M. S. Ferreira, and J. J. Boland, Manipulating connectivity and electrical conductivity in metallic nanowire networks, *Nano Lett.* **12**, 5966 (2012). 4

[21] R. M. Mutiso, M. C. Sherrott, A. R. Rathmell, B. J. Wiley, and K. I. Winey, Integrating simulations and experiments to predict sheet resistance and optical transmittance in nanowire films for transparent conductors, *ACS Nano* **7**, 7654 (2013). 4, 36, 41, 53, 54, 55

[22] D. P. Langley, G. Giusti, M. Lagrange, R. Collins, C. Jiménez, Y. Bréchet, and D. Bellet, Silver nanowire networks: Physical properties and potential integration in solar cells, *Sol. Energy Mater. Sol. Cells* **125**, 318 (2014). 4, 41, 53

[23] L. J. Andrés, M. F. Menéndez, D. Gómez, A. L. Martinez, N. Bristow, J. P. Kettle, A. Menéndez, and B. Ruiz, Rapid synthesis of ultra-long silver nanowires for tailor-made transparent conductive electrodes: Proof of concept in organic solar cells, *Nanotechnology* **26**, 265201 (2015). 4, 53, 54, 55

[24] C. O'Callaghan, C. Gomes da Rocha, H. G. Manning, J. J. Boland, and M. S. Ferreira, Effective medium theory for the conductivity of disordered metallic nanowire networks, *Phys. Chem. Chem. Phys.* **18**, 27564 (2016). 4, 34

[25] S. I. White, R. M. Mutiso, P. M. Vora, D. Jahnke, S. Hsu, J. M. Kikkawa, J. Li, J. E. Fischer, and K. I. Winey, Electrical percolation behavior in silver

nanowire–polystyrene composites: Simulation and experiment, *Adv. Funct. Mater.* **20**, 2709 (2010). 4

[26] I. Balberg, N. Binenbaum, and C. H. Anderson, Critical behavior of the two-dimensional sticks system, *Phys. Rev. Lett.* **51**, 1605 (1983). 4, 11

[27] R. Ramasubramaniam, J. Chen, and H. Liu, Homogeneous carbon nanotube/ polymer composites for electrical applications, *Appl. Phys. Lett.* **83**, 2928 (2003). 4, 11, 42

[28] L. Hu, D. S. Hecht, and G. Grüner, Percolation in transparent and conducting carbon nanotube networks, *Nano Lett.* **4**, 2513 (2004). 4, 5, 11, 34

[29] H. E. Unalan, G. Fanchini, A. Kanwal, A. D. Pasquier, and M. Chhowalla, Design criteria for transparent single-wall carbon nanotube thin-film transistors, *Nano Letters* **6**, 677 (2006). 4, 5, 34

[30] I. Balberg, D. Azulay, Y. Goldstein, and J. Jedrzejewski, Possible origin of the smaller-than-universal percolation-conductivity exponent in the continuum, *Phys. Rev. E* **93**, 062132 (2016). 5, 34

[31] P. Keblinski and F. Cleri, Contact resistance in percolating networks, *Phys. Rev. B* **69**, 184201 (2004). 5, 42, 46

[32] Y. Hazama, N. Ainoya, J. Nakamura, and A. Natori, Conductivity and dielectric constant of nanotube/polymer composites, *Phys. Rev. B* **82**, 045204 (2010). 5, 11, 42

[33] J. Li and S.-L. Zhang, Conductivity exponents in stick percolation, *Phys. Rev. E* **81**, 021120 (2010). 5, 35, 36, 40, 42

[34] Q. Cao, H.-S. Kim, N. Pimparkar, J. P. Kulkarni, C. Wang, M. Shim, K. Roy, M. A. Alam, and J. A. Rogers, Medium-scale carbon nanotube thin-film integrated circuits on flexible plastic substrates, *Nature (London)* **454**, 495 (2008). 6, 7, 11, 60, 80

[35] M. F. L. De Volder, S. H. Tawfick, R. H. Baughman, and A. J. Hart, Carbon nanotubes: Present and future commercial applications, *Science* **339**, 535 (2013). 6

[36] A. Abdelhalim, A. Abdellah, G. Scarpa, and P. Lugli, Metallic nanoparticles functionalizing carbon nanotube networks for gas sensing applications, *Nanotechnology* **25**, 055208 (2014). 6

[37] A. D. Bartolomeo, M. Rinzan, A. K. Boyd, Y. Yang, L. Guadagno, F. Giubileo, and P. Barbara, Electrical properties and memory effects of field-effect transistors from networks of single- and double-walled carbon nanotubes, *Nanotechnology* **21**, 115204 (2010). 6, 7

[38] M. Engel, J. P. Small, M. Steiner, M. Freitag, A. A. Green, M. C. Hersam, and P. Avouris, Thin film nanotube transistors based on self-assembled, aligned, semiconducting carbon nanotube arrays, *ACS Nano* **2**, 2445 (2008). 6

[39] D.-M. Sun, M. Y. Timmermans, Y. Tian, A. G. Nasibulin, E. I. Kauppinen, S. Kishimoto, T. Mizutani, and Y. Ohno, Flexible high-performance carbon nanotube integrated circuits, *Nat. Nanotechnol.* **6**, 156 (2011). 6, 72

[40] B. Chandra, H. Park, A. Maarouf, G. J. Martyna, and G. S. Tulevski, Carbon nanotube thin film transistors on flexible substrates, *Appl. Phys. Lett.* **99**, 072110 (2011). 6

[41] C. Wang, J.-C. Chien, K. Takei, T. Takahashi, J. Nah, A. M. Niknejad, and A. Javey, Extremely bendable, high-performance integrated circuits using semiconducting carbon nanotube networks for digital, analog, and radio-frequency applications, *Nano Lett.* **12**, 1527 (2012). 6

[42] S. Park, M. Vosguerichian, and Z. Bao, A review of fabrication and applications of carbon nanotube film-based flexible electronics, *Nanoscale* **5**, 1727 (2013). 6

[43] P. H. Lau, K. Takei, C. Wang, Y. Ju, J. Kim, Z. Yu, T. Takahashi, G. Cho,

and A. Javey, Fully printed, high performance carbon nanotube thin-film transistors on flexible substrates, *Nano Lett.* **13**, 3864 (2013). 6

[44] Y. Che, H. Chen, H. Gui, J. Liu, B. Liu, and C. Zhou, Review of carbon nanotube nanoelectronics and macroelectronics, *Semicond. Sci. Technol.* **29**, 073001 (2014). 6

[45] N. Liu, K. N. Yun, H.-Y. Yu, J. H. Shim, and C. J. Lee, High-performance carbon nanotube thin-film transistors on flexible paper substrates, *Appl. Phys. Lett.* **106**, 103106 (2015). 6

[46] J. Zaumseil, Single-walled carbon nanotube networks for flexible and printed electronics, *Semicond. Sci. Technol.* **30**, 074001 (2015). 6

[47] S. Kumar, N. Pimparkar, J. Y. Murthy, and M. A. Alam, Theory of transfer characteristics of nanotube network transistors, *Appl. Phys. Lett.* **88**, 123505 (2006). 6, 57, 58, 78

[48] C. Kocabas, N. Pimparkar, O. Yesilyurt, S. J. Kang, M. A. Alam, and J. A. Rogers, Experimental and theoretical studies of transport through large scale, partially aligned arrays of single-walled carbon nanotubes in thin film type transistors, *Nano Lett.* **7**, 1195 (2007). 6, 57

[49] N. Rouhi, D. Jain, and P. J. Burke, High-performance semiconducting nanotube inks: Progress and prospects, *ACS Nano* **5**, 8471 (2011). 6, 57

[50] J. Li, Z.-B. Zhang, and S.-L. Zhang, Percolation in random networks of heterogeneous nanotubes, *Appl. Phys. Lett.* **91**, 253127 (2007). 6, 7, 31, 57, 60

[51] V. K. Sangwan, A. Behnam, V. W. Ballarotto, M. S. Fuhrer, A. Ural, and E. D. Wiliams, Optimizing transistor performance of percolating carbon nanotube networks, *Appl. Phys. Lett.* **97**, 043111 (2010). 6, 7, 11, 57, 72, 79

[52] P. G. Collins, M. S. Arnold, and P. Avouris, Engineering carbon nanotubes and nanotube circuits using electrical breakdown, *Science* **292**, 706 (2001). 7

[53] M. S. Arnold, A. A. Green, J. F. Hulvat, S. I. Stupp, and M. C. Hersam, Sorting carbon nanotubes by electronic structure using density differentiation, *Nat. Nanotechnol.* **1**, 60 (2006). 7

[54] G. Zhang, P. Qi, X. Wang, Y. Lu, X. Li, R. Tu, S. Bangsaruntip, D. Mann, L. Zhang, and H. Dai, Selective etching of metallic carbon nanotubes by gas-phase reaction, *Science* **314**, 974 (2006). 7

[55] S. Kumar, B. A. Cola, R. Jackson, and S. Graham, A review of carbon nanotube ensembles as flexible electronics and advanced packaging materials, *J. Elect. Packaging* **133**, 020906 (2011). 7

[56] L. Hu, D. S. Hecht, and G. Grüner, Carbon nanotube thin films: Fabrication, properties, and applications, *Chem. Rev.* **110**, 5790 (2010). 7, 58, 67

[57] D. S. Hecht, L. Hu, and G. Irvin, Emerging transparent electrodes based on thin films of carbon nanotubes, graphene, and metallic nanostructures, *Adv. Mater.* **23**, 1482 (2011). 7

[58] E. S. Snow, J. P. Novak, P. M. Campbell, and D. Park, Random networks of carbon nanotubes as an electronic material, *Appl. Phys. Lett.* **82**, 2145 (2003). 7, 60, 77, 78

[59] S. Seppälä, E. Häkkinen, M. J. Alava, V. Ermolov, and E. T. Seppälä, Electrical transport properties of percolating random networks of carbon nanotube bundles, *Europhys. Lett.* **91**, 47002 (2010). 7, 60

[60] J. Faist, F. Capasso, D. L. Sivco, C. Sitori, A. L. Hutchinson, and A. Y. Cho, Quantum cascade laser, *Science* **264**, 553 (1994). 8, 83

[61] C. Gmachl, F. Capasso, D. L. Sivco, and A. Y. Cho, Recent progress in quantum cascade lasers and applications, *Rep. Prog. Phys.* **64**, 1533 (2001). 8, 83

[62] B. S. Williams, Terahertz quantum-cascade lasers, *Nat. Photonics* **1**, 517 (2007). 8

[63] C. Becker, C. Sirtori, O. Drachenko, V. Rylkov, D. Smirnov, and J. Leotin, GaAs quantum box cascade lasers, *Appl. Phys. Lett.* **81**, 2941 (2002). 8, 83

[64] D. Smirnov, O. Drachenko, J. Leotin, H. Page, C. Becker, C. Sirtori, V. Apalkov, and T. Chakraborty, Intersubband magnetophonon resonances in quantum cascade structures, *Phys. Rev. B* **66**, 125317 (2002). 8, 9, 83, 84, 86, 93, 98

[65] D. Smirnov, C. Becker, O. Drachenko, V. V. Rylkov, H. Page, J. Leotin, and C. Sirtori, Control of electron–optical–phonon scattering rates in quantum box cascade lasers, *Phys. Rev. B* **66**, 121305 (2002). 8, 9, 83, 86

[66] A. Leuliet, A. Vasanelli, A. Wade, G. Fedorov, D. Smirnov, G. Bastard, and C. Sirtori, Electron scattering spectroscopy by a high magnetic field in quantum cascade lasers, *Phys. Rev. B* **73**, 085311 (2006). 8, 9, 83, 84, 86, 87, 89, 93

[67] O. Drachenko, S. Winnerl, H. Schneider, M. Helm, J. Wosnitza, and J Leotin, Compact magnetospectrometer for pulsed magnets based on infrared quantum cascade lasers, *Rev. Sci. Instrum.* **82**, 033108 (2011). 8, 9

[68] A. Hugi, R. Maulini, and J. Faist, External cavity quantum cascade laser, *Semicond. Sci. Technol.* **25**, 083001 (2010). 8

[69] R. F. Curl, F. Capasso, C. Gmachl, A. A. Kosterev, B. McManus, R. Lewicki, M. Pusharsky, G. Wysocki, and F. K. Tittel, Quantum cascade lasers in chemical physics, *Chem. Phys. Lett.* **487**, 1 (2010). 8

[70] M. Tonouchi, Cutting-edge terahertz technology, *Nat. Photonics* **1**, 97 (2007). 8

[71] C. Jirauschek and T. Kubis, Modeling techniques for quantum cascade lasers, *Appl. Phys. Rev.* **1**, 011307 (2014). 8, 83

[72] J. Faist, *Quantum Cascade Lasers*, 1st ed., Oxford University Press, Oxford (2013). 8, 83

[73] A. Gajić, J. Radovanović, V. Milanović, D. Indjin, and Z. Ikonić, Genetic algorithm applied to the optimization of quantum cascade lasers with second harmonic generation, *J. Appl. Phys.* **115**, 053712 (2014). 8, 83

[74] A. Daničić, J. Radovanović, V. Milanović, D. Indjin, and Z Ikonić, Magnetic field effects on THz quantum cascade laser: A comparative analysis of three and four quantum well based active region design, *Physica E* **81**, 275 (2016). 8, 83

[75] C. Becker, A. Vasanelli, C. Sirtori, and G. Bastard, Electron–longitudinal optical phonon interaction between Landau levels in semiconductor heterostructures, *Phys. Rev. B* **69**, 115328 (2004). 8, 9, 83, 86, 87, 93

[76] A. Wade, G. Fedorov, D. Smirnov, S. Kumar, B. S. Williams, Q. Hu, and J. L. Reno, Magnetic-field-assisted terahertz quantum cascade laser operating up to 225 K, *Nat. Photonics* **3**, 41 (2009). 8

[77] G. Scalari, C. Walther, L. Sirigu, M. L. Sadowski, H. Beere, D. Ritchie, N. Hoyler, M. Giovannini, and J. Faist, Strong confinement in terahertz intersubband lasers by intense magnetic fields, *Phys. Rev. B* **76**, 115305 (2007). 8

[78] F. R. Jasnot, L.-A. de Vaulchier, Y. Guldner, G. Bastard, A. Vasanelli, C. Manquest, C. Sirtori, M. Beck, and J. Faist, Direct surface cyclotron resonance terahertz emission from a quantum cascade structure, *Appl. Phys. Lett.* **100**, 102103 (2012). 8

[79] G. Scalari, D. Turčinková, J. Lloyd-Hughes, M. I. Amanti, M. Fischer, M. Beck, and J. Faist, Magnetically assisted quantum cascade laser emitting from 740 GHz to 1.4 THz, *Appl. Phys. Lett.* **97**, 081110 (2010). 8

[80] J. Radovanović, V. Milanović, Z Ikonić, D. Indjin, and P. Harrison, Electron-phonon relaxation rates and optical gain in a quantum cascade laser in a magnetic field, *J. Appl. Phys.* **97**, 103109 (2005). 9, 84, 91, 92

[81] H. B. Teng, J. P. Sun, G. I. Haddad, M. A. Stroscio, S. Yu, and K. W. Kim, Phonon assisted intersubband transitions in step quantum well structures, *J. Appl. Phys.* **84**, 2155 (1998). 10, 84, 88

[82] A. Trionfi, D. H. Wang, J. D. Jacobs, L.-S.Tan, R. A. Vaia, and J. W. P. Hsu, Direct measurement of the percolation probability in carbon nanofiber-polyimide nanocomposites, *Phys. Rev. Lett.* **102**, 116601 (2009). 11

[83] X.-Z. Bo, N. G. Tassi, C. Y. Lee, M. S. Strano, C. Nuckolls, and G. B. Blanchet, Pentacene-carbon nanotubes: Semiconducting assemblies for thin-film transistor applications, *Appl. Phys. Lett.* **87**, 203510 (2005). 11

[84] J. Li, Z.-B. Zhang, M. Östling, and S.-L. Zhang, Improved electrical performance of carbon nanotube thin film transistors by utilizing composite networks, *Appl. Phys. Lett.* **92**, 133103 (2008). 11

[85] S. Kumar, J.Y. Murthy, and M. A. Alam, Percolating conduction in finite nanotube networks, *Phys. Rev. Lett.* **95**, 066802 (2005). 11

[86] J. Li and S.-L. Zhang, Understanding doping effects in biosensing using carbon nanotube network field-effect transistors, *Phys. Rev. B* **79**, 155434 (2009). 11

[87] D. Stauffer, Search for logarithmic factors near the two-dimensional percolation threshold, *Phys. Lett. A* **83**, 404 (1981). 11, 26

[88] J. L. Cardy, Critical percolation in finite geometries, *J. Phys. A: Math. Gen* **25**, L201 (1992). 11, 12, 19

[89] R. M. Ziff, Spanning probability in 2D percolation, *Phys. Rev. Lett.* **69**, 2670 (1992). 11, 26

[90] A. Aharony and J.-P. Hovi, Comment on "Spanning probability in 2D percolation", *Phys. Rev. Lett.* **72**, 1941 (1994). 11

[91] J.-P. Hovi and A. Aharony, Scaling and universality in the spanning probability for percolation, *Phys. Rev. E* **53**, 235 (1996). 11, 18

[92] M. E. J. Newman and R. M. Ziff, Efficient Monte Carlo algorithm and high-precision results for percolation, *Phys. Rev. Lett.* **85**, 4104 (2000). 11

[93] R. M. Ziff and M. E. J. Newman, Convergence of threshold estimates for two-dimensional percolation, *Phys. Rev. E* **66**, 016129 (2002). 11, 12, 29

[94] G. E. Pike and C. H. Seager, Percolation and conductivity: A computer study, *Phys. Rev. B* **10**, 1421 (1974). 11

[95] I. Balberg and N. Binenbaum, Computer study of the percolation threshold in a two-dimensional anisotropic system of conducting sticks, *Phys. Rev. B* **28**, 3799 (1983). 11

[96] I. Balberg, C. H. Anderson, S Alexander, and N. Wagner, Excluded volume and its relation to the onset of percolation, *Phys. Rev. B* **30**, 3933 (1984). 11

[97] J. Bernasconi, Real-space renormalization of bond-disordered conductance lattices, *Phys. Rev. B* **18**, 2185 (1978). 12, 30, 43

[98] M. E. J. Newman and R. M. Ziff, Fast Monte Carlo algorithm for site or bond percolation, *Phys. Rev. E* **64**, 016706 (2001). 12, 13, 15, 107

[99] I. Stanković, M. Kröger, and S. Hess, Recognition and analysis of local structure in polycrystalline configurations, *Comput. Phys. Commun.* **145**, 371 (2002). 12, 35, 58

[100] A. Balaž, O. Prnjat, D. Vudragović, V. Slavnić, I. Liabotis, E. Atanassov, B. Jakimovski, and M. Savić, Development of grid e-infrastructure in South-eastern Europe, *J. Grid. Comput.* **9**, 135 (2011). 12

[101] J. Li and S.-L. Zhang, Finite-size scaling in stick percolation, *Phys. Rev. E* **80**, 040104 (2009). 12, 13, 17

[102] C. Li and T.-W. Chou, Continuum percolation of nanocomposites with fillers of arbitrary shapes, *Appl. Phys. Lett.* **90**, 174108 (2007). 31

[103] A. Balaž, I. Vidanović, D. Stojiljković, D. Vudragović, A. Belić, and A. Bogojević, SPEEDUP code for calculation of transition amplitudes via the effective action approach, *Commun. Comput. Phys.* **11**, 739 (2012). 35, 58

[104] Y. Zhou, S. Sreekala, P. M. Ajayan, and S. K. Nayak, Resistance of copper nanowires and comparison with carbon nanotube bundles for interconnect applications using first principles calculations, *J. Phys.: Condens. Matter* **20**, 095209 (2008). 36, 41

[105] J.-Y. Park, S. Rosenblatt, Y. Yaish, V. Sazonova, H. Üstünel, S. Braig, T.A. Arias, P. W. Brouwer, and P. L. McEuen, Electron−phonon scattering in metallic single-walled carbon nanotubes, *Nano Lett.* **4**, 517 (2004). 36, 41, 60

[106] Eric W. Weisstein, *CRC Concise Encyclopedia of Mathematics*, 2nd ed., CRC Press, United States (2002). 39, 107, 108

[107] J. R. Shewchuk, An introduction to the conjugate gradient method without the agonizing pain, `https://www.cs.cmu.edu/~quake-papers/painless-conjugate-gradient.pdf` (1994). 40, 113, 114, 115

[108] J.-Y. Yu, S.-W. Chung, and J. R. Heath, Silicon nanowires: Preparation, device fabrication, and transport properties, *J. Phys. Chem. B* **104**, 11864 (2000). 41

[109] M. S. Fuhrer, J. Nygård, L. Shih, M. Forero, Y. G. Yoon, M. S. C. Mazzoni, H. J. Choi, J. Ihm, S. G. Louie, A. Zettl, and P. L. McEuen, Crossed nanotube junctions, *Science* **288**, 494 (2000). 41, 58, 60

[110] A. Buldum and J. P. Lu, Contact resistance between carbon nanotubes, *Phys. Rev. B* **63**, 161403 (2001). 41, 60

[111] A. T. Bellew, H. G. Manning, C. Gomes da Rocha, M. S. Ferreira, and J. J. Boland, Resistance of single Ag nanowire junctions and their role in the conductivity of nanowire networks, *ACS Nano* **9**, 11422 (2015). 41, 53

[112] A. D. Franklin and Z. Chen, Length scaling of carbon nanotube transistors, *Nat. Nanotechnol.* **5**, 858 (2010). 41, 60

[113] A. Bid, A. Bora, and A. K. Raychaudhuri, Temperature dependence of the resistance of metallic nanowires of diameter ≥ 15 nm: Applicability of Bloch-Grüneisen theorem, *Phys. Rev. B* **74**, 035426 (2006). 41

[114] C. Grimaldi and I. Balberg, Tunneling and nonuniversality in continuum percolation systems, *Phys. Rev. Lett.* **96**, 066602 (2006). 43

[115] J. Heitz, Y. Leroy, L. Hébrard, and C. Lallement, Theoretical characterization of the topology of connected carbon nanotubes in random networks, *Nanotechnology* **22**, 345703 (2011). 45

[116] D. B. Gingold and C. J. Lobb, Percolative conduction in three dimensions, *Phys. Rev. B* **42**, 8220 (1990). 48

[117] A. Behnam and A. Ural, Computational study of geometry-dependent resistivity scaling in single-walled carbon nanotube films, *Phys. Rev. B* **75**, 125432 (2007). 60

[118] A. Javey, J. Guo, M. Paulsson, Q. Wang, D. Mann, M. Lundstrom, and H. Dai, High-field quasiballistic transport in short carbon nanotubes, *Phys. Rev. Lett.* **92**, 106804 (2004). 60

[119] P. Avouris, Carbon nanotube electronics and optoelectronics, *MRS Bull.* **29**, 403 (2004). 60, 67

[120] M. S. Purewal, B. H. Hong, A. Ravi, B. Chandra, J. Hone, and P. Kim, Scaling of resistance and electron mean free path of single-walled carbon nanotubes, *Phys. Rev. Lett.* **98**, 186808 (2007). 60

[121] A. Bachtold, P. Hadley, T. Nakanishi, and C. Dekker, Logic circuits with carbon nanotube transistors, *Science* **294**, 1317 (2001). 60

[122] A. Javey, J. Guo, Q. Wang, M. Lundstrom, and H. Dai, Ballistic carbon nanotube field-effect transistors, *Nature* **424**, 654 (2003). 60

[123] B. K. Sarker, N. Kang, and S. I. Khondaker, High performance semiconducting enriched carbon nanotube thin film transistors using metallic carbon nanotubes as electrodes, *Nanoscale* **6**, 4896 (2014). 60

[124] C. Wang, J. Zhang, and C. Zhou, Macroelectronic integrated circuits using high-performance separated carbon nanotube thin-film transistors, *ACS Nano* **4**, 7123 (2010). 67

[125] Y. Kuwahara, F. Nihey, S. Ohmori, and T. Saito, Length dependent performance of single-wall carbon nanotube thin film transistors, *Carbon* **91**, 370 (2015). 69

[126] The on-conductance of a rectangular TFT channel is $G_{\mathrm{ON}} = \sigma_{\mathrm{ON}} W_{\mathrm{CH}}/L_{\mathrm{CH}} = \sigma_{\mathrm{ON}}/r$, and similarly the off-conductance is $G_{\mathrm{OFF}} = \sigma_{\mathrm{OFF}}/r$, where σ_{ON} and σ_{OFF} are the on- and off-state conductivities, respectively. As one can see, the on-conductance G_{ON} is inversely proportional to the aspect ratio r, while the on/off ratio $G_{\mathrm{ON}}/G_{\mathrm{OFF}} = \sigma_{\mathrm{ON}}/\sigma_{\mathrm{OFF}}$ is independent of r. 72, 73, 74, 77, 78

[127] T. Ando, A. B. Fowler, and F. Stern, Electronic properties of two-dimensional systems, *Rev. Mod. Phys.* **54**, 437 (1982). 84, 89

[128] T. Unuma, M. Yoshita, T. Noda, H. Sakaki, and H. Akiyama, Intersubband absorption linewidth in GaAs quantum wells due to scattering by interface roughness, phonons, alloy disorder, and impurities, *J. Appl. Phys.* **93**, 1586 (2003). 84, 89

[129] M. Califano, N. Q. Vinh, P. J. Phillips, Z. Ikonić, R. W. Kelsall, P. Harrison, C. R. Pidgeon, B. N. Murdin, D. J. Paul, P. Townsend, J. Zhang, I. M. Ross, and A. G. Cullis, Interwell relaxation times in p−Si/SiGe asymmetric quantum well structures: Role of interface roughness, *Phys. Rev. B* **75**, 045338 (2007). 84, 89

[130] A. Valavanis, Z. Ikonić, and R. W. Kelsall, Intersubband carrier scattering in n- and p-Si/SiGe quantum wells with diffuse interfaces, *Phys. Rev. B* **77**, 075312 (2008). 84, 89

[131] T. Unuma, T. Takahashi, T. Noda, M. Yoshita, H. Sakaki, M. Baba, and H. Akiyama, Effects of interface roughness and phonon scattering on intersubband absorption linewidth in a GaAs quantum well, *Appl. Phys. Lett.* **78**, 3448 (2001). 89

[132] C. Weisbuch, R. Dingle, A. C. Gossard, and W. Wiegmann, Optical characterization of interface disorder in GaAs – $Ga_{1-x}Al_xAs$ multi-quantum well structures, *Solid State Commun.* **38**, 709 (1981). 89

[133] U. Ekenberg, Nonparabolicity effects in a quantum well: Sublevel shift, parallel mass, and Landau levels, *Phys. Rev. B* **40**, 7714 (1989). 91, 92, 94

[134] S. Živanović, V. Milanović, and Z. Ikonić, Intraband absorption in semiconductor quantum wells in the presence of a perpendicular magnetic field, *Phys. Rev. B* **52**, 8305 (1995). 91

[135] P. Kruck, H. Page, C. Sirtori, S. Barbieri, M. Stellmacher, and J. Nagle, Improved temperature performance of $Al_{0.33}Ga_{0.67}As$/GaAs quantum-cascade lasers with emission wavelength at $\lambda \approx 11$ μm, *Appl. Phys. Lett.* **76**, 3340 (2000). 93

[136] J. Wang, J.-P. Leburton, Z. Moussa, F. H. Julien, and A. Saár, Simulation of optically pumped mid-infrared intersubband semiconductor laser structures, *J. Appl. Phys.* **80**, 1970 (1996). 94

[137] A. Daničić, J. Radovanović, V. Milanović, D. Indjin, and Z Ikonić, Optimization and magnetic-field tunability of quantum cascade laser for applications in trace gas detection and monitoring, *J. Phys. D: Appl. Phys.* **43**, 045101 (2010). 100

Publications list

[1] **M. Žeželj**, V. Milanović, J. Radovanović, and I. Stanković, Influence of interface roughness scattering on output characteristics of GaAs/AlGaAs quantum cascade laser in a magnetic field, *J. Phys. D: Appl. Phys.* **44**, 325105 (2011).

[2] **M. Žeželj**, I. Stanković, and A. Belić, Finite-size scaling in asymmetric systems of percolating sticks, *Phys. Rev. E* **85**, 021101 (2012).

[3] **M. Žeželj** and I. Stanković, From percolating to dense random stick networks: Conductivity model investigation, *Phys. Rev. B* **86**, 134202 (2012).

[4] J. Smiljanić, **M. Žeželj**, V. Milanović, J. Radovanović, and I. Stanković, MATLAB-based program for optimization of quantum cascade laser active region parameters and calculation of output characteristics in magnetic field, *Comput. Phys. Commun.* **185**, 998 (2014).

[5] I. Stanković, **M. Žeželj**, J. Smiljanić, A. Belić, Modelling of disaster spreading dynamics, in *High-Performance Computing Infrastructure for South East Europe's Research Communities, Springer Book Series on Modeling and Optimization in Science and Technologies* **2**, 31 (2014).

[6] **M. Žeželj** and I. Stanković, Random networks of carbon nanotubes optimized for transistor mass-production: Searching for ultimate performance, *Semicond. Sci. Technol.* **31**, 105015 (2016).

Biography

Milan Žeželj was born in 1985 in Zemun, Serbia. He has finished the Mathematical Grammar School in Belgrade in 2004. In the same year he was awarded a bronze medal at the 35th International Physics Olympiad. Afterwards, he started his undergraduate studies at the School of Electrical Engineering, University of Belgrade, which he has finished in 2008 as the best student of generation at the Department of Electronics. In 2009 he completed his master studies, also at the Department of Electronics. In autumn 2009 he started his PhD studies at the School of Electrical Engineering, University of Belgrade, module: Nanoelectronics and Photonics.

Milan Žeželj started his research at the Scientific Computing Laboratory, Center for the Study of Complex Systems of the Institute of Physics Belgrade at the beginning of 2010 under the supervision of Dr. Igor Stanković. His research interests include transport processes in materials of complex and disordered morphology. During his PhD studies Milan published 6 papers in leading international journals. He was actively involved in research projects funded by the Ministry of Education, Science, and Technological Development of the Republic of Serbia and he also took part in an international project financed by the SCOPES program of the Swiss National Science Foundation. He actively participated in several conferences and schools.

Изјава о ауторству

Име и презиме аутора: **Милан Жежељ**

Број индекса: **5043/2009**

Изјављујем

да је докторска дисертација под насловом

Моделовање и оптимизација транспортних процеса у савременим наноелектронским уређајима

- резултат сопственог истраживачког рада;
- да дисертација у целини ни у деловима није била предложена за стицање друге дипломе према студијским програмима других високошколских установа;
- да су резултати коректно наведени и
- да нисам кршио/ла ауторска права и користио/ла интелектуалну својину других лица.

Потпис аутора

У Београду, 01.11.2016.

Милан Жежељ

Изјава о истоветности штампане и електронске верзије докторског рада

Име и презиме аутора: **Милан Жежељ**

Број индекса: **5043/2009**

Студијски програм: **Наноелектроника и фотоника**

Наслов рада: **Моделовање и оптимизација транспортних процеса у савременим наноелектронским уређајима**

Ментор: **проф. др. Јелена Радовановић**

Изјављујем да је штампана верзија мог докторског рада истоветна електронској верзији коју сам предао/ла ради похрањена у **Дигиталном репозиторијуму Универзитета у Београду.**

Дозвољавам да се објаве моји лични подаци везани за добијање академског назива доктора наука, као што су име и презиме, година и место рођења и датум одбране рада.

Ови лични подаци могу се објавити на мрежним страницама дигиталне библиотеке, у електронском каталогу и у публикацијама Универзитета у Београду.

Потпис аутора

У Београду, 01.11.2016.

Милан Жежељ

Изјава о коришћењу

Овлашћујем Универзитетску библиотеку „Светозар Марковић“ да у Дигитални репозиторијум Универзитета у Београду унесе моју докторску дисертацију под насловом:

Моделовање и оптимизација транспортних процеса у савременим наноелектронским уређајима

која је моје ауторско дело.

Дисертацију са свим прилозима предао/ла сам у електронском формату погодном за трајно архивирање.

Моју докторску дисертацију похрањену у Дигиталном репозиторијуму Универзитета у Београду и доступну у отвореном приступу могу да користе сви који поштују одредбе садржане у одабраном типу лиценце Креативне заједнице (Creative Commons) за коју сам се одлучио/ла.

1. Ауторство (CC BY)
2. Ауторство – некомерцијално (CC BY-NC)
3. Ауторство – некомерцијално – без прерада (CC BY-NC-ND)
4. Ауторство – некомерцијално – делити под истим условима (CC BY-NC-SA)
5. Ауторство – без прерада (CC BY-ND)
6. Ауторство – делити под истим условима (CC BY-SA)

(Молимо да заокружите само једну од шест понуђених лиценци.
Кратак опис лиценци је саставни део ове изјаве).

Потпис аутора

У Београду, 01.11.2016.

Милан Жежељ

1. **Ауторство**. Дозвољавате умножавање, дистрибуцију и јавно саопштавање дела, и прераде, ако се наведе име аутора на начин одређен од стране аутора или даваоца лиценце, чак и у комерцијалне сврхе. Ово је најслободнија од свих лиценци.

2. **Ауторство – некомерцијално**. Дозвољавате умножавање, дистрибуцију и јавно саопштавање дела, и прераде, ако се наведе име аутора на начин одређен од стране аутора или даваоца лиценце. Ова лиценца не дозвољава комерцијалну употребу дела.

3. **Ауторство – некомерцијално – без прерада**. Дозвољавате умножавање, дистрибуцију и јавно саопштавање дела, без промена, преобликовања или употребе дела у свом делу, ако се наведе име аутора на начин одређен од стране аутора или даваоца лиценце. Ова лиценца не дозвољава комерцијалну употребу дела. У односу на све остале лиценце, овом лиценцом се ограничава највећи обим права коришћења дела.

4. **Ауторство – некомерцијално – делити под истим условима**. Дозвољавате умножавање, дистрибуцију и јавно саопштавање дела, и прераде, ако се наведе име аутора на начин одређен од стране аутора или даваоца лиценце и ако се прерада дистрибуира под истом или сличном лиценцом. Ова лиценца не дозвољава комерцијалну употребу дела и прерада.

5. **Ауторство – без прерада**. Дозвољавате умножавање, дистрибуцију и јавно саопштавање дела, без промена, преобликовања или употребе дела у свом делу, ако се наведе име аутора на начин одређен од стране аутора или даваоца лиценце. Ова лиценца дозвољава комерцијалну употребу дела.

6. **Ауторство – делити под истим условима**. Дозвољавате умножавање, дистрибуцију и јавно саопштавање дела, и прераде, ако се наведе име аутора на начин одређен од стране аутора или даваоца лиценце и ако се прерада дистрибуира под истом или сличном лиценцом. Ова лиценца дозвољава комерцијалну употребу дела и прерада. Слична је софтверским лиценцама, односно лиценцама отвореног кода.